

## THE ULTRAVIOLET DETECTION OF DIFFUSE GAS IN GALAXY GROUPS

JOHN T. STOCKE,<sup>1</sup> BRIAN A. KEENEY,<sup>1</sup> CHARLES W. DANFORTH,<sup>1</sup> BENJAMIN D. OPPENHEIMER,<sup>1</sup> CAMERON T. PRATT,<sup>1</sup>  
ANDREAS A. BERLIND,<sup>2</sup> CHRIS IMPEY,<sup>3</sup> AND BUELL JANNUZI<sup>3</sup>

<sup>1</sup>*Center for Astrophysics and Space Astronomy, Department of Astrophysical and Planetary Sciences, University of Colorado, 389 UCB, Boulder, CO 80309, USA*

<sup>2</sup>*Department of Physics and Astronomy, Vanderbilt University, PMB 401807, 2401 Vanderbilt Place, Nashville, TN 37240-1807, USA*

<sup>3</sup>*Steward Observatory, University of Arizona, 933 N Cherry Avenue, Tucson, AZ 85721, USA*

### ABSTRACT

A small survey of the UV-absorbing gas in 12 low- $z$  galaxy groups has been conducted using the Cosmic Origins Spectrograph (COS) on-board the *Hubble Space Telescope* (HST). Targets were selected from a large, homogeneously-selected sample of groups found in the Sloan Digital Sky Survey (SDSS). A critical selection criterion excluded sight lines that pass close ( $< 1.5$  virial radii) to a group galaxy, to ensure absorber association with the group as a whole. To characterize these  $10^{13.5}$  to  $10^{14.5} M_{\odot}$  groups, the most massive of which are highly-virialized with numerous early-type galaxies (ETGs). This sample also includes two spiral-rich groups, not yet fully-virialized. At group-centric impact parameters of 0.3-2 Mpc, these S/N = 15-30 spectra detected H I absorption in 7 of 12 groups; high (O VI) and low (Si III) ion metal lines are present in 2/3 of the absorption components. None of the three most highly-virialized, ETG-dominated groups are detected in absorption. Covering fractions  $\gtrsim 50\%$  are seen at all impact parameters probed, but do not require large filling factors despite an enormous extent. Unlike halo clouds in individual galaxies, group absorbers have radial velocities which are too low to escape the group potential well without doubt. This suggests that these groups are “closed boxes” for galactic evolution in the current epoch. Evidence is presented that the cool and warm group absorbers are not a pervasive intra-group medium (IGrM), requiring a hotter ( $T \sim 10^6$  to  $10^7$  K) IGrM to be present to close the baryon accounting.

*Keywords:* quasars: absorption lines — galaxies: halos — intergalactic medium — galaxies: groups — galaxies: evolution

## 1. INTRODUCTION

In the past decade, the *Hubble Space Telescope* (*HST*) and its UV spectrographs have brought a tremendous increase in our knowledge of the relationship between galaxies and the diffuse circum- and inter-galactic media (CGM & IGM) out of which galaxies are still forming. But while QSO absorption-line probes show that diffuse gas in the IGM accounts for the vast majority of baryons at all epochs (Rauch 1998; Shull, Smith, & Danforth 2012), the “baryon census” is still not complete at low- $z$ , either for individual spiral galaxies (Klypin et al. 2001; Stocke et al. 2013, although see Prochaska et al. 2017 for a different view) or on cosmological scales (Shull et al. 2012). With the IGM becoming more complex with time (e.g., Davé et al. 1999; Cen & Ostriker 1999), the effects of galaxy feedback and non-equilibrium cooling complicate both an observational search and a theoretical prediction for diffuse gas associated with individual galaxies (Tumlinson et al. 2011; Oppenheimer et al. 2012; Stocke et al. 2013; Werk et al. 2013; Prochaska et al. 2017), galaxy groups and clusters (Yoon et al. 2012; Yoon & Putman 2013, 2017), and large-scale galaxy structures (Wakker et al. 2015; Tejos, Rodríguez-Puebla, & Primack 2018).

Of particular interest in this regard are highly-ionized metal (O VI & Ne VIII) lines and thermally-broadened H I absorptions, which show that there is a sizable fraction of warm gas (following the naming convention in Savage et al. 2014, since sometimes gas in this temperature range is called the warm-hot IGM, or WHIM) locally at  $T > 10^5$  K. The WHIM is suspected to harbor the bulk of the “missing baryons” at low- $z$ , and may also be an important gas reservoir in the recycling processes of galactic winds and in-fall that continue to fuel on-going star formation in spiral galaxies (e.g., Binney & Tremaine 1987). Surveys for metal ion absorbers (e.g., Steidel et al. 2010; Danforth & Shull 2008; Tumlinson et al. 2011; Burchett et al. 2016) show that gas enriched by star formation has been transported quite far from galaxies (Chen et al. 2001; Adelberger et al. 2005; Stocke et al. 2006, 2013; Prochaska et al. 2011; Johnson, Chen, & Mulchaey 2015; Pratt et al. 2018), up to  $\sim 600$  kpc or more in the current epoch, much larger than the inferred virial radius of even the most massive galaxies, but somewhat smaller than the size of most galaxy groups.

The science program of the Cosmic Origins Spectrograph (COS) Guaranteed Time Observers (GTOs; Stocke et al. 2013; Keeney et al. 2017) and the various *HST* guest observer (GO) Projects, including COS-Halos, COS-Dwarfs and COS-GASS (Tumlinson et al. 2011; Werk et al. 2013; Bordoloi et al. 2014; Borthakur et al. 2013), and the Andromeda Galaxy AMIGA project (Lehner, Howk, & Wakker 2015), among others, have gone a long way towards defining the relationship between individual galaxies, their massive photo-ionized CGMs ( $> 10^{10} M_{\odot}$  at  $T \sim 10^4$  K for

$L \geq L^*$ , late-type galaxies) and the shocked interfaces with hotter gas seen as O VI absorptions (Savage et al. 2010, 2012; Tumlinson et al. 2011, 2013; Prochaska et al. 2011; Thom et al. 2012; Borthakur et al. 2013; Stocke et al. 2013, 2014; Werk et al. 2013, 2014; Bordoloi et al. 2014; Lehner et al. 2014). However dramatic the CGM detections have been, these studies still leave  $\lesssim 50\%$  of spiral baryons unaccounted for in the current epoch (but see Prochaska et al. 2017 for an accounting in which the CGM baryon content is dominated by warm gas). If there are as-yet undetected baryons in the CGM, this uncertainty leaves important questions unanswered, including what are the physical conditions of these baryons and are these baryons still bound to the galaxies or blown out into the IGM?

Savage et al. (2014, Paper 1 hereafter) used *HST*/COS spectra with S/N = 20-50 to detect and analyze 54 O VI absorbers at low- $z$ , including at least 14 systems which are demonstrably collisionally ionized gas at warm temperatures ( $T > 10^5$  K) too hot to be cool, photo-ionized gas. The remaining O VI systems are either cooler than this limit, suggesting photo-ionized gas, or have velocity misalignments that preclude conclusive temperature analysis (see Paper 1 for detailed methodology). The broad, shallow absorptions seen in many of these O VI plus Ly $\alpha$  systems are not obviously associated with individual galaxies, since many of these absorbers are found well outside the virial radius of the nearest galaxy (Keeney et al. 2017; Pratt et al. 2018).

In Stocke et al. (2014, Paper 2 hereafter), the galaxy environments of nearby ( $z \leq 0.15$ ) photo-ionized and collisionally ionized O VI absorbers from Paper 1 were investigated. Based on deep and wide galaxy surveys around these sight lines, groups of galaxies were found in all cases. Using a subset of these groups for which at least eight members were identified, weak correlations ( $\sim 95\%$  confidence level) were found between the gas temperatures as inferred from the O VI and H I  $b$ -values and the velocity dispersions and total luminosities of the groups. While an association between some of these absorbers and the nearest group galaxy to the sight line is plausible in several cases, Paper 2 puts forward the hypothesis that most of these warm absorbers are associated with an entire galaxy group.

If this is the case, a simple argument suggests that these warm absorbers are very large, and massive enough to account for the remainder of the missing baryons in late-type galaxies; viz. using the warm absorber line density of  $dN/dz \geq 4$  per unit redshift (Paper 2) in conjunction with the local space density of galaxy groups (Pisani, Ramella, & Geller 2003; Berlind et al. 2006) requires that these absorbers have radii  $\geq 1$  Mpc at high covering factor (larger still, if “patchy”), and therefore quite massive ( $\lesssim 10^{12} M_{\odot}$ ; Paper 2). This is comparable to the mass of the X-ray emitting intra-cluster medium (ICM) in elliptical-dominated groups and

poor clusters, where it is the dominant baryon reservoir at halo masses of  $\geq 10^{14.5} M_{\odot}$  (Mulchaey 2000).

However, little is known about the intra-group medium (IGrM) in the lower-mass halos ( $10^{12}$  to  $10^{14} M_{\odot}$ ) typical of small groups of galaxies, the most numerous ensembles of galaxies in the Universe. If a massive IGrM is present at the expected temperatures ( $\log [T/\text{K}] = 6.2\text{--}6.5$ ; Mulchaey et al. 1996), it would be difficult to detect — too cool to emit significantly at keV energies, and too hot to create narrow, high column density H I Ly $\alpha$  and metal absorption lines. But at the very least, a rudimentary (i.e., patchy and multi-temperature) IGrM is expected because disk galaxies merge to form the central elliptical in elliptical-dominated groups, which do exhibit massive, X-ray emitting IGrMs.

If an IGrM at warm temperatures or slightly higher is volume-filling, its mass is comparable to the amount needed to bring groups up to the cosmic mean baryon-to-dark matter ratio (e.g. Klypin et al. 1999; McGaugh et al. 2000). This would make groups of galaxies, like the more massive clusters, “closed boxes” for galactic evolution. Recent observational work by Pratt et al. (2018) confirms earlier studies which showed that high metallicity gas ( $Z \geq 0.1 Z_{\odot}$  as traced by O VI absorption) does not extend farther than  $\approx 600$  kpc from its source inside star-forming galaxies; this maximum distance that metal absorption (specifically O VI) extends from galaxies is insufficient for the gas to escape from the group. On the other hand, current numerical simulations differ by factors of 3-5 on the percentage of baryons retained by groups in this critical mass range ( $\log [M/M_{\odot}] = 13\text{--}14.5$ ); e.g., COSMO-Owls (Le Brun et al. 2014), EAGLE (Schaye et al. 2015) and ILLUSTRIS (Nelson et al. 2018) find divergent values in this halo mass range due to differing feedback prescriptions.

Reconciling the observational results with the numerical simulations is important. If all the baryons expelled from individual galaxies are retained inside galaxy groups, this would have important consequences for galactic evolution; e.g., some of the observed width in the mass-metallicity relationship (Tremonti et al. 2004) could be due to differing chemical histories between groups of galaxies. Additionally, the continuing high star formation rate in spirals and the so-called “G-dwarf problem” (Binney & Tremaine 1987; Pagel 2009) must be reconciled within individual galaxy groups. Given these important consequences, the hypotheses put forward above, which are based on the *HST/COS* results of Papers 1 & 2, need to be tested. This is one of the purposes of the current paper.

This paper is organized as follows: Section 2 describes the experimental design for this investigation and the selection of the sample of low- $z$  galaxy groups with QSO probes. Section 3 presents the *HST/COS* UV spectra and the basic analysis of the absorption systems detected at the redshifts of the

foreground groups, including an analysis of the few possible broad Ly $\alpha$  absorbers (BLAs) in these groups. Section 4 presents the analysis of the galaxy redshift surveys conducted around each sight line based on the data found in Keeney et al. (2018), and describes the group-finding algorithm and derived group parameters (e.g., membership, sky position, redshift and velocity dispersion) for each group. Section 5 discusses the results of this survey of gas in galaxy groups, including whether the absorption is associated with an individual group galaxy or the entire group. Discussions of gas covering fractions, absorber kinematics and absorber/group correlations are also included in this Section. Section 6 summarizes the basic observational properties of this work and describes the important conclusions derived from this survey. Detailed descriptions of the *HST/COS* spectroscopy are presented in Appendix A, including Table 10, which provides measurements for each absorption line detected that is associated with these groups. Appendix B presents detailed notes on each galaxy group. Throughout this paper we assume a WMAP9 cosmology (i.e.,  $H_0 = 69.7 \text{ km s}^{-1} \text{ Mpc}^{-1}$ ,  $\Omega_{\Lambda} = 0.718$  and  $\Omega_m = 0.282$ ; Hinshaw et al. 2013).

## 2. EXPERIMENTAL DESIGN AND SAMPLE SELECTION

This project investigates whether galaxy groups possess a cool and/or warm component to the IGrM by performing the reverse experiment to that of Papers 1 and 2. In those papers, the *HST/COS* spectra were used to find and identify WHIM absorbers, then the foreground galaxy distribution at the absorber distances were examined; groups of galaxies were found to be present in virtually all cases. However, groups of galaxies are a very common phenomenon in the low- $z$  Universe ( $3 \times 10^{-3} \text{ Mpc}^{-3}$  at  $M_{\text{grp}} \geq 10^{13} M_{\odot}$ ; Berlind et al. 2006, Paper 3 hereafter). Moreover, these warm gas-selected groups in Paper 2 have rather heterogeneous properties, ranging from systems with total luminosities of  $\sim 50 L^*$  and  $\sigma_{\text{grp}} \approx 300\text{--}500 \text{ km s}^{-1}$  to much smaller groups similar to the M51/M101 group. This diversity casts some doubt on the associations proposed in Paper 2; in some cases, the absorption could be due to individual galaxy halos, not to gas associated with the entire group. Since galaxies and groups of galaxies are not independent phenomena, it is difficult to ascribe association of gas to one and not the other using the method of Papers 1 and 2.

Here we reverse this experiment. We start by pre-selecting a homogeneous set of low- $z$  galaxy groups defined by a uniform, objective selection method. By using a homogeneously selected sample of groups, we avoid the problem of assigning association to a very heterogeneous population for which a potential chance coincidence between absorbers and groups is possible. A large catalog of galaxy groups ( $> 7500$ ) chosen systematically from the Sloan Digital Sky Survey (SDSS) us-

**Table 1.** *HST*/COS Observations

Group ID	AGN Target Name	$z_{\text{AGN}}$	Obs. Date	$t_{\text{exp}}$ (ksec)	$F_{\text{FUV}}$ ( $10^{-15}$ )	S/N	Notes
(1)	(2)	(3)	(4)	(5)	(6)	(7)	(8)
12833	RBS 711	0.255	9/29/16	5	12	29	14277-07
16803	SDSS J1540-0205	0.321	7/3/16	25.3	$< 1^{\text{d}}$	11	14277-05,-06
19670	SBS 0956+510	0.143	6/23/16	8.0	8	21	14277-09
25124	B 1612+266	0.395	Jul/Aug '16 <sup>c</sup>	25.4	2	20	14277-03,-04
32123	SDSS J1333+4518	0.320	4/26/17	11	2	16	14277-16
36001	SDSS J1028+2119	0.374	4/2/16	15.9	4	26	14277-01,-02
44564	CSO 1022 <sup>a</sup>	0.285	6/30/14	4.8	5	16	13444 <sup>e</sup> (Wakker)
44565	CSO 1022 <sup>a</sup>	0.285	6/30/14	4.8	5	16	13444 <sup>e</sup> (Wakker)
44726	CSO 1080	0.526	7/7/16	10.1	5	19	14277-13,-15
44739	FBQS J1519+2838 <sup>b</sup>	0.270	8/10/16	15.8	3	22	14277-11,-12
44858	FBQS J1519+2838 <sup>b</sup>	0.270	8/10/16	15.8	3	22	14277-11,-12
50433	FBQS J1030+3102	0.178	3/26/16	4.9	12	23	14277-10

<sup>a</sup>Two groups are probed by the CSO 1022 sight line

<sup>b</sup>Two groups are probed by the FBQS J1519+2838 sight line

<sup>c</sup>Two coadded visits 22 Jul and 6 Aug 2016

<sup>d</sup>Partial LLS at source redshift mostly eliminates O VI sensitivity.

<sup>e</sup>Archival dataset

ing the algorithm of Paper 3 was used to identify appropriate groups for study.

Restricting the groups searched to redshifts of  $z = 0.1-0.2$ : (1) allows good SDSS galaxy group membership selection and characterization (e.g., estimated total luminosities, sizes and velocity dispersions); (2) facilitates excellent follow-up observations using multi-object galaxy spectroscopy (MOS already in-hand; Keeney et al. 2018) and (3) allows both the O VI doublet and Ly $\alpha$  (as well as Ly $\beta$ , Si III, and other lines of potential interest) to be observed with COS in the highest throughput G130M mode in a minimum number of *HST* orbits. Much of this wavelength range is blueward of the Ly $\alpha$  rest wavelength, making an O VI identification much easier and more secure, even if only one line of the doublet is detected (Stocke et al. 2017).

Next, we cross-correlated the redshift-restricted group catalog with a list of bright ( $V \lesssim 17.5$ ) background QSO targets, which allows high-S/N spectra to be obtained in just a few orbits. We required that the AGN sight lines intersect these groups at a range of impact parameters ( $\rho$ ):  $0.25 \leq \rho \leq 1.5$  group virial radii (symbolized  $R_{\text{grp}}$  herein to distinguish this scaling parameter from an individual galaxy's virial radius,  $R_{\text{vir}}$ ). Some of these impact parameters are modified by our

more detailed examination of group membership and properties described in Section 4. While sight lines at larger impact parameters were available, association between absorbers and individual groups become less secure at larger radii. Importantly, we rejected sight lines which passed within  $1.5 R_{\text{vir}}$  of a group galaxy to make sure we were observing group gas, not gas associated with individual galaxies (see e.g., Prochaska et al. 2011; Stocke et al. 2013; Keeney et al. 2017).

The resulting QSO target list along with basic observational details is shown in Table 1. Despite having thousands of groups in the catalog from which to choose, the restrictions mentioned above leave only about two dozen which have bright QSOs projected nearby. Only six of these targets had been previously observed by COS and all but one of these six have S/N too low for detecting broad, shallow WHIM absorbers.

However, FBQS 1010+3003 has medium-quality archival COS data (S/N = 15 (20) at O VI (Ly $\alpha$ ); Stocke et al. 2017) with a broad ( $b \approx 100 \text{ km s}^{-1}$ ), shallow,  $4\sigma$  detection of O VI 1032 Å at approximately the redshift of a group in our catalog. While Ly $\alpha$  shows several narrower, photo-ionized CGM components most likely associated with individual group

galaxies, there is no Ly $\alpha$  absorber that can be associated with the O VI. This requires  $T > 10^6$  K as in [Savage et al. \(2010\)](#). There is no other plausible identification for the O VI line since it is found blueward of the Ly $\alpha$  rest wavelength.

Based on an analysis of five SDSS galaxies and 15 from WIYN/HYDRA ([Keeney et al. 2018](#)) located at  $\rho < 2$  Mpc and  $|\Delta v_{\text{abs}}| < 2000$  km s $^{-1}$  from the O VI absorber, this group has  $\sigma_{\text{grp}} \approx 200$  km s $^{-1}$  ([Stocke et al. 2017](#)), similar to what was found by Paper 2 for some absorber-selected galaxy groups. In this case, the group centroid on the sky and its mean recession velocity made a group association with the O VI absorber unlikely. Instead, [Stocke et al. \(2017\)](#) concluded that the warm gas detection most likely was associated with the single, nearest galaxy to the absorber. This test case is a cautionary tale for this project, highlighting both the importance of choosing targets well away from bright group galaxies, and also the difficulty in both characterizing groups of galaxies and determining if the observed UV absorption system is related primarily to an individual galaxy or to the entire group.

With the absence of sufficient high-S/N UV spectra in the *HST* archive to conduct this experiment, we used the SDSS group catalog to identify ten new, bright targets which span a range of impact parameters through low- $z$  galaxy groups. Of the ten targets selected, one (CSO 1022) was observed by Program 13444 (PI: Wakker) during the previous cycle. These ten QSO sight lines plus the FBQS 1010+3003 sight line probe a well-defined sample of 13 pre-selected galaxy groups at a variety of impact parameters (two sight lines probe two distinct groups at two different redshifts; see [Table 1](#)). In conjunction with the ‘‘serendipitous’’ sample of group WHIM detections from Papers 1 and 2, these detections either will affirm or deny the proposed model for these warm absorbers as an IGrM.

[Table 2](#) lists the properties of the groups defined by the SDSS analysis of Paper 3. The group identifier is listed in column 1, followed by the number of group members in column 2. The group centroid on the sky is listed in columns 3 and 4, its redshift in column 5, and its estimated mass ( $M_0$ ) and velocity dispersion ( $\sigma_0$ ) in columns 6 & 7. Finally, the coordinates of the QSO sight line that probes the group ([Table 1](#)) are listed in columns 8 & 9. Note that despite the modest numbers of group members ( $N_0 = 3$ -10), these groups have  $M_0 > 10^{14} M_{\odot}$  in most cases.

### 3. *HST*/COS SPECTROSCOPY

This section details the UV absorption systems associated with the 13 SDSS galaxy groups. Systems of absorption are considered within  $\pm 2.5 \sigma_0$  of the mean redshift of the group (see [Table 2](#)). This broad window is necessary both because individual components of the system may be related either to an individual galaxy or the entire group and also because

the original group mean position and recession velocity were based on just the few brightest SDSS group galaxies. We revise the original estimate of group parameters using SDSS combined with the MOS presented in [Section 4](#), and will revisit the velocity, velocity dispersion and sky offsets of each group as it pertains to the detected absorbers.

For each of the nine sight lines in our *HST* observing program (#14277: Stocke, PI) a single COS G130M spectrum was obtained over several orbits in *HST* Cycle 23 (see [Table 1](#) for details). The G130M spectrum of CSO 1022 was taken by program #13444 in the previous *HST* cycle and obtained S/N  $\approx 16$  at 1200 Å. The G130M spectrum of FBQS 1010+3003 exceeds this criteria at Ly $\alpha$  and is close to this S/N ratio at O VI (see above).

All other sight lines have a S/N ratio at this level or greater, allowing the  $4\sigma$  detection of an unresolved O VI 1032 Å line with an equivalent width  $W_{\lambda} \gtrsim 40$  mÅ, corresponding to an O VI column density of  $N_{\text{OVI}} \gtrsim 10^{13.5}$  cm $^{-2}$  in the co-added spectra. However, one spectrum obtained by this program, SDSS J1540–0205, has a higher redshift Lyman limit system (LLS) that obscures the wavelength where the O VI absorption would appear in group 16803 ( $z_0 = 0.14839$ ). Because Si III absorption is not detected in a high-S/N portion of this same spectrum at the group redshift, we conservatively identify this sight line as an H I-only detection, even though the potential O VI wavelength does not meet the above criteria.

Spectra were processed using the techniques employed in [Danforth et al. \(2016\)](#), including automated line-identification procedures based on the Faint Object Spectrograph procedure developed by [Schneider et al. \(1993\)](#), with statistical significance for each line determined by the method developed specifically for the COS data by [Keeney et al. \(2012\)](#). In our first analysis of each spectrum, we searched for systems of absorbers (see detailed discussion of systems versus components in [Danforth et al. 2016](#)) and then refit each spectrum to determine the component(s) associated with the O VI absorption, if present.

We present a top-level summary of the absorption-line findings in [Table 3](#). Four sight lines (five groups) show strong H I absorption and significant (though not necessarily strong) O VI absorption in at least one component. Four sight lines show H I absorption, but no O VI; this includes the SDSSJ 15403–0205 sight line, where a weak Ly $\alpha$  feature is seen  $\sim 900$  km s $^{-1}$  from the SDSS center of group 16803, but the corresponding O VI is obscured by an intervening LLS. Finally, two sight lines (three groups) show no significant absorption of any kind within the established velocity range of the group (see [Section 5.1](#)).

[Figure 1](#) shows all absorption within  $\pm 2.5 \sigma_0$  of the SDSS group redshifts in [Table 2](#), indicated by the green circles, whose error bars indicate the SDSS redshift uncertainty. The blue diamonds with error bars show the revised group red-

**Table 2.** Group Properties from SDSS Analysis

Group	$N_0$	RA <sub>0</sub>	Dec <sub>0</sub>	$z_0$	log $M_0$	$\sigma_0$	RA <sub>*</sub>	Dec <sub>*</sub>
(1)	(2)	(3)	(4)	(5)	(6)	(7)	(8)	(9)
12833	8	129.423 ± 0.040	44.295 ± 0.029	0.14693 ± 0.00077	14.42 ± 0.26	534	129.245433	44.433969
16803	10	234.981 ± 0.015	-2.040 ± 0.040	0.14839 ± 0.00046	14.54 ± 0.25	586	235.081530	-2.084831
19670	8	150.196 ± 0.044	50.794 ± 0.028	0.13443 ± 0.00052	14.38 ± 0.26	518	149.881960	50.746969
25124	7	243.541 ± 0.018	26.625 ± 0.036	0.18613 ± 0.00038	14.64 ± 0.24	632	243.544250	26.547278
32123	6	203.074 ± 0.066	45.413 ± 0.024	0.15971 ± 0.00044	14.15 ± 0.29	434	203.253458	45.302500
36001	3	157.110 ± 0.045	21.338 ± 0.028	0.18788 ± 0.00023	14.17 ± 0.28	441	157.060646	21.331967
44564	4	208.120 ± 0.040	36.261 ± 0.022	0.14506 ± 0.00050	14.04 ± 0.30	399	208.358845	36.347070
44565	5	208.151 ± 0.016	36.280 ± 0.013	0.14925 ± 0.00054	14.21 ± 0.28	455	208.358845	36.347070
44726	4	226.175 ± 0.034	29.791 ± 0.035	0.15208 ± 0.00092	13.76 ± 0.35	322	226.365002	29.788439
44739	7	229.811 ± 0.033	28.413 ± 0.051	0.11839 ± 0.00023	14.22 ± 0.28	458	229.900610	28.641011
44858	9	230.091 ± 0.027	28.850 ± 0.013	0.12740 ± 0.00055	14.44 ± 0.26	542	229.900610	28.641011
50433	4	157.742 ± 0.026	30.864 ± 0.009	0.13599 ± 0.00033	14.12 ± 0.29	424	157.746220	31.048811

NOTE—All coordinates are J2000,  $M_0$  has units of  $M_\odot$ , and  $\sigma_0$  has units of  $\text{km s}^{-1}$ . RA<sub>\*</sub> and Dec<sub>\*</sub> are the coordinates of the COS sight line.

**Table 3.** Detections/non-detections in group sight lines

Group	$\rho/R_0$	AGN	Absorption component notes
(1)	(2)	(3)	(4)
12833	0.9	RBS711	strong H I; no O VI
16803	0.5	SDSS15403	weak H I at $-1036 \text{ km s}^{-1}$ ; partial LLS blocks O VI
19670	0.9	SBS0956	strong H I; no O VI
25124	0.4	B1612	2 strong H I, 1 possible BLA; O VI aligned with BLA
32123	1.1	SDSS1333	3 strong H I, 1 weak BLA; 1 weak O VI; 1 Si III
36001	0.3	SDSS1028	3 strong H I; 1 weak O VI; 1 Si III; probably aligned
44564	1.3	CSO1022	nothing
44565	1.0	CSO1022	nothing
44726	1.4	CSO1080	strong H I at $+1200 \text{ km s}^{-1}$ ; no O VI
44739	1.1	FBQS1519	4 strong H I; 2 weak O VI, 1 with Si III; probably aligned
44858	1.1	FBQS1519	strong H I; moderate O VI; slight misalignment
50433	1.1	FBQS1030	nothing

NOTE—Column 2 lists the impact parameter between the SDSS group barycenter (Table 2) and the QSO sight line, normalized by the group virial radius.

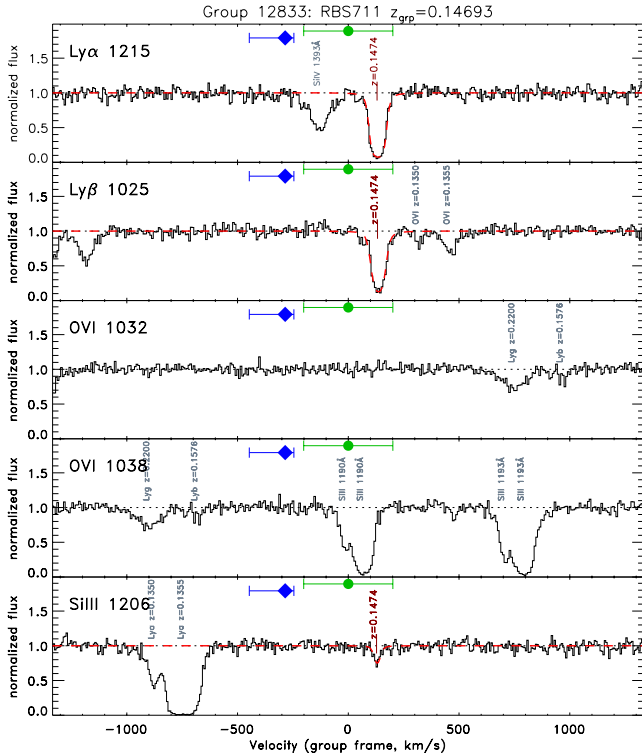


**Figure 1.** H I, O VI, and Si III absorption within  $\pm 2.5\sigma_0$  of group 12833. The panels are centered on the SDSS group redshifts (green circles), and use the SDSS velocity dispersion,  $\sigma_0$ , from Table 2. Blue diamonds show the group redshift and its uncertainty derived from our updated Monte Carlo analysis (Table 6). Strong, narrow H I is seen at  $\Delta v_{\text{abs}} = +129 \text{ km s}^{-1}$  with no corresponding O VI. A weak Si III feature aligned with the H I absorption shows the existence of enriched, photo-ionized gas. Absorption features unrelated to the galaxy group are identified in gray with either wavelengths (for Galactic features) or redshifts (for unrelated IGM lines).

shifts and uncertainties from Table 6 (see Section 4.3 for details). Red dashed lines and labels indicate absorption near the group redshift, while gray labels indicate absorption at other redshifts including Galactic lines. The galaxy symbol indicates the velocity of the nearest galaxies within  $1.5R_{\text{vir}}$  of the sight line (3 cases only).

Discussions of the absorption toward each sight line are presented in Appendix A, including Table 10 which details line measurements of all H I and O VI lines detected within  $\pm 2.5\sigma_0$  of the SDSS group centers. In many cases, particularly for absorbers which fall at large velocity offsets from the group, these systems may be coincidental and not associated with the galaxy groups. We list these line parameters for completeness. The limiting factor on the velocity accuracy for individual absorbers, especially Ly $\alpha$  absorbers, is often set by the ability to de-convolve complex line profiles into individual components. A complete discussion of the line

identification and measurement techniques is found in Danforth et al. (2016).

### 3.1. Metal-line Absorbers

As listed in Table 10 (see Appendix A) and shown in Figure 1, metal lines are detected in two-thirds (12 out of 18) of the absorption components. O VI is detected in seven of the metal-bearing systems as expected (Pratt et al. 2018) given the large impact parameters from individual galaxies designed into this study. The remaining absorbers contain significant low-ion absorption, usually Si III 1206 Å, similar to the photo-ionized absorbers in the CGM of individual galaxies. In the following discussion, the individual absorption components will be labeled by: [group/Ly $\alpha$  redshift].

Because this study was able to observe these targets only with COS/G130M, the higher ionization transitions normally seen in photo-ionized gas (Si IV and C IV) are not available, making a robust ionization model impossible for these absorbers. In lieu of that preferred solution, we assume that the five absorbers with only low ions (usually Si III) are close to photo-ionization equilibrium (PIE), with a characteristic gas temperature of  $\sim 20,000 \text{ K}$  as a very rough estimate. These absorbers are 12833/0.14743; 25124/0.18528, 32123/0.15874, 36001/0.18585 (C III is the only metal line detected) and 44739/0.11706. Three absorbers are detected in H I and O VI only, and have O VI and H I line widths consistent with warm gas; their characteristic temperatures are derived in Section 3.2.

This leaves four absorbers with both Si III and O VI detected. For three (32123/0.16081; 36001/0.18527 and 44739/0.11537) of these four composite systems, both the O VI and Si III are too weak to provide any definitive information, so the temperatures of these absorbers are poorly estimated. By our automated measurement the first two of these three absorbers have  $b_{\text{OVI}} > b_{\text{HI}}$ , an unphysical situation if the H I and O VI reside in the same gas. Although the error bars on these measurements do overlap, the more straightforward solution is that the narrow H I ( $b \approx 25 \text{ km s}^{-1}$ ) is not co-located with the broader O VI ( $b \approx 30 \text{ km s}^{-1}$ ), but is associated with the Si III absorption.

We suspect that a BLA is present in the saturated Ly $\alpha$  profile that matches the O VI line widths in these two cases but the O VI profiles are too weak to provide tight enough constraints to specify the BLA parameters. Instead, we can set only very loose upper limits on the temperature of these two absorbers by assuming that the O VI line widths are entirely thermal:  $T < 8 \times 10^5 \text{ K}$  and  $T < 1 \times 10^6 \text{ K}$ , respectively. This assumption leaves the observed Si III lines and the narrow H I lines as low temperature, photo-ionized absorbers.

For the third system in this list (44739/0.11537),  $b_{\text{HI}} > b_{\text{OVI}}$  and Si III is much stronger than the O VI. In this case, a photo-ionization model seems plausible and no BLA is re-

**Table 4.** The Probable BLA in Group 25124

	$\lambda$ (Å)	$z$	$b$ (km s <sup>-1</sup> )	EW (mÅ)	log $N$ ( $N$ in cm <sup>-2</sup> )
#1	1440.89	0.18526	$37 \pm 4$	708	$15.89 \pm 0.41$
#2	1441.05	0.18540	$128 \pm 57$	140	$13.43 \pm 0.38$
#3	1441.41	0.18569	$18 \pm 7$	63	$13.15 \pm 0.19$

quired. In the fourth absorber (44739/0.11766) the O VI is very broad and symmetrical suggesting that a BLA is present and the absorber temperature is  $> 10^5$  K (see Section 3.2).

For the metal-free absorbers, no definitive ionization-state or temperature determination is possible, except for absorber 32123/0.16142, which has a very broad and symmetrical Ly $\alpha$  profile with a line width suggesting a temperature in CIE just barely exceeding  $10^5$  K. As discussed previously (Stocke et al. 2013; Werk et al. 2014; Keeney et al. 2017), absorbers with no metal lines detectable in these spectra means only that the metallicities are low, typically  $\lesssim 10\%$  Solar metallicity, so that some metals may well be present in these six “metal-free” absorbers as well.

### 3.2. Presence of Broad Ly $\alpha$ Absorbers (BLAs)

The spectra shown in Figure 1 and absorptions described in Table 10 use the automated line-finding and measurement program described in Danforth et al. (2016). However, that routine is not well-suited to the detection of broad, shallow components in complex Ly $\alpha$  profiles, which can indicate the presence of warm-hot gas in these groups. Since Paper 2 found evidence linking systems containing broad BLAs as well as broad, shallow O VI absorption with galaxy groups, it is important to establish how many absorbers found here are consistent with possessing BLAs and thus with warm-hot gas in these groups.

To investigate the possibility that BLAs are present in these spectra, the three Ly $\alpha$  lines were refit for cases in which the O VI absorption suggests the presence of warm gas (see procedure developed in Papers 1 and 2 using the H I and O VI absorptions only). Briefly, the velocity and  $b$ -value of the O VI lines are used to constrain the wavelength and width of a potential BLA. The high-S/N ratio of these spectra is a necessity for this procedure.

*Group 25124*—The presence of a BLA is suggested in this case by an offset in the velocity centroid between the strong, broad, symmetrical O VI 1038 line compared to the two H I components and low-ionization metal ions. The stronger O VI line is blended with a Ly10 absorption at  $z=0.330$  (see Figure 1). Using the location and width of the O VI 1038 Å

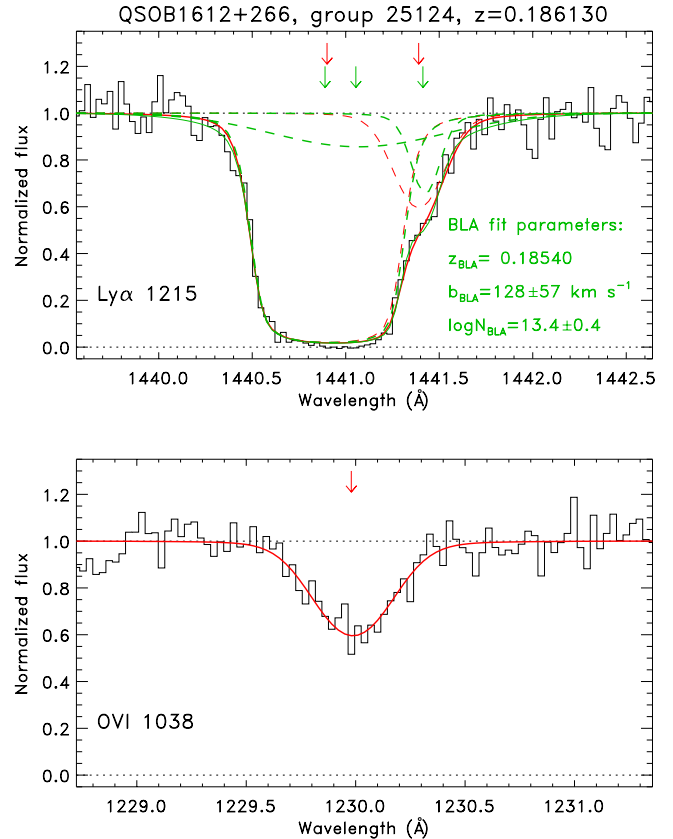


**Figure 2.** A BLA in the absorption associated with group 25124. Nominal fits are shown in solid red lines for Ly $\alpha$  and O VI 1038 Å (the O VI 1032 Å line is blended with Ly10 at a different redshift as discussed in the text) with red arrows marking the velocities. Individual components are shown as dashed lines. The green line shows the Ly $\alpha$  profile refitted with a third component centered at the same velocity as the broad, symmetrical O VI absorber; individual velocity components for this second fit are shown as dashed lines. The green arrows indicate the positions of the new Ly $\alpha$  components. The BLA has best-fit parameters shown in the plot, with a large  $b$ -value implying warm gas temperatures ( $T \approx 8 \times 10^5$  K, but with considerable uncertainty).

line, the Ly $\alpha$  profile was refit and a BLA matching the O VI can be present (see Figure 2 and Table 4). The N II, Si II and Si III lines follow the narrow H I absorption, as does the blue component of the C III line; the redward C III line and the N III line match the location of the BLA and O VI. The narrower blue component likely has a low temperature consistent with PIE, and is closely associated with a nearby  $2L^*$  galaxy 168 kpc ( $0.8 R_{\text{vir}}$ ) away. Using the measured  $b$ -values for the BLA and O VI in this case suggests a gas temperature in CIE of  $T \approx 8 \times 10^5$  K. This BLA may be associated either with the nearby galaxy or the entire galaxy group, since the velocity difference between the broad and narrow components suggest different physical locations for these absorbers.

*Group 32123*—In this sight line there are two possibilities for BLAs. One at  $z = 0.16081$  contains broad O VI absorption seen in both lines of the doublet but at low-S/N. A BLA corresponding to this O VI can be fit within the Ly $\alpha$  absorption complex, but is not well-constrained; i.e., we can set only a very loose upper limit on temperature ( $T < 8 \times 10^5$  K) by assuming that the observed O VI line width is entirely thermal. More interesting is a possible, metal-free BLA absorber at  $z = 0.16142$ , whose symmetrical line width suggests a temperature of  $1.5 \times 10^5$  K,

*Group 36001*—In this spectrum at  $z = 0.18527$  there is a weak, broad O VI 1032 Å absorber, too weak to be detected in the 1038 Å line. While a BLA be present, its parameters are not well-constrained. As with the possible warm absorber in group 32123, we set a very loose upper limit of  $T < 1 \times 10^6$  K by assuming that the OVI line width is entirely thermal. Two possibilities seem equally plausible; a warm absorber with a BLA and broad O VI and a cool absorber with narrow H I and Si III are both present, or there is a single cool absorber which contains both photo-ionized Si III and O VI. There is also another H I plus O VI absorber possibly associated with group 36001 at a relative velocity of  $-906 \text{ km s}^{-1}$ ,  $> 2.5 \sigma_{\text{grp}}$  from the group mean velocity and thus outside the velocity bounds we have set for association (see Section 5.1). In this case, the H I and O VI have nearly the same line widths suggesting a low temperature and a turbulent medium, but a BLA associated with the O VI could be present in the saturated Ly $\alpha$  profile. Assuming that the O VI width is entirely thermal sets a firm upper limit of  $T < 1 \times 10^6$  K.

*Group 44739*—In this case, a very broad, shallow O VI 1032 Å line is well-aligned with a narrow H I line that also has moderately strong Si III (see Figure 1 and Table 10) at  $z = 0.11766$ . While a BLA could be present in this case, and is suggested by the breadth of the symmetrical O VI doublet lines, the BLA is predicted to have  $b_{\text{HI}} \approx 200 \text{ km s}^{-1}$  assuming minimal gas turbulence or velocity components in the O VI. This line width is so broad that the predicted BLA would be undetectable, and suggests  $T > 10^6$  K. In this scenario, a cool, photo-ionized absorber would also be present at nearly the same velocity, based on the narrow H I and Si III.

*Group 44858*—In this case, the original line fit listed in Table 10 for this  $z = 0.12567$  absorber does not change by applying the method used above. The somewhat broad H I and O VI lines indicate a gas temperature just slightly in excess of  $10^5$  K; The nearest galaxy is  $7R_{\text{vir}}$  away, making a group association with this gas most likely.

## 4. CHARACTERIZING THE SDSS GROUPS PROBED BY THESE SIGHT LINES

### 4.1. MOS Observations

While the acquisition and analysis of the galaxy redshift and magnitude data is presented and described in detail in Keeney et al. (2018), here we summarize the basic parameters of those observations as they apply to the group membership analysis. For all of the target sight line fields, the SDSS spectroscopic survey data is used for the brighter galaxies ( $r \leq 17.8$ ), while new multi-object spectroscopy (MOS) on fainter galaxies was obtained specifically for this program at the MMT Observatory 6m using the Hectospec MOS (Fabricant 2005) and at the WIYN 3.5m telescope using the HYDRA MOS.

These groups have modest numbers of SDSS galaxies ( $N_0 = 3-10$ ), so we designed the MOS survey to increase the number of group members to  $N \geq 20$  per group to better constrain basic group parameters, including velocity dispersion, centroid position and extent on the sky, which can be used to infer, e.g., the group halo mass and group virial radius. Our goal for these observations was not very high completeness, but rather a fair sampling of potential group members so that the group is well-characterized. The overall completeness of these observations is  $\geq 60\%$  for these target fields, where the overall completeness is defined to be the fraction of all targets with  $g < 20$  within  $20'$  of the sight line for which redshifts are available from this survey or other sources (Keeney et al. 2018, see their Table 8 for individual field completeness values and other related quantities). These limits correspond to group galaxies at  $L \geq 0.2L^*$ , although only a small percentage of those galaxies with redshifts in-hand are actually at the redshifts of these groups; it is likely that a similarly small percentage of unobserved galaxies are also at the group redshift.

At WIYN/HYDRA we used the 600@10.1 grating centered at 5200 Å ( $\mathcal{R} \approx 1200$  from 3800-6600 Å); the S/N of these spectra is  $9_{-3}^{+5}$  per pixel when the galaxy  $g$ -band magnitude range is  $19.4_{-0.7}^{+0.5}$ . At MMT/Hectospec, we used the 270gpm grating to achieve  $\mathcal{R} \approx 1000$  from 3700-9100 Å; the S/N of these spectra is  $7_{-3}^{+6}$  per pixel when the galaxy  $g$ -band magnitude range is  $19.8_{-0.8}^{+0.7}$ . We chose our wavelength coverage to ensure good sensitivity to Ca II H & K absorption at  $z \approx 0$  to maximize the return of accurate redshifts for absorption-line galaxies in these low- $z$  galaxy groups.

The design criterion to obtain redshifts for a representative sample of  $> 20$  group members is achieved in all but two cases, group 36001 (6 group galaxies; see Table 8) and group 44726 (8 group members; Table 8). Group 36001 has only 57% overall completeness, but Group 44726 easily exceeds the design completeness level (60%) for this survey. Since the MOS on these two fields did not differ signifi-

cantly in completeness from the others, these are truly sparse groups, not fields with high incompleteness.

#### 4.2. Nearest Galaxies to the Absorbers

For all of our groups, we have located the galaxy with  $|\Delta v_{\text{abs}}| \leq 1000 \text{ km s}^{-1}$  nearest to the QSO sight line to determine whether an individual galaxy is more likely associated with the observed absorption than the group as a whole. While our original criteria for choosing sight lines excluded QSOs whose impact parameter to a bright group galaxy was  $\leq 1.5 R_{\text{vir}}$ , deeper MOS found two cases where fainter galaxies were found close to the sight line at the redshift of the absorber.

Table 5 lists the properties of the nearest galaxy to each absorber detected in our *HST*/COS spectra at or near the group redshift. Column 9 lists the rest-frame velocity difference between the absorber and galaxy; i.e.,  $\Delta v_{\text{abs}} = c(z_{\text{gal}} - z_{\text{abs}})/(1 + z_{\text{abs}})$ . The final column lists the galaxy's three-dimensional distance from the absorber,  $D$ , normalized by the galaxy's virial radius,  $R_{\text{vir}}$ . The virial radius is estimated from the galaxy's rest-frame  $g$ -band luminosity,  $L_{\text{gal}}^1$ , as detailed in Stocke et al. (2013). The three-dimensional absorber-galaxy distance is calculated using:

$$D^2 = \rho^2 + D_z^2 \quad (1)$$

where  $\rho$  is the galaxy's impact parameter with respect to the QSO sight line and  $D_z$  is the distance along the line of sight in Mpc. The line-of-sight distance is calculated using a reduced Hubble flow model such that

$$D_z = \begin{cases} 0 & |\Delta v_{\text{abs}}| \leq v_{\text{red}} \\ (|\Delta v_{\text{abs}}| - v_{\text{red}})/H_0 & |\Delta v_{\text{abs}}| > v_{\text{red}} \end{cases} \quad (2)$$

We assume  $v_{\text{red}} = 400 \text{ km s}^{-1}$  for consistency with previous studies of galaxy-absorber associations (see, e.g., Paper 2, Prochaska et al. 2011; Stocke et al. 2013; Keeney et al. 2017, 2018; Pratt et al. 2018). This convention is used to account for possible peculiar velocities between galaxies and absorbers (e.g., due to outflow/infall); the reduced Hubble flow cutoff value was chosen to match the maximum rotation speeds of the most massive galaxies.

There are only two cases for which a galaxy is close to the sight line in units of virial radii: group 25124 ( $0.8 R_{\text{vir}}$  from the sight line) and group 32123 ( $0.6 R_{\text{vir}}$  away). Based on the observed distributions of nearest and next-nearest neighbors to a large sample of absorbers, Keeney et al. (2017) find that low- $z$  absorption can be attributed with confidence to the

CGM of individual galaxies only when  $D/R_{\text{vir}} \lesssim 1.4$ . This suggests that some of the absorption in groups 25124 and 32123 is likely associated with individual galaxies in Table 5 rather than the group itself.

To investigate this uncertainty, the sight line towards FBQS 1010+3003 was used as a test case for the current study. This sight line was selected in the same way as the current study, except that a bright SDSS galaxy at the group redshift was known to be present close to the sight line prior to deeper MOS. A relatively high-S/N (15-20) COS spectrum was in-hand for FBQS 1010+3003 from the science program of the COS-GTOs (Stocke et al. 2013; Keeney et al. 2017) and a deep galaxy survey of the region is available from Keeney et al. (2018). A detailed examination in Stocke et al. (2017) tried to distinguish between an absorber association with an individual  $2.7 L^*$  galaxy located  $1.0 R_{\text{vir}}$  from the absorber and a small group of nearby galaxies, of which the individual galaxy is not a member. For an O VI-only absorber in the FUV spectrum of FBQS 1010+3003, a better match both in sky position and velocity was found for the individual galaxy association. For comparison, the nearest galaxy data for this case is reproduced at the bottom of Table 5 and labeled group 49980. The O VI-only absorber is at  $z = 0.11351$ ; the other absorbers are detected in Ly $\alpha$ , some of which likely are associated with the galaxy group (see Stocke et al. 2017 for details).

The situation is not so clear for groups 25124 and 32123. For the  $z = 0.18529, 0.18540$  (the BLA plus O VI absorber),  $0.18569$  Ly $\alpha$  complex in group 25124, the high and low-ion components cannot be at the same location given their velocity difference. All three components can be associated with the single galaxy in Table 5, or the BLA plus broad O VI can be associated with the galaxy group. To be conservative, we associate all three with the galaxy and count group 25124 as a non-detection. The case of group 32123 is somewhat clearer in that a total of four absorbers are present; the two at lower velocity match the velocity of the nearest galaxy (see Table 5), which is not a group member. The other two absorbers are too far away in velocity to be plausibly associated with this same galaxy. For these two absorbers, which include an H I and O VI absorber and a BLA (see Figure 1), the closest galaxy is  $1.8 R_{\text{vir}}$  away, so we identify the absorption with the galaxy group.

The individual galaxies associated with absorbers near the redshifts of groups 25124 and 32123 are both early types, with specific star formation rates consistent with being passive galaxies ( $\text{sSFR} < 10^{11} \text{ yr}^{-1}$ ). Additionally, the nearest galaxy in the FBQS 1010+3003 sight line is an Sa galaxy whose sSFR suggests that it is also passive. We detect O VI absorption in all three of these cases as well as a few other cases in previous investigations (Paper 2 and Keeney et al. 2017), but the COS-Halos collaboration found very few O VI

<sup>1</sup> As in Keeney et al. (2017), we adopt  $M_g^* = -20.3$  (Montero-Dorta & Prada 2009, corrected to  $H_0 = 70 \text{ km s}^{-1}$ ) with  $K$ -corrections from Chilingarian, Melchior, & Zolotukhin (2010) and Chilingarian & Zolotukhin (2012).

**Table 5.** Nearest Galaxy Properties

Group	$z_{\text{abs}}$	RA	Dec	$z_{\text{gal}}$	$L_{\text{gal}}$	$R_{\text{vir}}$	$\rho$	$\Delta v_{\text{abs}}$	$D/R_{\text{vir}}$
		( $^{\circ}$ )	( $^{\circ}$ )		( $L^*$ )	(kpc)	(kpc)	( $\text{km s}^{-1}$ )	
(1)	(2)	(3)	(4)	(5)	(6)	(7)	(8)	(9)	(10)
12833	0.14743	129.343638	44.390149	0.14844	2.6	248	772	263	3.1
16803	0.14497	235.046611	-2.039641	0.14549	1.2	191	525	136	2.7
19670	0.13388	149.958823	50.778650	0.13346	1.1	185	499	-111	2.7
25124	0.18529	243.531018	26.556435	0.18507	1.9	223	168	-55	0.8
	0.18569							-159	
32123	0.15874	203.271113	45.315150	0.15853	5.0	311	175	-54	0.6
	0.16081	203.211036	45.300789	0.16102	0.78	167	299	54	1.8
	0.16142							-103	
36001	0.18429	156.986890	21.245411	0.18432	2.7	252	1239	7	4.9
	0.18494	156.986060	21.369490	0.18658	2.0	228	887	414	4.0
	0.18527							-323	3.9
	0.18585	157.086777	21.355513	0.18752	4.7	304	382	422	1.6
44564/44565	...	...	...	...	...	...	...	...	...
44726	...	...	...	...	...	...	...	...	...
44739	0.11537	229.950843	28.626721	0.11502	1.1	185	350	-94	1.9
	0.11706	229.844996	28.711684	0.11801	1.4	203	661	254	3.3
	0.11766							93	
	0.11795							16	
44858	0.12551	230.069021	28.838277	0.12638	4.0	287	2006	231	7.0
	0.12567							189	
50433	...	...	...	...	...	...	...	...	...
49980	0.11351	152.472930	30.033939	0.11345	2.7	252	254	-16	1.0
	0.11381							-96	
	0.11466							-325	
	0.11675	152.426382	29.942452	0.11551	3.5	274	1005	-332	3.7

NOTE—An individual galaxy can be identified as the nearest galaxy to several Ly $\alpha$  absorbers; when this occurs the galaxy properties are listed once and only the galaxy-absorber velocity difference is updated for subsequent absorbers. Similarly, some groups have no absorption within 1000  $\text{km s}^{-1}$  of the group centroid (see Table 10), as indicated by the “...” symbol in each column.

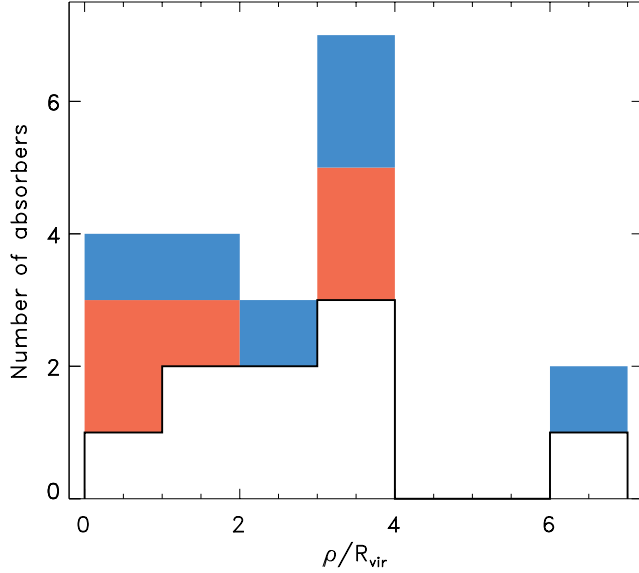


**Figure 3.** Impact parameters of nearest galaxies to the absorbers in this survey. Open boxes are metal-free absorbers; blue boxes indicate the presence of O VI while the red boxes are absorbers with only low ions. The FBQS 1010+3003 field, which has a close galaxy at  $\rho/R_{\text{vir}} < 1$ , is included in this compilation despite being chosen somewhat differently from the rest of the sample (see text).

absorptions associated with passive galaxies in their sample (Tumlinson et al. 2011). The reported absence of O VI is almost certainly due to the COS-Halos spectra having lower S/N than the present data and the data obtained in the COS-GTO program. While O VI is undoubtedly present around most passive galaxies, the larger impact parameters of those absorbers suggests an association with the entire group to which the galaxy is a member (Paper 2 and Keeney et al. 2017). The rather constant covering fraction of 50-70% for absorption-line galaxies as a function of impact parameter out to several virial radii ( $4R_{\text{vir}}$  or  $\sim 1$  Mpc) suggests that the gaseous structure creating the absorption around passive galaxies is much larger than an individual galaxy CGM (see Figures 7 and 8 in Keeney et al. 2018).

For the other groups, despite the much deeper MOS obtained by us, there are no galaxies close to the sight lines, making the claim that these absorbers are associated with the entire galaxy group strong. The full range of nearest galaxy impact parameters is shown as a histogram in Figure 3. The bins are in units of virial radii, and open symbols indicate H I-only absorption, red indicates low-ion without O VI, and blue indicates O VI absorption with or without low ions. The FBQS 1010+3003 field listed at the bottom as group 49980 is included for completeness, despite having a previously known galaxy close to the sight line (see Stocke et al. 2017).

In summary, while all the absorptions listed in Table 5 could be ascribed to the foreground groups targeted by this

study, we conservatively associate the absorption complex in group 25124 and two of four absorbers near group 32123 to the individual closest galaxy listed in Table 5. We associate the other two absorbers near group 32123 (those not close to an individual galaxy) with the entire group. That is, we count group 25124 as a non-detection, while group 32123 is counted as a detection because only one of the two absorber systems detected is associated with an individual galaxy.

#### 4.3. Group-Finding Algorithm and Parameters

The group-finding algorithm employed here differs somewhat from that presented in our previous group studies. Paper 2 and Stocke et al. (2017) used a friends-of-friends (FoF) algorithm to create an initial guess at group membership, which was subsequently refined by a “virialization” step. Here, we remove the initial FoF step altogether and use Monte Carlo simulations to explore the systematic effects of initial parameters in the virialization procedure.

Our group-finding algorithm assumes a group mass-to-light ratio of  $\Upsilon_{\text{grp}} \equiv M_{\text{grp}}/L_{\text{grp}}$ , which allows us to estimate the group’s virial radius,  $R_{\text{grp}}$ , and velocity dispersion,  $\sigma_{\text{grp}}$ , based on the total luminosity of the group members:

$$L_{\text{grp}} = \sum_{i=1}^{N_{\text{grp}}} L_i \quad (3)$$

$$M_{\text{grp}} = \Upsilon_{\text{grp}} \left( \frac{L_{\text{grp}}}{L^*} \right) \times 10^{10} M_{\odot} \quad (4)$$

$$\begin{aligned} R_{\text{grp}} &= \left( \frac{3M_{\text{grp}}}{4\pi\Delta_{\text{crit}}\rho_{\text{crit}}} \right)^{1/3} \\ &= 957 \left( \frac{M_{\text{grp}}}{10^{14} M_{\odot}} \right)^{1/3} \text{ kpc} \end{aligned} \quad (5)$$

$$\begin{aligned} \sigma_{\text{grp}} &= \sqrt{\frac{GM_{\text{grp}}}{3R_{\text{grp}}}} \\ &= 387 \left( \frac{M_{\text{grp}}}{10^{14} M_{\odot}} \right)^{1/3} \text{ km s}^{-1} \end{aligned} \quad (6)$$

We assume  $\Delta_{\text{crit}} = 200$  and  $\rho_{\text{crit}} = 9.205 \times 10^{-30} h_{70}^2 \text{ g cm}^{-3}$  (Shull, Smith, & Danforth 2012), and ignore any evolution with redshift since our groups are all located at  $z < 0.2$ .

We start with an initial group position, redshift, and mass close to those in Table 2, then search for galaxies that are located within a specified distance of the group center on the plane of the sky and in velocity space (see Section 4.3.1 for details). All galaxies in this volume are assumed to be group members, and new group positions, redshifts, and masses are estimated based on the revised membership. These updated group properties are used as the starting point for the next iteration of the group finder, and the algorithm iterates until it converges (i.e., the identities of group members do not change from one iteration to the next), which is typically achieved in five or fewer iterations.

As mentioned above, all galaxies within our search volume are considered to be group members, so it is important to choose the boundaries carefully. For the boundary on the plane of the sky, we adopt the group splashback radius<sup>2</sup>,  $R_{\text{sp}} \sim \Omega_{\text{m}}^{-1/3} R_{\text{grp}} \approx 1.5 R_{\text{grp}}$  (Diemer 2017). For the boundary in velocity space, we adopt  $\pm 2\sigma_{\text{grp}}$  from the group redshift. This value was chosen by analyzing a large mock catalog, where galaxies were placed inside dark matter halos in an  $N$ -body simulation and given velocities that trace the velocities of dark matter particles; this analysis suggests that  $> 99\%$  of all satellite galaxies are located within  $2\sigma_{\text{grp}}$  of the parent halo’s velocity.

#### 4.3.1. Monte Carlo Analysis

The basic group properties that we wish to derive are its position on the sky, redshift, and membership. Unfortunately, these properties depend sensitively on nuisance parameters<sup>3</sup> whose values are unknown or ill-constrained. We employ Monte Carlo simulations to marginalize over these parameters by allowing them to vary over a range of values.

Our initial estimates of the group location, redshift, and mass come from the SDSS analysis in Table 2. The uncertainties in the group position and redshift are the uncertainties in the mean value for the SDSS group members (i.e., they are proportional to  $N_0^{-1/2}$ ). We assume Gaussian priors for these values, with mean and standard deviation from Table 2.

The uncertainties in the group mass were estimated by running the SDSS FoF algorithm of Paper 3 on mock galaxy catalogs where the true halo masses were known. Our prior on  $\log M_0$  assumes a Gaussian with mean and standard deviation listed in Table 2 that is then weighted by a halo mass function (HMF) to account for the expectation that low-mass halos are more common than high-mass halos. The HMF was evaluated at  $z = 0.15$  with  $\Delta_{\text{crit}} = 200$ , cosmological parameters from *Planck* (Planck Collaboration et al. 2014), and fitting functions from Tinker et al. (2008) using the online HMF calculator of Murray, Power, & Robotham (2013).

We adopt a Gaussian prior on  $\log \Upsilon_{\text{grp}}$  with a mean of 2.5 and a standard deviation of 0.3 dex, which is a good characterization of the  $g$ -band values from Proctor et al. (2015). While it is typically assumed that redder optical magnitudes (i.e., SDSS  $r$ - or  $i$ -band) correlate more strongly with an individual galaxy’s stellar mass,  $\Upsilon_{\text{grp}}$  shows no difference in correlation for the SDSS  $g$ -,  $r$ -, and  $i$ -bands (i.e., the Gaussian distribution of  $\log \Upsilon_{\text{grp}}$  has a width of 0.3 dex in all three

bands; Proctor et al. 2015). Thus, we retain the  $g$ -band as our standard of reference for all galaxy luminosities for consistency with past studies (Paper 2, Stocke et al. 2013, 2017; Keeney et al. 2017, 2018).

For each SDSS galaxy group in Table 2, we perform 10,000 Monte Carlo realizations, allowing the nuisance parameters to vary as described above. For each realization, we record the values of the nuisance parameters for that trial and the group members identified by our algorithm. From these, physically-meaningful values such as the group position, redshift, and luminosity,  $M_{\text{grp}}$ ,  $R_{\text{grp}}$ ,  $\sigma_{\text{grp}}$  are derived.<sup>4</sup> The observed size ( $R_{\text{obs}}$ ) and velocity dispersion ( $\sigma_{\text{obs}}$ ) of the group members, and the impact parameter between the group center and the QSO sight line ( $\rho_*$ ) also are derived. The ensemble of all realizations are then analyzed to determine the range of the derived quantities for each galaxy group.

As in Paper 2 and Stocke et al. (2017), we have used robust estimators of the group properties, as initially defined by Beers, Flynn, & Gebhardt (1990). The position of the group on the sky and its redshift are calculated with the bi-weight location estimator, and the observed velocity dispersion of the group ( $\sigma_{\text{obs}}$ ) is calculated using the “gapper” scale estimator as illustrated in Equations 3-4 of Paper 2. Additionally, we estimate the observed size of the group ( $R_{\text{obs}}$ ) by calculating each group member’s impact parameter with respect to the group center and adopting the 68th percentile value as  $R_{\text{obs}}$  (i.e., 68% of the identified group members are within a projected distance of  $R_{\text{obs}}$  from the group center). Unlike  $\sigma_{\text{obs}}$ , we do not assign any physical meaning to  $R_{\text{obs}}$ ; it is merely an empirical means of assessing whether the identified group is approximately the size that we would expect given its inferred mass (i.e.,  $R_{\text{obs}} \sim R_{\text{grp}}$ ).

Table 6 summarizes our Monte Carlo realizations. Column 1 lists the group identifier, columns 2 & 3 the sky position in degrees, and column 4 the redshift ( $z_{\text{grp}}$ ). Column 5 lists the number of group members ( $N_{\text{grp}}$ ), column 6 the total group luminosity ( $L_{\text{grp}}$ ; Equation 3), and column 7 the total group mass ( $M_{\text{grp}}$ ; Equation 4). Columns 8 and 9 are the observed group radius ( $R_{\text{obs}}$ ) and velocity dispersion ( $\sigma_{\text{obs}}$ ). Column 11 lists the ratio  $R_{\text{obs}}/R_{\text{grp}}$ , and column 12 the ratio  $\sigma_{\text{obs}}/\sigma_{\text{grp}}$ , where  $R_{\text{grp}}$  and  $\sigma_{\text{grp}}$  are calculated using Equation 5 and Equation 6, respectively. Columns 10 and 13 list the sight line impact parameter from the group centroid in kpc and as a fraction of  $R_{\text{grp}}$ . Details of individual groups are discussed in Appendix B.

<sup>2</sup> The “splashback radius” is the apocenter of satellites during their first orbit after falling into a dark matter halo, and has been suggested as a physically motivated definition of a halo boundary (Adhikari, Dalal, & Chamberlain 2014; Diemer & Kravtsov 2014; More, Diemer, & Kravtsov 2015).

<sup>3</sup> We use the term “nuisance parameter” in the statistical sense; i.e., a model parameter that is not of physical interest but must be accounted for to constrain parameters that are physically interesting.

<sup>4</sup> We caution the reader that we are using different notation than Paper 2 and Stocke et al. (2017). We now call the group velocity dispersion expected based on its mass  $\sigma_{\text{grp}}$  instead of  $\sigma_{\text{vir}}$ , and the observed velocity dispersion  $\sigma_{\text{obs}}$  instead of  $\sigma_{\text{grp}}$ . We believe that this new nomenclature is more transparent and internally consistent, and apologize for any confusion.

Table 6. Range of Group Properties

Group	RA ( $^{\circ}$ )	Dec ( $^{\circ}$ )	$z_{\text{grp}}$	$N_{\text{grp}}$	$L_{\text{grp}}$ ( $L^*$ )	$\log M_{\text{grp}}$	$R_{\text{obs}}$ (kpc)	$\sigma_{\text{obs}}$ ( $\text{km s}^{-1}$ )	$\rho_*$ (kpc)	$R_{\text{obs}}/R_{\text{grp}}$	$\sigma_{\text{obs}}/\sigma_{\text{grp}}$	$\rho_*/R_{\text{grp}}$
(1)	(2)	(3)	(4)	(5)	(6)	(7)	(8)	(9)	(10)	(11)	(12)	(13)
12833	129.400 $^{+0.013}_{-0.013}$	44.282 $^{+0.010}_{-0.007}$	0.14584 $^{+0.00015}_{-0.00062}$	50 $^{+19}_{-21}$	88.2 $^{+25.8}_{-27.0}$	14.44 $^{+0.41}_{-0.45}$	1395 $^{+637}_{-436}$	434 $^{+15}_{-119}$	1741 $^{+69}_{-48}$	1.02 $^{+0.06}_{-0.05}$	0.78 $^{+0.06}_{-0.20}$	1.33 $^{+0.47}_{-0.29}$
16803	234.994 $^{+0.005}_{-0.026}$	-2.098 $^{+0.009}_{-0.011}$	0.14845 $^{+0.00017}_{-0.00009}$	54 $^{+13}_{-18}$	94.9 $^{+24.1}_{-29.6}$	14.48 $^{+0.40}_{-0.45}$	1254 $^{+333}_{-175}$	445 $^{+57}_{-76}$	824 $^{+297}_{-55}$	0.90 $^{+0.19}_{-0.07}$	0.80 $^{+0.18}_{-0.14}$	0.59 $^{+0.14}_{-0.06}$
19670	150.178 $^{+0.028}_{-0.026}$	50.784 $^{+0.002}_{-0.007}$	0.13442 $^{+0.00042}_{-0.00072}$	69 $^{+24}_{-21}$	87.0 $^{+22.0}_{-24.8}$	14.43 $^{+0.40}_{-0.43}$	1144 $^{+606}_{-154}$	494 $^{+76}_{-91}$	1651 $^{+136}_{-158}$	0.90 $^{+0.09}_{-0.08}$	0.91 $^{+0.13}_{-0.11}$	1.18 $^{+0.54}_{-0.20}$
25124	243.538 $^{+0.005}_{-0.015}$	26.687 $^{+0.002}_{-0.006}$	0.18576 $^{+0.00107}_{-0.00009}$	30 $^{+10}_{-14}$	80.5 $^{+24.5}_{-19.1}$	14.40 $^{+0.42}_{-0.43}$	1380 $^{+242}_{-521}$	451 $^{+13}_{-143}$	1586 $^{+19}_{-62}$	0.95 $^{+0.11}_{-0.09}$	0.77 $^{+0.20}_{-0.15}$	1.24 $^{+0.32}_{-0.35}$
32123	203.047 $^{+0.020}_{-0.012}$	45.425 $^{+0.008}_{-0.039}$	0.15958 $^{+0.00031}_{-0.00014}$	19 $^{+17}_{-0}$	32.8 $^{+31.7}_{-0.7}$	14.22 $^{+0.59}_{-0.33}$	837 $^{+667}_{-0}$	316 $^{+129}_{-3}$	1942 $^{+1}_{-366}$	0.97 $^{+0.12}_{-0.12}$	0.88 $^{+0.10}_{-0.18}$	2.00 $^{+0.50}_{-0.92}$
36001	157.056 $^{+0.019}_{-0.003}$	21.339 $^{+0.018}_{-0.031}$	0.18760 $^{+0.00001}_{-0.00012}$	6 $^{+4}_{-1}$	20.0 $^{+12.3}_{-2.1}$	13.79 $^{+0.53}_{-0.36}$	728 $^{+334}_{-74}$	194 $^{+110}_{-24}$	297 $^{+179}_{-150}$	0.92 $^{+0.14}_{-0.11}$	0.57 $^{+0.15}_{-0.08}$	0.36 $^{+0.46}_{-0.23}$
44564	208.170 $^{+0.013}_{-0.012}$	36.275 $^{+0.005}_{-0.006}$	0.14609 $^{+0.00006}_{-0.00009}$	114 $^{+39}_{-38}$	132 $^{+58.0}_{-49.3}$	14.62 $^{+0.46}_{-0.50}$	1336 $^{+471}_{-200}$	547 $^{+84}_{-91}$	1545 $^{+126}_{-82}$	0.87 $^{+0.13}_{-0.06}$	0.88 $^{+0.19}_{-0.16}$	0.99 $^{+0.60}_{-0.32}$
44565	208.171 $^{+0.012}_{-0.012}$	36.277 $^{+0.004}_{-0.007}$	0.14611 $^{+0.00006}_{-0.00006}$	115 $^{+38}_{-35}$	134 $^{+57.0}_{-44.2}$	14.62 $^{+0.45}_{-0.47}$	1336 $^{+471}_{-183}$	557 $^{+74}_{-82}$	1535 $^{+115}_{-75}$	0.88 $^{+0.12}_{-0.07}$	0.89 $^{+0.17}_{-0.16}$	1.00 $^{+0.55}_{-0.32}$
44726	226.214 $^{+0.001}_{-0.066}$	29.833 $^{+0.007}_{-0.064}$	0.15233 $^{+0.00003}_{-0.00014}$	7 $^{+15}_{-0}$	11.0 $^{+18.1}_{-0.4}$	13.53 $^{+0.70}_{-0.40}$	188 $^{+852}_{-10}$	226 $^{+213}_{-4}$	1331 $^{+493}_{-6}$	0.37 $^{+0.65}_{-0.10}$	0.94 $^{+0.19}_{-0.14}$	2.03 $^{+0.83}_{-0.54}$
44739	229.822 $^{+0.019}_{-0.019}$	28.342 $^{+0.058}_{-0.006}$	0.11883 $^{+0.00017}_{-0.00040}$	62 $^{+44}_{-11}$	65.0 $^{+37.0}_{-6.7}$	14.31 $^{+0.49}_{-0.35}$	1144 $^{+658}_{-151}$	348 $^{+96}_{-63}$	2394 $^{+28}_{-416}$	1.01 $^{+0.06}_{-0.09}$	0.71 $^{+0.15}_{-0.10}$	1.98 $^{+0.62}_{-0.85}$
44858	230.084 $^{+0.035}_{-0.032}$	28.873 $^{+0.008}_{-0.008}$	0.12729 $^{+0.00082}_{-0.00024}$	80 $^{+23}_{-28}$	103 $^{+22.0}_{-23.0}$	14.52 $^{+0.39}_{-0.42}$	1313 $^{+248}_{-419}$	507 $^{+74}_{-134}$	2289 $^{+172}_{-31}$	0.87 $^{+0.05}_{-0.05}$	0.87 $^{+0.05}_{-0.12}$	1.61 $^{+0.78}_{-0.43}$
50433	157.732 $^{+0.003}_{-0.003}$	30.845 $^{+0.006}_{-0.001}$	0.13630 $^{+0.00006}_{-0.00006}$	25 $^{+7}_{-4}$	39.7 $^{+18.1}_{-3.0}$	14.10 $^{+0.38}_{-0.33}$	600 $^{+234}_{-38}$	343 $^{+27}_{-57}$	1781 $^{+11}_{-47}$	0.62 $^{+0.12}_{-0.08}$	0.82 $^{+0.11}_{-0.14}$	1.73 $^{+0.43}_{-0.42}$

NOTE.—Tabulated values are the median from the Monte Carlo realizations, and ranges are the 16th and 84th percentile values.  $M_{\text{grp}}$  has units of  $M_{\odot}$ , and  $\rho_*$  is the impact parameter between the group center and the COS sight line.

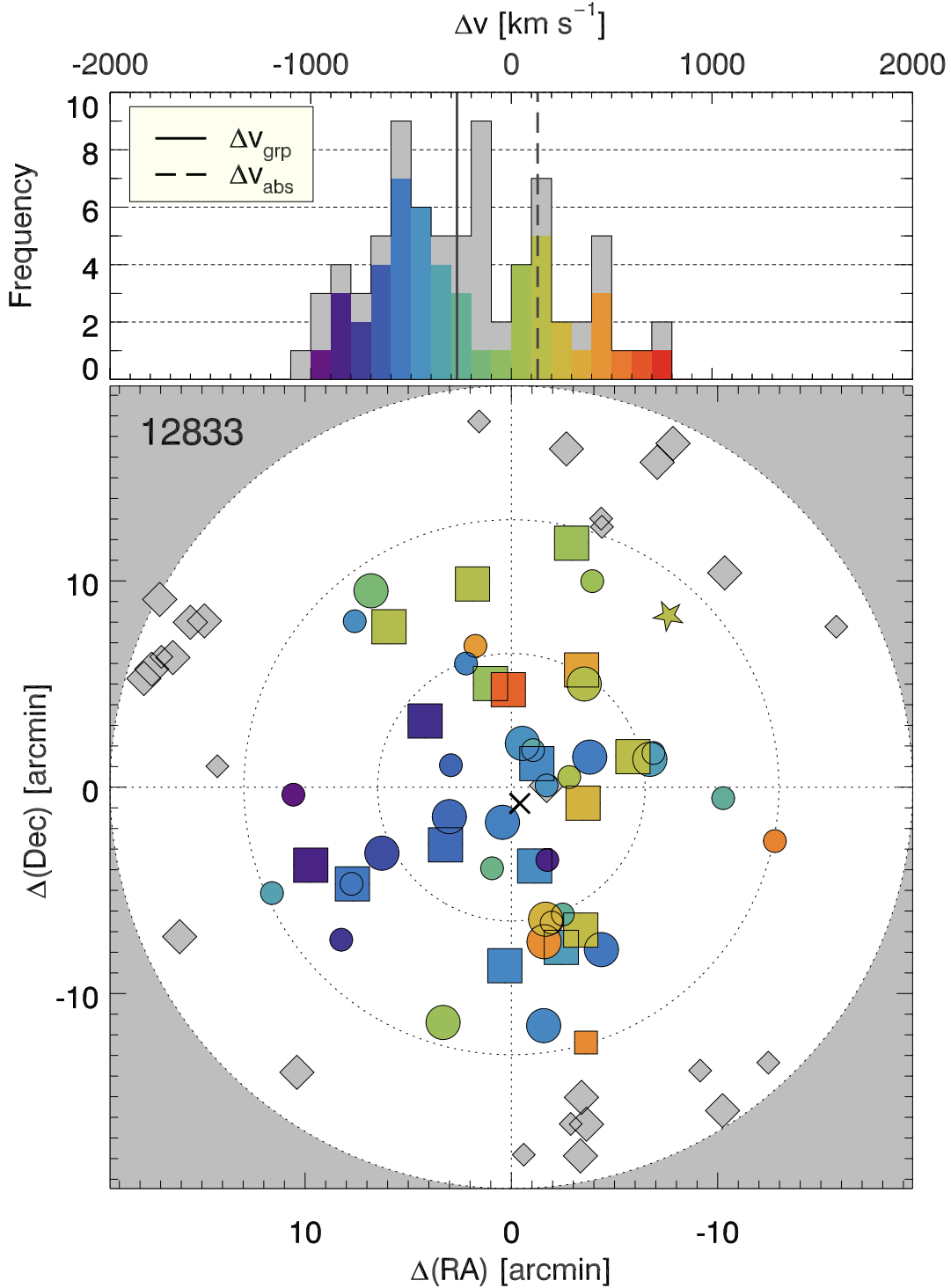


**Figure 4.** *Top:* Velocity histogram of galaxies near group 12833. Group members are color coded from purple to red for the lowest and highest redshift group members, respectively. Field galaxies are gray. The solid vertical line shows the group velocity centroid and dashed vertical lines show the positions of absorption in the *HST/COS* spectra. All velocities are calculated with respect to the initial estimate of the group redshift from the SDSS analysis in Table 2. *Bottom:* Distribution on the sky of galaxies near group 12833. Group members are colored as in the top panel. Gray diamonds represent field galaxies, squares represent SDSS galaxies, and circles represent new galaxy redshifts from our MOS campaign. The position of the group centroid on the sky is marked with an “x”, and the position of the *HST/COS* sight line is marked with a star. Circles are shown at 1 Mpc intervals, centered on the initial estimate of the group position from the SDSS analysis in Table 2.

**Table 7.** Members of Group 12833

Name	RA	Dec	$z_{\text{gal}}$	$L_{\text{gal}}$ ( $L^*$ )	Type	$\Delta\rho$ (kpc)	$\Delta v$ ( $\text{km s}^{-1}$ )	$f_{\text{mem}}$ (%)
(1)	(2)	(3)	(4)	(5)	(6)	(7)	(8)	(9)
rbs711_126_554	129.398389	44.325363	0.14572	0.575	A	323	-316	99.6
rbs711_135_607	129.383140	44.296795	0.14519	0.998	A	265	-455	99.5
1237654652565651620	129.394131	44.314455	0.14505	1.66	A	261	-492	99.5
rbs711_123_564	129.410462	44.330803	0.14518	1.05	C	340	-457	99.5
rbs711_143_470	129.334488	44.319729	0.14485	1.44	A	631	-544	99.4
rbs711_136_895	129.444666	44.229919	0.14614	0.519	C	627	-207	99.3
rbs711_132_770	129.432936	44.267044	0.14492	1.20	A	272	-525	99.3
rbs711_117_767	129.491115	44.313179	0.14454	0.757	A	484	-625	99.3
rbs711_124_864	129.492903	44.271641	0.14459	1.20	A	517	-612	99.3
rbs711_146_793	129.382281	44.236610	0.14369	0.584	C	610	-847	99.3
1237654652565586007	129.396584	44.231755	0.14514	4.72	A	618	-468	99.3
1237654652565651637	129.497242	44.248864	0.14458	8.14	A	658	-613	99.2
1237654652565651551	129.520232	44.348909	0.14386	2.15	C	818	-802	96.8
1237654652565651712	129.446442	44.379164	0.14691	6.55	A	796	-5	95.9
rbs711_100_604	129.474092	44.395351	0.14496	0.669	C	991	-515	95.7
rbs711_154_921	129.364843	44.192634	0.14592	0.482	C	1032	-264	95.0
rbs711_170_421	129.266596	44.317944	0.14545	5.19	C	1062	-387	95.0
rbs711_172_401	129.262476	44.323036	0.14467	0.803	A	1099	-591	94.9
rbs711_140_550	129.357548	44.303642	0.14728	0.714	C	442	91	94.4
rbs711_121_315	129.340653	44.378765	0.14738	1.03	C	950	118	94.3
1237655108362108987	129.285682	44.320084	0.14751	6.03	A	942	151	94.3
1237654652565586095	129.344588	44.180009	0.14761	3.71	A	1194	177	93.4
1237654652565586098	129.366472	44.166001	0.14542	2.68	C	1262	-396	92.6
rbs711_121_1082	129.569020	44.242108	0.14424	1.46	C	1093	-703	92.6
rbs711_165_990	129.321227	44.164215	0.14478	1.15	A	1397	-562	92.1
1237654652565586126	129.430232	44.151193	0.14501	2.17	C	1343	-501	92.1
1237654652565586160	129.341944	44.282553	0.14802	2.03	C	552	285	88.2
rbs711_151_952	129.384227	44.188805	0.14800	1.15	A	1025	280	88.1
rbs711_203_553	129.183812	44.286568	0.14586	0.919	C	1595	-280	87.4
rbs711_122_1207	129.603338	44.217339	0.14451	0.691	A	1406	-633	81.5
1237655107825238285	129.602299	44.217301	0.14477	1.81	A	1400	-564	81.5
1237655108362109124	129.343638	44.390149	0.14844	2.53	C	1028	394	77.4
rbs711_97_567	129.463434	44.409596	0.14857	0.831	C	1097	429	73.2

*Table 7 continued*

Table 7 (continued)

Name	RA	Dec	$z_{\text{gal}}$	$L_{\text{gal}}$ ( $L^*$ )	Type	$\Delta\rho$ (kpc)	$\Delta v$ ( $\text{km s}^{-1}$ )	$f_{\text{mem}}$ (%)
(1)	(2)	(3)	(4)	(5)	(6)	(7)	(8)	(9)
rbs711_157_1246	129.386401	44.102791	0.14504	1.30	C	1810	−494	71.1
rbs711_152_1014	129.385972	44.170589	0.14877	1.09	A	1188	481	70.2
1237655107825303599	129.649314	44.232407	0.14367	3.64	E	1620	−851	69.2
1237654652565717293	129.560989	44.425002	0.14736	2.03	C	1517	112	69.2
rbs711_143_1352	129.499970	44.105369	0.14697	1.26	A	1842	10	68.9
rbs711_126_1339	129.614897	44.172196	0.14399	0.580	E	1719	−768	68.9
1237655108362174725	129.466743	44.459596	0.14737	1.98	A	1556	114	68.9
rbs711_109_1207	129.668913	44.289364	0.14334	0.459	C	1641	−938	67.4
rbs711_73_243	129.331584	44.461864	0.14702	0.580	E	1665	24	67.2
1237654652565651690	129.426343	44.374180	0.14927	2.69	A	734	612	63.3
1237654652565520483	129.338620	44.089159	0.14882	0.160	C	2001	493	61.2
rbs711_91_910	129.599690	44.429485	0.14513	0.529	C	1716	−471	61.1
rbs711_214_724	129.125490	44.251896	0.14891	0.783	A	2023	518	55.4
rbs711_152_955	129.377389	44.186016	0.14973	0.869	A	1062	732	55.3
rbs711_87_866	129.581308	44.454063	0.14640	1.13	C	1815	−139	54.7
rbs711_117_1407	129.693074	44.209873	0.14552	0.714	A	1970	−369	52.9
1237655108362174700	129.354902	44.492543	0.14700	1.93	C	1890	18	52.1

NOTE—Column 6 lists the galaxy’s spectral type: “E” for emission-line galaxies, “A” for absorption-line galaxies, and “C” for composite galaxies that show both emission and absorption.  $\Delta\rho$  and  $\Delta v$  are calculated with respect to the original SDSS group centers in Table 2;  $f_{\text{mem}}$  is the percentage of the Monte Carlo trials in which a galaxy was identified as a group member.

#### 4.4. Adopted Group Membership

The Monte Carlo analysis described in Section 4.3 allows us to assess which galaxies are group members probabilistically. Regardless of the uncertainties of this process it is essential that a final group membership is adopted so that its overall properties (mean recession velocity, mass, etc) and relationship to any absorption can be assessed, as well as whether the nearest galaxy to the QSO sight line is a group member (e.g., the passive galaxy closest to one of the absorbers in Group 32123 is not a member of the group identified in this field; [Stocke et al. 2017](#)).

As a first step, we determine each galaxy’s membership fraction,  $f_{\text{mem}}$ ; i.e., the fraction of the Monte Carlo trials in which a particular galaxy was identified as a group member. While it is tempting to define the final group as the set of all galaxies with  $f_{\text{mem}} > 50\%$ , there is no guarantee that this set of galaxies is self-consistent (i.e., all located within  $1.5R_{\text{grp}}$  of the group center and  $2\sigma_{\text{grp}}$  of the group redshift, to the exclusion of all other galaxies).

Instead, we calculate several group parameters (sky position,  $z_{\text{grp}}$ ,  $N_{\text{grp}}$ ,  $M_{\text{grp}}$ ) for each Monte Carlo realization, and compare them with the distribution of values over all realizations (i.e., marginal likelihoods<sup>5</sup>) to determine whether the value for a particular realization is a common outcome. This comparison uses an adaptive kernel density estimate ([Terrell & Scott 1992](#)) of the marginal likelihoods to avoid artifacts from arbitrary choices of histogram bin sizes and centers.

Each realization is then assigned a joint likelihood by multiplying the marginal likelihood values described above over all parameters. We adopt the membership of the realization with the highest joint likelihood as the final group configuration. This procedure ensures that we only adopt group configurations that are representative and self-consistent.

Figure 4 shows the adopted membership of individual groups, with group members displayed in color and the gradation in color indicating the recession velocity gradient for

<sup>5</sup> These are the histograms in Figure 15 (see Appendix B).

**Table 8.** Adopted Group Properties

Group	RA	Dec	$z_{\text{grp}}$	$N_{\text{grp}}$	$\log M_{\text{grp}}$	$R_{\text{grp}}$	$\sigma_{\text{grp}}$	$R_{\text{obs}}$	$\sigma_{\text{obs}}$	$\rho_*/R_{\text{grp}}$	$\Delta\rho$	$\Delta v$	$f_{\text{spiral}}$
	( $^{\circ}$ )	( $^{\circ}$ )				(kpc)	( $\text{km s}^{-1}$ )	(kpc)	( $\text{km s}^{-1}$ )		(kpc)	( $\text{km s}^{-1}$ )	(%)
(1)	(2)	(3)	(4)	(5)	(6)	(7)	(8)	(9)	(10)	(11)	(12)	(13)	(14)
12833	129.413	44.282	0.14589	50	14.45	1352	547	1396	444	1.32	137	-271	43.9
16803	234.995	-2.093	0.14839	55	14.49	1394	563	1297	455	0.59	507	1	49.1
19670	150.178	50.785	0.13370	48	14.30	1205	487	991	404	1.36	128	-193	50.0
25124	243.538	26.687	0.18569	29	14.40	1301	526	1167	448	1.22	704	-111	44.8
32123	203.047	45.432	0.15958	19	14.01	965	390	837	313	2.01	268	-34	50.0
36001	157.053	21.357	0.18761	6	13.80	821	332	729	170	0.36	638	-69	66.7
44564	208.170	36.280	0.14610	116	14.63	1553	628	1337	567	1.00	402	271	37.5
44565	208.170	36.280	0.14610	116	14.63	1553	628	1337	567	0.99	142	-823	37.5
44726	226.215	29.834	0.15236	7	13.53	667	270	178	223	1.98	527	74	40.0
44739	229.828	28.336	0.11887	59	14.30	1205	487	1135	336	2.00	604	128	68.0
44858	230.052	28.878	0.12707	99	14.59	1506	609	1546	569	1.49	364	-88	50.0
50433	157.732	30.845	0.13624	25	14.10	1034	418	600	338	1.73	187	67	31.3

NOTE— $M_{\text{grp}}$  has units of  $M_{\odot}$ , and is calculated assuming  $\Upsilon_{\text{grp}} = 2.5$ .  $\rho_*$  is the impact parameter between the adopted group center and the COS sight line.  $\Delta\rho$  and  $\Delta v$  are offsets from the SDSS group centroids in Table 2. The final column lists an estimate of the group’s spiral fraction derived from the spectral types of the adopted group members (see text for details).

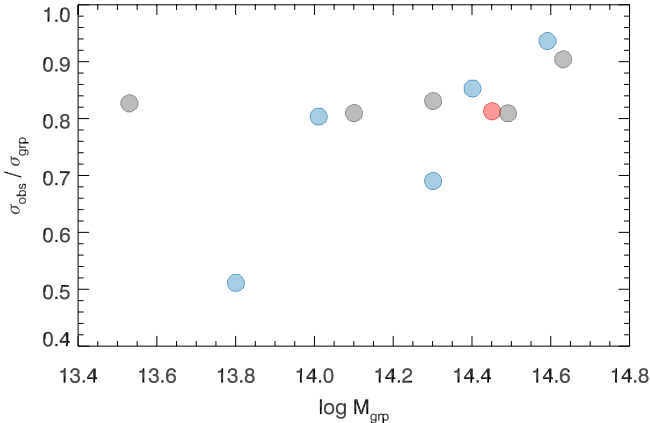
group members. Gray symbols are non-group galaxies in the field-of-view and velocity range. Zero velocity in the top histogram and the center in the bottom plot are the SDSS group velocity and sky position in Table 2, respectively. The solid vertical line in the top panel, and the “×” symbol in the bottom panel, mark the adopted group velocity and sky centroids, respectively. The star marks the AGN sight line location in the bottom panel, while the absorber velocity or velocities are shown as dashed vertical lines in the top panel.

Table 7 lists the adopted members of individual galaxy groups, with galaxies listed in order of decreasing membership fraction,  $f_{\text{mem}}$ . This table includes by column: (1) a galaxy identifier, which is either a SDSS “ObjID” or, for galaxies without SDSS redshifts, a string in the style of Keeney et al. (2018); (2 & 3) galaxy sky position in degrees; (4) galaxy redshift; (5) rest-frame  $g$ -band luminosity; (6) galaxy spectral type; (7 & 8) galaxy offset on the sky (in kpc) and in velocity (in  $\text{km s}^{-1}$ ) from the SDSS group centroids in Table 2; and (9)  $f_{\text{mem}}$ . A galaxy’s spectral type is determined visually as described in Keeney et al. (2018), and abbreviated “E” for emission-line galaxies, “A” for absorption-line galaxies, and “C” for composite galaxies that show both emission and absorption.

The properties of our adopted groups are summarized in Table 8, where all values are calculated using only galax-

ies that are adopted as group members by the procedure described above. The columns list largely the same information as those of Table 6, except for columns 12 and 13, which list the offsets between the adopted sky position and redshift and the SDSS values (Table 2), and column 14, which lists the group’s spiral fraction. We estimate a group’s spiral fraction using the spectral types of the members, where all emission-line and composite galaxies are considered “spirals”. These percentages use only those galaxies at  $L > 0.6L^*$  where the MMT0 galaxy survey work is largely complete (Keeney et al. 2018).

The centroids for 9 of the 12 groups did not vary significantly between the SDSS analysis and the results found here using much deeper data. The deeper MOS data find that groups 44564 and 44565 in the CSO 1022 sight line are part of a larger group with centroids intermediate between the two, and the new analysis finds group 12833 in the RBS 711 sight line to be  $1.5\sigma$  ( $\sim 300 \text{ km s}^{-1}$ ) lower in redshift than in Table 2. The remaining 9 groups showed little change in their 3D locations between Table 2 and Table 8. Derived halo masses range from  $10^{13.5}$  to  $10^{14.6} M_{\odot}$ , with a corresponding range of virial radii of  $R_{\text{grp}} = 650\text{--}1500$  kpc and velocity dispersions of  $\sigma_{\text{grp}} = 270\text{--}610 \text{ km s}^{-1}$  (see Table 8). The range of impact parameters in this study is  $0.36\text{--}2R_{\text{grp}}$ , with few sight lines  $< R_{\text{grp}}$  due to the criterion that these sight lines could



**Figure 5.** The calculated group mass ( $M_{\text{grp}}$ ) versus  $\sigma_{\text{obs}}/\sigma_{\text{grp}}$ , which is a measure of the virialization of these systems; e.g.,  $\sigma_{\text{obs}}/\sigma_{\text{grp}} = 1$  suggests a highly-virialized system. O VI-bearing groups are blue. All but two groups have  $\sigma_{\text{obs}}/\sigma_{\text{grp}} \gtrsim 0.8$ ; interestingly, the two less-virialized groups have rich associated UV absorption systems and high spiral fractions (see below).

not intercept an SDSS galaxy halo at  $< 1.5 R_{\text{vir}}$ , naturally excluding sight lines in the dense, inner regions of groups.

There is little difference between the total halo masses computed by Paper 3 using just the SDSS spectroscopic survey galaxies and the total halo masses computed using the deeper MMTO redshift survey (see Table 8). The revised values are only marginally lower (statistically less by 0.05 dex or 12%) than the SDSS values, much smaller than the factor 2-3 combined errors on individual mass estimates (see Table 2 and Table 6). Therefore, despite the modest number of group members in the SDSS analysis, the group halo masses derived by Paper 3 appear to be quite accurate and can be used as viable indicators of group mass for comparisons with other group properties, including those of the absorbers associated with groups at higher and lower estimated halo masses (see Section 4.5, 5.1 and 5.2).

#### 4.5. Basic Group Properties

In this section the basic properties of these groups are explored in order to place the UV absorptions into their proper context. While the number of group galaxies ( $N_{\text{grp}}$ ), the total group luminosity ( $L_{\text{grp}}$ ), total group mass ( $M_{\text{grp}}$ ), group virial radius ( $R_{\text{grp}}$ ), and velocity dispersion ( $\sigma_{\text{grp}}$ ) are all directly related by Equation 3-6, the observed velocity dispersion ( $\sigma_{\text{obs}}$ ) and the fraction of spiral or star-forming galaxies are independent of these derived group properties. The observed velocity dispersion differs from the calculated velocity dispersion ( $\sigma_{\text{grp}}$ ) because the group galaxies may not be in virial equilibrium.

In order to further explore the kinematic signature of virialization in these groups, Figure 5 shows the observed relationship between calculated group mass and the ratio between the

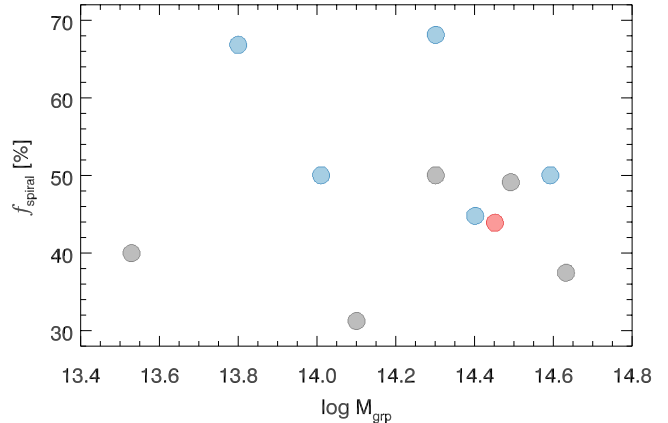


**Figure 6.** The calculated group mass ( $M_{\text{grp}}$ ) versus the fraction of  $L > 0.6L^*$  group galaxies that are star-forming ( $f_{\text{spiral}}$ ). For the star-forming/spiral classification we have used the spectroscopic proxy of emission lines; i.e., all galaxy spectra with either emission lines only or emission lines plus absorption lines are classified as spirals for this purpose (Keeney et al. 2018). O VI-bearing groups are blue.

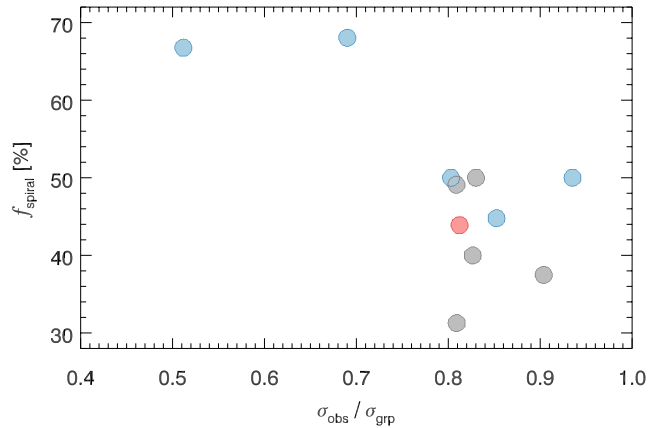


**Figure 7.** The virialization parameter ( $\sigma_{\text{obs}}/\sigma_{\text{grp}}$ ) versus the fraction of  $L > 0.6L^*$  group galaxies that are star-forming ( $f_{\text{spiral}}$ ). For the star-forming/spiral classification we have used the spectroscopic proxy of emission lines; i.e., all galaxy spectra with either emission lines only or emission lines plus absorption lines are classified as spirals for this purpose (Keeney et al. 2018). O VI-bearing groups are blue. In this plot the strong correlation between ETGs and virialization is apparent, although more examples of spiral-rich, unvirialized groups are required to make this conclusion robust.

observed and calculated velocity dispersion,  $\sigma_{\text{obs}}/\sigma_{\text{grp}}$ . At  $M_{\text{grp}} > 10^{14} M_{\odot}$ , all but one of these groups have  $\sigma_{\text{obs}}/\sigma_{\text{grp}} \geq 0.8$ , suggesting that these massive groups are mostly virialized. The sample also includes a couple of groups (36001 and 44739) which are not close to being virialized by this same measure. These two groups are among the few in this sample with very rich absorption systems (e.g., group 44739 has 4 absorbers; one H I-only; one H I + Si III; and two H I

+ O VI; see Section 5.2). Thus, this small sample appears to bridge the halo mass region where groups are becoming fully virialized in the current epoch.

Figure 6 and 7, show the spiral (i.e., star-forming) fraction of galaxies in these groups as a function of halo mass and of virialization, respectively. Because we do not possess good morphological information about these group galaxies, we have used the spectral classification of Keeney et al. (2018) as a proxy; viz., emission-line and composite (emission-line plus absorption-line) galaxies are classified as star-forming/spirals for this purpose. The spiral fraction is computed using all group members with  $L > 0.6L^*$ . The MMT0 MOS group galaxy survey used for these classifications (Keeney et al. 2018) is  $> 90\%$  complete to this limit out to  $\rho_* \leq 1$  Mpc for all groups except 25124, which is complete only to a limit slightly deeper than the SDSS ( $\sim 3L^*$  out to  $\rho_* \leq 1$  Mpc). If group 25124, which is a massive ( $10^{14.6} M_\odot$ ), highly-virialized ( $\sigma_{\text{obs}}/\sigma_{\text{grp}} = 0.8$ ) group with  $f_{\text{spiral}} = 0.45$ , were excluded from this discussion it would not alter these plots noticeably.

It is clear from Figure 5 and 6 that the mass range of this survey spans a range of group properties from nearly fully-virialized massive groups with large fractions of early-type galaxies (ETGs) to partially-virialized groups with large spiral fractions. Figure 7 highlights that the spiral fraction and partial virialization go together, although this conclusion certainly requires a much larger group sample, particularly at lower halo mass and lesser virialization, to be robust. Nevertheless, in the most massive, highly-virialized groups the spiral fraction is  $< 50\%$ , so these groups are dominated by ETGs.

Among the nine groups with high virialization factors, the three groups with the lowest spiral fraction have no detected UV absorption lines. These groups are neither highly centrally-concentrated nor dominated by a single ETG like the massive X-ray-detected groups of Mulchaey et al. (1996), but may have similar gas properties. Deep X-ray continuum observations are appropriate to test whether a hot IGrM is present in the ETG-dominated groups in this sample.

And while the least-massive groups in the sample are highly spiral-dominated and not always highly-virialized, they are still an order of magnitude more massive than the small, spiral-dominated groups like the Local Group where most of the star-formation in the current Universe takes place. New UV spectroscopy of spiral-rich groups at  $M_{\text{grp}} \leq 10^{13.5} M_\odot$  is required to investigate typical star-forming sites in the local Universe.

## 5. DISCUSSION OF RESULTS

### 5.1. Covering Fraction

Despite the wide range of impact parameters targeted, HI absorption was detected toward 7 of the 12 groups probed

through the full range of impact parameters (group 25124 is counted as a non-detection because its single absorber system is at least partly associated with an individual galaxy; see Table 5). Table 10 (see Appendix A) lists all absorbers within  $\pm 2.5\sigma_0$  (typically,  $\pm 1000$ - $1500$  km s $^{-1}$ ) of the group velocity centroid using the initial SDSS analysis (Table 2), but for the important choice of the absorber velocity range for group association, we adopt a range corresponding to  $\pm 2.5\sigma_{\text{grp}}$ , based on the adopted group parameters listed in Table 8.

While this choice is somewhat arbitrary, it is a good match to the criterion we used for including galaxies as group members; i.e., based on mock catalogs produced from  $N$ -body simulations,  $> 99\%$  of all satellite halos are found within  $\pm 2\sigma_{\text{grp}}$  of the primary halo's velocity (see Section 4.3). Increasing this range from  $\pm 2\sigma_{\text{grp}}$  to  $\pm 2.5\sigma_{\text{grp}}$  provides a small allowance for both the statistical sampling of the potential well using the modest number of galaxies available (i.e., uncertainties in mean velocity and velocity dispersion), and also for the peculiar velocity of gas which may have been expelled from, or is falling into, any individual galaxy in the group.

Enforcing these velocity bounds removes only one absorber system in Table 10 from group association: 36001/0.18429 at  $-906$  km s $^{-1}$  (a velocity difference of  $2.8\sigma_{\text{grp}}$ ). While there are other absorbers that remain in the sample at larger velocity differences, this particular absorber is excluded because group 36001 has the smallest  $\sigma_{\text{grp}}$  in the sample; however, there are two other absorber systems associated with group 36001, so it is retained as a group detection. Decreasing this limit to  $2\sigma_{\text{grp}}$  eliminates only an additional 2 systems of the 18 total. There are no viable individual galaxy associations associated with any of the systems with large  $|\Delta v|$  (see Figure 1 and Table 5).

While there are 10 sight lines through 12 galaxy groups as defined by our original set of observations, two modifications are required to correctly assess the covering fraction. First, our deeper MOS and subsequent analysis finds evidence that groups 44564 and 44565 in the CSO 1022 sight line are, in fact, one considerably more massive group; this leaves 11 groups probed. Second, the single absorber system in group 25124 was determined to be associated with a single bright galaxy, not the group as a whole; however, a BLA present within the Ly $\alpha$  absorption profile (see Section 3.1) is similar to other galaxy group absorptions investigated by Paper 2. Due to this uncertainty, we eliminate group 25124 from the covering fraction discussion rather than count it as a non-detection, leaving ten groups only.

The resulting Ly $\alpha$  covering fraction of the 10 groups of galaxies is shown in Table 9 as a function of normalized impact parameter,  $\rho_*/R_{\text{grp}}$ . Despite the small number statistics, Table 9 shows that the covering fraction is substantial ( $\gtrsim 50\%$ ) out to at least  $2R_{\text{grp}}$  ( $\sim 2$  Mpc, given the masses of the groups probed). This result is consistent with the

**Table 9.** Covering Fraction of Group Absorption

$\rho_*/R_{\text{grp}}$	Cov. Frac.	Notes
0.0-0.5	1/1	All have O VI
0.5-1.0	1/2	Metal-free
1.0-1.5	2/2	One metal-free, one low-ions only
1.5-2.0	3/5	All have O VI

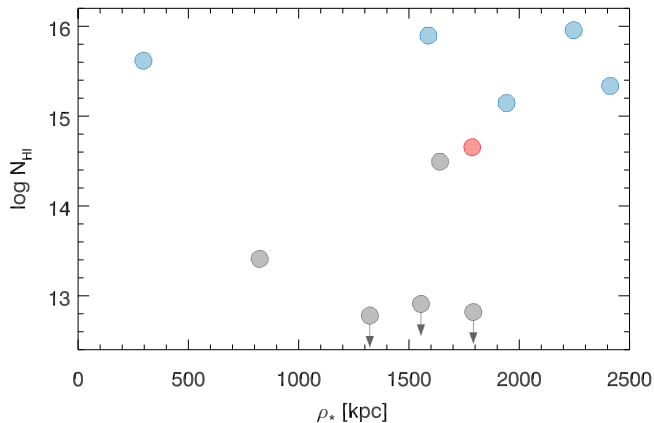


**Figure 8.** The total  $N_{\text{HI}}$  in all absorption components associated with the group as a function of the physical impact parameter  $\rho_*$ . O VI-bearing groups are blue. The H I column densities do not show any obvious trend with the group-centric impact parameter out to 2 Mpc, or  $\sim 2R_{\text{grp}}$ .

rather constant distribution of covering fractions with radius ( $\sim 50\%$  out to several virial radii, or  $\sim 1$  Mpc) seen for absorption-line galaxies in Keeney et al. (2018). It appears that the CGM of absorption-line galaxies joins seamlessly with group gas to which those galaxies typically belong.

Similarly, in Figure 8 the total H I column density within  $2.5\sigma_{\text{grp}}$  of  $z_{\text{grp}}$  along these group sight lines is shown as a function of sight-line impact parameter from the group centroid on the sky. The obvious conclusion from this plot is that cool and/or warm gas remains abundant out to at least 2 Mpc (or  $\sim 2R_{\text{grp}}$ ) for these groups. While the high, but  $< 100\%$ , covering fraction found here may be due to a patchy distribution of UV-absorbing gas in all these groups, it is also possible that the presence or absence of this gas can be due to other factors.

In Paper 2, an argument was presented that the area covered by warm group gas is large,  $\sim 1$  Mpc in radius per group if unity covering factor is assumed. This estimate is based on the number density per unit redshift ( $dN/dz = 4$ ) of warm absorbers ( $T \geq 10^5$  K) seen at low- $z$  and the space density of groups of galaxies ( $\approx 3 \times 10^{-4}$  Mpc $^{-3}$ ; Paper 3). The  $\gtrsim 50\%$

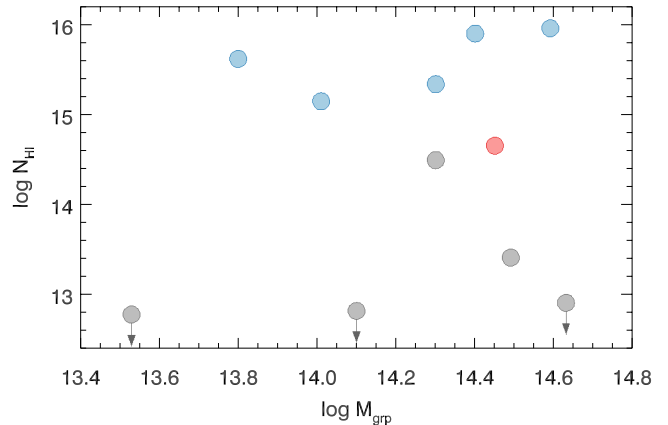


**Figure 9.** O VI-bearing groups are blue. Despite including both virialized and unvirialized groups, there is no obvious trend between the presence of absorbers and total group halo mass in this sample. Neither the H I detections/non-detections nor the H I column densities show any obvious trend with the estimated mass of the group.

covering fraction out to  $\rho \geq 2$  Mpc found by this study supports the previous conclusion that a large gaseous medium exists in galaxy groups.

However, the huge area covered by H I absorption does not require a huge mass because the filling factor of this gas is unknown and could be small; e.g., if the cool gas is in small clouds like in the CGM and the warm gas is in filamentary structures scattered throughout the volume of the group, the filling factor of cool plus warm group gas could be similar to the filling factor (3-5%) of cool gas in the CGM, or even smaller. In this case, the UV-detected group gas can have a total gas mass *per galaxy* of only 2-4% of the full baryon budget. This makes it unlikely that the UV-detected group gas solves the baryon problem. But, when viewed as transition gas, the UV absorbing gas may be cospatial with even hotter gas that constitutes a volume-filling IGrM. Further, in this sample there is no strong evidence for warm or warm-hot gas found associated with these groups (see Section 3.2).

Figure 9 shows the total H I column density of all absorption components in these groups as a function of group mass. Despite their lower mass, the two relatively un-virialized groups, 36001 ( $\log M_{\text{grp}} = 13.80$ ) and 44739 ( $\log M_{\text{grp}} = 14.30$ ) both have H I-rich absorption systems. There is no obvious trend between group mass and either detections/non-detections or the total  $N_{\text{HI}}$  in this mass range.

However, it is notable that the three groups that lack H I absorption (Table 10 in Appendix A) are the three most ETG-rich groups (Table 8), and among the most highly virialized (Figure 7). While a larger sample is certainly needed, this result suggests that groups which are spiral-rich and not completely virialized will be detected strongly and multiply in H I and metals. This result predicts that less-virialized groups at

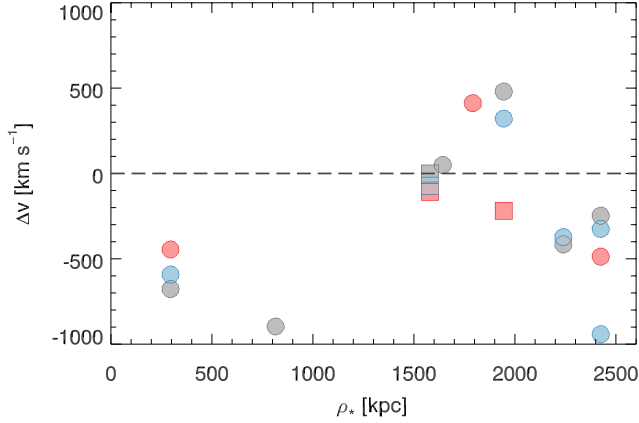


**Figure 10.** The physical impact parameter in kpc is plotted against the (absorber-group) velocity difference in  $\text{km s}^{-1}$ . Colors are as in Figure 9, and squares are absorbers which could be associated with individual galaxies.

lower halo mass will be found to have large reservoirs of cool plus warm UV-detectable gas which is not obviously associated with a specific group galaxy.

### 5.2. Absorber Kinematics

Limited by our available measurement tools, the kinematic information we have for these absorbers consists of: (1) a two-dimensional location on the sky with respect to the sky centroid of the group, and (2) the radial component of the velocity relative to the group centroid velocity. In Figure 10, these basic quantities are displayed in a plot of impact parameter,  $\rho_*$ , versus the one dimensional velocity difference,  $\Delta v = c(z_{\text{abs}} - z_{\text{grp}})/(1 + z_{\text{grp}})$ . There is no strong concentration around  $\Delta v = 0$ , which would be expected if the detected gas is a massive IGrM as seen in X-ray bremsstrahlung emission for more massive systems (Mulchaey 2000). The relative dearth of absorbers at  $\rho_* \leq 1.5$  Mpc is due to our imposed criterion that no sight line pass within  $1.5 R_{\text{vir}}$  of an SDSS group galaxy, thus avoiding the dense central regions of groups.

There is no obvious kinematic difference between the metal-bearing absorbers (red symbols for only low ions present and blue symbols for O VI present) and the metal-free absorbers (gray symbols); nor is there any difference between the locations of the high and low ions. The square symbols show the location of the absorbers possibly associated with individual bright galaxies in groups 25124 and 32123. If any or all of those absorbers are associated with the entire group rather than individual galaxies, the basic results of this plot are not altered.

More revealing is Figure 11, which shows these same observables normalized by the theoretical quantities of group virial radius (i.e.,  $\rho_*/R_{\text{grp}}$ ) on the horizontal axis and escape velocity (i.e.,  $|\Delta v|/v_{\text{esc}}$ ) on the vertical axis, where the escape velocity is calculated at a radius equal to the observed

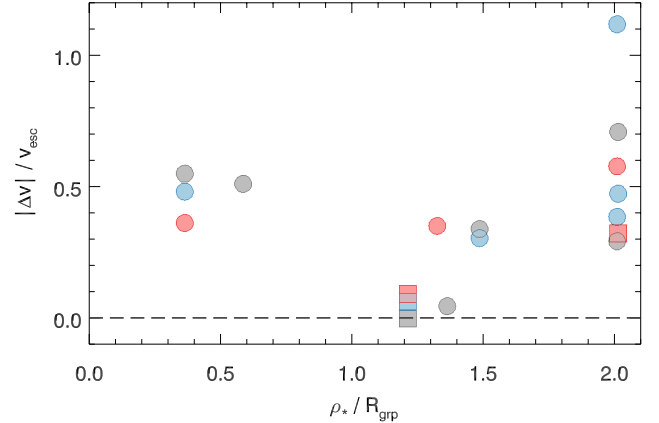


**Figure 11.** Symbols are similar to their depictions in Figure 10, but in this case the impact parameter ( $\rho_*$ ) is displayed in units of the group virial radius ( $R_{\text{grp}}$ ), while the velocity difference is in units of the escape velocity ( $v_{\text{esc}}$ ) at the radius of the impact parameter.

impact parameter. What is striking in this plot is that only one of the absorbers has sufficient radial velocity to escape the group gravitational potential well.

This result is similar to the results found the COS-Halos study (Tumlinson et al. 2011) of the inner half of the CGM for which absorbers do not possess sufficient radial velocity to escape their home galaxy’s gravitational potential. While Stocke et al. (2013) and Keeney et al. (2017) found a similar result to COS-Halos in the inner CGM, when the outer CGM ( $\rho > 0.5 R_{\text{vir}}$ ) is probed the results are quite different. At  $\rho > 0.5 R_{\text{vir}}$ , the one-dimensional velocity difference between absorbers and their associated galaxies cluster around the value for the escape velocity (see Figure 8 in Stocke et al. 2013 and Figure 13 in Keeney et al. 2017). For individual galaxies, this suggests that many of these CGM absorbers will escape if their direction of motion is out-going, although some few still are unlikely to escape (see e.g., Tumlinson et al. 1999; Keeney et al. 2005; Stocke et al. 2010; Tumlinson et al. 2011; Stocke et al. 2013). Presumably the absorbers discovered in this small survey are examples of gas which has escaped its home galaxy CGM and is now bound to its home galaxy group.

This result does not appear to be caused by the limit placed on absorber velocity, by which absorbers are excluded for association if  $|\Delta v| > 2.5 \sigma_{\text{grp}}$  from the group mean velocity. The one absorber excluded by this velocity cut (36001/0.18429) has a radial velocity relative to this group of only  $0.7 v_{\text{esc}}$ . On the other hand, the absorber whose relative velocity exceeds the escape speed (44739/0.11537, a mixed H I, O VI, and Si III absorber) has a relative velocity of  $< 2 \sigma_{\text{grp}}$  from the mean group velocity and so would have been included even if the limit were lowered.

To ensure that any fast-moving absorber that could have escaped from these groups has not been excluded from consid-

eration by the assumed cutoff in velocity that was imposed, a search for such absorbers was conducted around all the sight lines in this survey. Increasing the relative velocity bounds to include all absorbers at  $|\Delta v| \leq 5 \sigma_{\text{grp}}$  (roughly  $\pm 2500 \text{ km s}^{-1}$ ) from the group redshift, an additional dozen absorbers were found; however, all but three of these are metal-free and not relevant to these concerns. Of the remaining three, two show absorption in H I and O VI, and are located only  $0.83 R_{\text{vir}}$  from the same  $0.5 L^*$  galaxy, an individual galaxy association by our earlier discussion. The third absorber is  $2.3 R_{\text{vir}}$  from a  $2 L^*$  galaxy near group 19670, so this absorber could be associated with a lower luminosity galaxy not observed in our program, or it could be associated with another group of galaxies to which this nearest galaxy is a member, or it has been ejected from group 19670 at  $\sim 1800 \text{ km s}^{-1}$ , or  $1.5 v_{\text{esc}}$ . Even if the latter is correct, only 2 of 13 metal-bearing absorbers in these groups could have relative radial velocities exceeding the escape velocity for the groups they probe, thus any group mass lost by this process to the IGM is small.

Reinforcing the results shown in Figure 10 and 11 is Figure 12, which shows that there is little trend between the normalized absorber-group velocity difference and the group mass. Except for the one absorber mentioned above which exceeds the escape speed in radial velocity difference, there is little evidence that these absorption systems will escape from their parent groups.

For galaxy groups, Figure 11 shows that most absorbers may **not escape** from the group potential unless their direction of motion is mostly tangential on the sky or inward. This result can have significant implications for galaxy evolution; e.g., these groups are close to being “closed boxes” for galactic evolution in the current epoch. While some gas can be accreted onto the group from the intergalactic medium, any metals currently produced by group galaxies may not leave the group. Any baryons and metals which left the region of this group must have done so at much earlier cosmic times.

The BAHAMAS cosmological hydrodynamic simulations (McCarthy et al. 2017), which have been tuned to observational X-ray and Sunyaev-Zeldovich Effect constraints for groups and clusters, predict that about 1/3 of the baryons associated with a  $10^{13.8} M_{\odot}$  halo mass are ejected beyond the virial radius, while a  $10^{14.6} M_{\odot}$  halo should retain almost all of its baryons and be considered essentially baryonically closed. Almost all of the groups here are at estimated halo masses in excess of  $10^{14} M_{\odot}$ , in the regime where the BAHAMAS simulations suggest that most of the baryons should be retained by the group suggesting that a hot, massive IGrM is present in these groups.

### 5.3. Gas versus Group Properties

In our initial study of gas in galaxy groups (Paper 2) we used previously detected H I plus O VI absorbers from Pa-

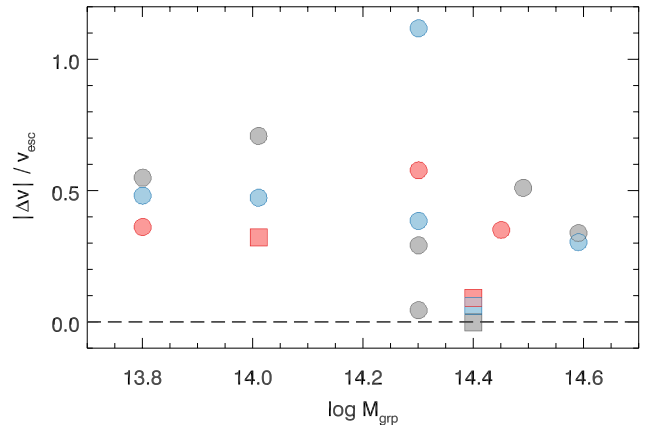


**Figure 12.** A plot of the calculated group mass ( $M_{\text{grp}}$ ) versus the absorber-group radial velocity difference, where the velocity difference is in units of the escape velocity ( $v_{\text{esc}}$ ) at the radius of the impact parameter.

per 1 as markers to search for groups at the absorber redshift. Groups of varying richness (total group luminosities ranging from a few  $L^*$  to nearly  $100 L^*$ ) were found near these absorbers. In that study, weak correlations were seen between gas and group properties, which supported the identification of those absorbers with the groups distinct from gas associated with individual galaxies in the groups.

Herein, the selection criteria excluded sight lines near ( $\rho \leq 1.5 R_{\text{vir}}$ ) bright galaxies in these groups, strongly supporting a group association for these absorbers. Still, many (9) absorbers were found within these groups with low ions like Si III typical of cool, photo-ionized CGM absorbers. Only two of these apparently photo-ionized absorbers are at  $\rho < 1.5 R_{\text{vir}}$  from the nearest galaxy; seven others are at larger distances including three at  $\rho > 3 R_{\text{vir}}$  away.

While it is possible that there are sub- $L^*$  galaxies closer to some of these absorbers that were not observed by our galaxy survey (Keeney et al. 2018), more likely these metal-bearing clouds have escaped their home galaxy’s potential well and are now bound within the confines of their home galaxy group. The cool clouds in these groups that are well-away from galaxies could be CGM clouds that have escaped their home galaxy as predicted by Stocke et al. (2013) and Keeney et al. (2017) based on CGM cloud kinematics.

Two plots from Paper 2 suggested weak correlations between absorber temperature and total group luminosity (Figure 13) and between absorber temperature and group velocity dispersion (Figure 14). These are reproduced here with the addition of a few points from this study selected in the same way; i.e., O VI absorbers in groups with either warm or cool absorbers depending on H I, O VI, and Si III properties (see Section 3.2). These Figures show that any correlation between these quantities is very weak or nonexistent. In these two figures, five points from the current study are added at

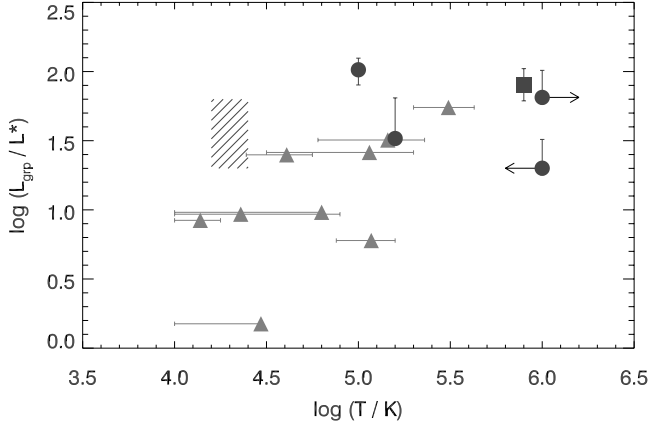


**Figure 13.** Group absorber temperatures versus total group luminosity, reproduced from Figure 10 of Paper 2. The gray points are from Paper 2, while the black points are warm absorbers from this study. The current sample temperatures are all quite uncertain and should be viewed as estimates. The hashed area is the approximate location for four photo-ionized group absorbers from this study. With the addition of the new data there is no obvious correlation found between these parameters.

$T > 10^5$  K (group 32123 has two possible warm absorbers; the one with a measured value is plotted, not the upper limit). The cross-hatched region shows the range of cool absorber properties where  $T \approx 20,000$  K is assumed.

While the groups studied here are comparable to only the most luminous and massive groups found by Paper 2, these groups possess gas at the full range of temperatures from 20,000 K to  $> 10^6$  K, diminishing the already marginal correlations found by the earlier work. Further, the absence of correlations in Figure 13 and Figure 14 show that the gas temperature is not directly related to the mass of the group (i.e., its potential well depth). Nor are the absorbers detected at velocities close to the group centroid velocities. These are other indicators that the UV-detected gas is not volume filling but is, instead, that gas most easily detectable through UV absorption.

Since the possibly warm clouds have temperatures too hot to be photo-ionized by the UV background, either these absorbers are heated by interaction with a hotter medium or are condensing out of it. In either case, a hot intra-group medium is suggested to be present that could be connected more intimately to the gravitational potential well depth. In richer systems like clusters and elliptical-dominated groups, this hotter gas is detected in X-ray bremsstrahlung emission.

Based on extrapolations from the richer systems shown in Figure 14, the groups studied here are expected to have an intra-group medium temperature of  $\log(T/K) = 6-7$ , much hotter than the warm clouds we detect as BLAs and broad O VI absorbers. The solid line extrapolation assumes energy equipartition between gas and galaxies (i.e.,  $\beta_{\text{spec}} = 1$ ; Os-

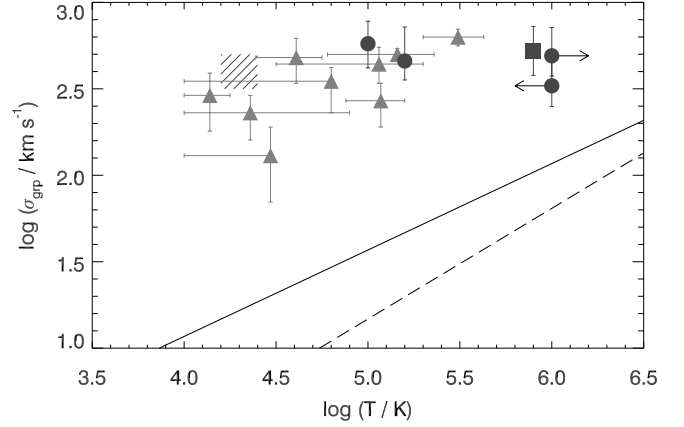


**Figure 14.** Group absorber temperatures vs. group velocity dispersion, reproduced from Figure 11 of Paper 2. The gray points are from Paper 2, while the black points are warm absorbers from this study. The current sample temperatures are all quite uncertain and should be viewed as estimates. The hashed area is the approximate location for four photo-ionized group absorbers from this study. With the addition of the new data there is no obvious correlation found between these parameters. The solid line is the extrapolation of  $\beta_{\text{spec}} = 1$  (energy equipartition between galaxies and gas) from the clusters and groups data found in Osmond & Ponman (2004); see their Figure 16. The dashed line is an extrapolation of the best-fit power law for clusters and groups from Wu et al. (1999). Notice that the points and limits for the warm absorbers in groups are far above either of these extrapolations from richer galaxy systems, illustrating that this gas is too cool by one order of magnitude or more from the expected volume-filling intra-group gas conditions.

mond & Ponman 2004), while the dashed line is the best-fit power-law extrapolation based on the Wu et al. (1999) compilation of clusters and groups. Our data points in Figure 14 are clearly too cool to fall near these extrapolations, nor do the current data possess the slope appropriate for an intra-group medium based on these extrapolations.

## 6. SUMMARY AND CONCLUSIONS

This study uses UV absorption lines detected in COS/G130M spectra of 10 AGN targets that probe 12 galaxy groups selected from a homogeneous catalog culled from the SDSS spectroscopic survey in the range  $z_0 = 0.10-0.19$ , which facilitates the detection of both the O VI doublet and Ly $\alpha$  in the single G130M exposures allocated. These sight lines occur at group-centered impact parameters ranging from 0.3-2 group virial radii with absorber-group radial velocity differences as large as  $\pm 1000$  km s $^{-1}$ .

In order to ensure that these spectra probe gas associated with the foreground groups distinct from individual galaxies within the groups, an important sample selection criterion is that no sight line passes within 1.5 virial radii of a bright SDSS group galaxy. Earlier work (Keeney et al. 2017) showed that an association between an absorber and a single

galaxy is plausible only if the impact parameter  $\rho \leq 1.4R_{\text{vir}}$ . But this selection criterion also has the effect of minimizing the number of sight lines close to group centers where the galaxy density is highest, minimizing sample statistics close to group centers.

Excepting for SDSS J1540–0205 (where a Lyman limit system at  $z = 0.33$  obscures the O VI region in group 16803), S/N = 15–30 was achieved for these targets in the wavelength regions of Ly $\alpha$  and the O VI doublet at the group redshift. Absorption associated with these groups was detected for 7 of the 12 groups probed, including group 16803 where only Ly $\alpha$  was detected. Metal lines, usually the O VI doublet and/or Si III 1206 Å, are seen in 12 of the 18 absorber components detected. See Figure 1 for the COS spectra; all line parameters are listed in Table 10.

These *HST*/COS observations were supported by a deep and wide galaxy redshift survey around each of these sight lines (see Keeney et al. 2018 for details of these observations and subsequent spectral analysis). While the SDSS spectroscopic survey provides complete galaxy redshift information down to  $L \gtrsim L^*$ , the MOS obtained by Keeney et al. (2018) extends to  $L > 0.2L^*$  at a completeness level over a 20'-radius field-of-view of  $\gtrsim 60\%$ .

These MOS observations were designed to obtain  $\geq 20$  group members so that each group could be correctly characterized from the galaxy data. This observing goal was accomplished in all but three cases (groups 36001, 49980 and 44726), which have few member galaxies in toto, not because they were poorly observed. The galaxy positions and redshifts provide ample data to characterize these groups using a unique Monte-Carlo approach that is described in detail in Section 4. All MOS galaxy redshifts used in this study can be found at MAST via [doi:10.17909/T9XH52]<sup>6</sup>.

The resulting group parameters from the Monte Carlo process are listed in Table 6 and Table 8, and are generally very similar to the parameters found by the algorithm of Paper 3 using the SDSS data alone Table 2. These groups have varying richness with total luminosities  $L = 10\text{--}130L^*$ , virial radii of  $R_{\text{grp}} = 680\text{--}1540$  Mpc, velocity dispersions of  $\sigma_{\text{grp}} = 270\text{--}630$  km s<sup>-1</sup>, and estimated halo masses of  $\log(M_{\text{grp}}/M_{\odot}) = 13.5\text{--}14.5$ . At these masses, the groups in this sample have a mixture of early- and late-type galaxies and are more massive than most nearby groups in the Local Supercluster, including the Local Group. Additionally, this sample spans the range from almost fully virialized groups dominated by early-type, passive galaxies to partially-virialized, spiral rich groups. These groups are similar to the groups in which Paper 2 found warm absorbers.

Based on the information derived from these two datasets, the basic results from this study include:

1. The covering fraction of Ly $\alpha$  absorption due to these groups is  $\gtrsim 50\%$  at impact parameters  $\rho = 0.4\text{--}2R_{\text{grp}}$ ;  $R_{\text{grp}} \approx 1$  Mpc for the masses of these groups. Additionally, there is no obvious trend between the observed  $N_{\text{HI}}$  and impact parameter out to  $\approx 2$  Mpc. This is quite different from the rapidly declining CGM  $N_{\text{HI}}$  around individual star-forming galaxies. While large covering fractions over such a huge area around these groups is consistent with the number density of warm absorbers ( $dN/dz = 4$  per unit redshift; Paper 2), high covering fractions do not lead necessarily to large volume-filling factors and very large masses of cool and/or warm gas (see below). Given the unstable condition of warm, collisionally-ionized gas, it is likely that this gas exists in filaments that fill only a few percent of the group's volume and account for only a few percent of the total baryon budget of the group.
2. While the H I covering fraction of these groups is high over a very large surface area, it is possible that some few massive groups always possess detectable warm and/or cool H I absorption and some do not. In this sample, the three H I non-detections are all quite massive, highly-virialized groups with spiral galaxy fractions of  $\sim 40\%$  (see discussion in Section 5.1). This result leads to the prediction that lower mass (approximately one order of magnitude less massive than those studied here), spiral-rich groups will have H I Ly $\alpha$  detections at close to 100% covering fraction out to a couple of virial radii in impact parameter. Since these lower halo mass groups, which are similar to the Local Group in mass and kinematics, are the sites where most of the current-epoch star formation occurs, probing these groups for UV absorption is vital to understand the full context of star formation in the local Universe.
3. Different from the circumstance for single-galaxy CGMs, the absorbers associated with groups do **not** possess sufficient relative radial velocities to escape from these groups; i.e.,  $|\Delta v|/v_{\text{esc}} \leq 0.6$  except for one absorber with  $|\Delta v| = 1.1 v_{\text{esc}}$  (see Section 5.2). Since seven H I and low-metal-ion (usually Si III) absorbers are found in these groups well away from individual galaxies, cool CGM clouds do escape from their home galaxy (as suggested by CGM cloud radial velocities close to  $v_{\text{esc}}$ ; see Stocke et al. 2013; Keeney et al. 2017) but do not escape from their home galaxy group. This has the important consequence for massive galaxy groups in the mass range studied here that little or no gas escapes from galaxy groups into the

<sup>6</sup> <https://archive.stsci.edu/prepds/igm-gal/>

IGM in the current epoch. If baryons and metals have left the region of this group, that process must have occurred at earlier cosmic times.

4. There are several observational results from this study which strongly suggest that the cool and/or warm gas detected in groups is neither volume filling nor massive. These observational results include: (1) the cool or warm gas detected is not close to either the sky centroid of these groups nor to their radial velocity centroid (see Figure 10); (2) the temperature of this gas does not correlate with two different measurements of group halo mass, its total luminosity (see Figure 13) and the velocity dispersion of its galaxies (see Figure 14); and (3) the warm gas temperatures, both those possible detections found herein and those found in Stocke et al. (2014), are too cool by an order of magnitude to be a volume-filling IGrM based on extrapolations from richer galaxy systems (see Figure 14).

While plentiful warm and cool gas has been found associated with rich groups of galaxies, a massive IGrM that completes the baryon inventory in star-forming and passive galaxies has yet to be discovered. Given its predicted temperature range of  $10^6$  to  $10^7$  K, new soft X-ray instrumentation and telescopes will be required to discover it. Based on assuming pressure balance with individual CGM clouds at  $P/k \approx 10 \text{ cm}^{-3} \text{ K}$ , an IGrM at these temperatures has physical densities of  $n = 10^{-5}$  to  $10^{-6} \text{ cm}^{-3}$ , making its detection challenging (although see Nicastro et al. 2018, and M. Donahue et al. 2019, in prep, for tentative detections).

With little evidence for gas escaping from these groups, systems with total halo masses of  $10^{13.5}$  to  $10^{14.5} M_{\odot}$  should be considered “closed boxes” in the current epoch for galactic evolution and the baryon census. Since the currently detected baryons are insufficient to bring these groups up to

the cosmic ratio of baryons to dark matter, a massive IGrM is likely present. Indeed, the recent BAHAMAS numerical simulations predict that most of the groups studied here, specifically the most massive ones, have retained most of their baryons. If this is the case, a massive IGrM should be present in these groups to close the baryon accounting. Efforts should be made to extend these UV results downward in halo mass to systems the size of the Local Group to determine if these smaller groups show similar trends; e.g., presence of both cool and warm gas and few absorbers escaping. These lower mass groups are important because they are the sites where most of the star formation in the current Universe is taking place. Since different galaxy groups can have differing evolutionary and thus metallicity histories (e.g., only some have had major mergers early-on), the galaxy metallicity pattern in groups can vary. This may be observable as differences in the mass-metallicity relationship in different groups, contributing to the width observable in that relationship when galaxies from many groups are included (factor of  $\sim 4$  [95% contour] in metallicity at fixed mass; Tremonti et al. 2004).

This study also clarifies that theoretically modeling the CGM of star-forming and passive galaxies must account for the IGrM of the groups in which the absorbers and galaxies are found. Specifically this means that the halo masses investigated in numerical simulations must concentrate on group-size halos ( $10^{12.5}$  to  $10^{14.5} M_{\odot}$ ) to both fully account for the all the baryons in these systems and to predict CGM and IGrM properties successfully.

This research was supported by NASA/HST grants 14277 (PI: JTS) and 14308 (PI: BDO). Special thanks to Alex Parker for stimulating discussions. Access to the MMTO through the University of Arizona is gratefully acknowledged.

## REFERENCES

- Adelberger, K. L., Shapley, A. E., Steidel, C. C., et al. 2005, *ApJ*, 629, 636
- Adhikari, S., Dalal, N., & Chamberlain, R. T. 2014, *JCAP*, 11, 19
- Beers, T. C., Flynn, K., & Gebhardt, K. 1990, *AJ*, 100, 32
- Berlind, A., Frieman, J., Weinberg, D. H., et al. 2006, *ApJS*, 167, 1 (Paper 3)
- Binney, J., & Tremaine, S. 1987, *Galactic Dynamics*, Princeton, NJ: Princeton University Press
- Bordoloi, R., Tumlinson, J., Werk, J. K., et al. 2014, *ApJ*, 796, 136
- Borthakur, S., Heckman, T., Strickland, D., Wild, V., & Schiminovich, D. 2013, *ApJ*, 768, 18
- Burchett, J. N., Tripp, T. M., Bordoloi, R., et al. 2016, *ApJ*, 832, 124
- Cen, R. & Ostriker, J. P. 1999, *ApJ*, 514, 1
- Chen, H.-W., Lanzetta, K. M., Webb, J. K., & Barcons, X. 2001, *ApJ*, 559, 654
- Chilingarian, I. V., Melchior, A.-L., & Zolotukhin, I. Y. 2010, *MNRAS*, 405, 1409
- Chilingarian, I. V. & Zolotukhin, I. Y. 2012, *MNRAS*, 419, 1727
- Danforth, C. W., & Shull, J. M. 2008, *ApJ*, 679, 194-219
- Danforth, C. W., Keeney, B. A., Tilton, E. M., et al. 2016, *ApJ*, 817, 111
- Davé, R., Hernquist, L., Katz, N., & Weinberg, D. H. 1999, *ApJ*, 511, 521
- Diemer, B. & Kravtsov, A. V. 2014, *ApJ*, 789, 1
- Diemer, B. 2017, *ApJS*, 231, 5

- Fabricant, D., Fata, R., Roll, J., et al. 2005, *PASP*, 117, 1411
- Hinshaw, G., Larson, D., Komatsu, E., et al. 2013, *ApJS*, 208, 19
- Johnson, S. D., Chen, H.-W., & Mulchaey, J. S. 2015, *MNRAS*, 449, 3263
- Keeney, B. A., Momjian, E., Stocke, J. T., Carilli, C. L., & Tumlinson, J. 2005, *ApJ*, 622, 267
- Keeney, B. A., Danforth, C. W., Stocke, J. T., France, K., & Green, J. C. 2012, *PASP*, 124, 830
- Keeney, B. A., Stocke, J. T., Danforth, C. W., et al. 2017, *ApJS*, 230, 6
- Keeney, B. A., Pratt, C. T., Stocke, J. T., et al. 2018, *ApJS*, 237, 11
- Klypin, A., Kravtsov, A. V., Valenzuela, O., & Prada, F. 1999, *ApJ*, 522, 82
- Klypin, A., Kravtsov, A. V., Bullock, J. S., & Primack, J. R. 2001, *ApJ*, 554, 903
- Le Brun, A. M. C., McCarthy, I. G., Schaye, J., & Ponman, T. J. 2014, *MNRAS*, 441, 1270
- Lehner, N., O'Meara, J. M., Fox, A. J., et al. 2014, *ApJ*, 788, 119
- Lehner, N., Howk, J. C., & Wakker, B. P. 2015, *ApJ*, 804, 79
- McCarthy, I. G., Schaye, J., Bird, S., & Le Brun, A. M. C. 2017, *MNRAS*, 465, 2936
- McGaugh, S. S., Schombert, J. M., Bothun, G. D., & de Blok, W. J. G. 2000, *ApJL*, 533, L99
- Montero-Dorta, A. D. & Prada, F. 2009, *MNRAS*, 399, 1106
- More, S., Diemer, B., & Kravtsov, A. V. 2015, *ApJ*, 810, 36
- Mulchaey, J. S., Davis, D. S., Mushotzky, R. F., & Burstein, D. 1996, *ApJ*, 456, 80
- Mulchaey, J. S. 2000, *ARA&A*, 38, 289
- Murray, S., Power, C., & Robotham, A., 2013, *Astronomy and Computing*, 3, 23
- Nelson, D., Kauffmann, G., Pillepich, A., et al. 2018, *MNRAS*, 447, 450
- Nicastro, F., Kaastra, J., Krongold, Y., et al. 2018, *Nature*, 558, 406
- Oppenheimer, B. D., Davé, R., Katz, N., Kollmeier, J. A., & Weinberg, D. H. 2012, *MNRAS*, 420, 829
- Osmond, J. P. F. & Ponman, T. J. 2004, *MNRAS*, 350, 1511
- Pagel, B. E. J. 2009, *Nucleosynthesis and Chemical Evolution of Galaxies*, Cambridge, UK: Cambridge University Press
- Pisani, A., Ramella, M., & Geller, M. J. 2003, *AJ*, 126, 1677
- Planck Collaboration, Ade, P. A. R., Aghanim, N., et al. 2014, *A&A*, 571, A16
- Pratt, C. T., Stocke, J. T., Keeney, B. A., & Danforth, C. W. 2017, *ApJ*, in press (arXiv:1706.05103)
- Prochaska, J. X., Weiner, B., Chen, H.-W., Mulchaey, J., & Cooksey, K. 2011, *ApJ*, 740, 91
- Prochaska, J. X., Werk, J. K., Worseck, G., et al. 2017, *ApJ*, 837, 169
- Proctor, R. N., Mendes de Oliveira, C., Azanha, L., Dupke, R., & Overzier, R. 2015, *MNRAS*, 449, 2345
- Rauch, M. 1998, *ARA&A*, 36, 267
- Savage, B. D., Narayanan, A., Wakker, B. P., et al. 2010, *ApJ*, 719, 1526
- Savage, B. D., Kim, T.-S., Keeney, B., et al. 2012, *ApJ*, 753, 80
- Savage, B. D., Kim, T.-S., Wakker, B. P., et al. 2014, *ApJS*, 212, 8 (Paper 1)
- Schaye, J., Crain, R. A., Bower, R. G., et al. 2015, *MNRAS*, 446, 521
- Schneider, D. P., Hartig, G. F., Jannuzi, B. T., et al. 1993, *ApJS*, 87, 45
- Shull, J. M., Smith, B. D., & Danforth, C. W. 2012, *ApJ*, 759, 23
- Steidel, C. C., Erb, D. K., Shapley, A. E., et al. 2010, *ApJ*, 717, 289
- Stocke, J. T., Penton, S. V., Danforth, C. W., et al. 2006, *ApJ*, 641, 217
- Stocke, J. T., Keeney, B. A., & Danforth, C. W. 2010, *PASA*, 27, 256
- Stocke, J. T., Keeney, B. A., Danforth, C. W., et al. 2013, *ApJ*, 763, 148
- Stocke, J. T., Keeney, B. A., Danforth, C. W., et al. 2014, *ApJ*, 791, 128 (Paper 2)
- Stocke, J. T., Keeney, B. A., Danforth, C. W., et al. 2017, *ApJ*, 838, 37
- Tejos, N., Rodríguez-Puebla, A., & Primack, J. R. 2018, *MNRAS*, 473, 366
- Terrell, D. G. & Scott, D. W. 1992, *AnSta*, 20, 1236
- Thom, C., Tumlinson, J., Werk, J. K., et al. 2012, *ApJL*, 758, L41
- Tinker, J., Kravtsov, A. V., Klypin, A., et al. 2008, *ApJ*, 688, 709
- Tremonti, C. A., Heckman, T. M., Kauffmann, G., et al. 2004, *ApJ*, 613, 898
- Tumlinson, J., Giroux, M. L., Shull, J. M. & Stocke, J. T. 1999, *AJ*, 118, 2148
- Tumlinson, J., Thom, C., Werk, J. K., et al. 2011, *Science*, 334, 948
- Tumlinson, J., Thom, C., Werk, J. K., et al. 2013, *ApJ*, 777, 59
- Tumlinson, J., Peebles, M. S., & Werk, J. K. 2017, *ARA&A*, 55, 389
- Wakker, B. P., Hernandez, A. K., French, D. M., et al. 2015, *ApJ*, 814, 40
- Werk, J. K., Prochaska, J. X., Thom, C., et al. 2013, *ApJS*, 204, 17
- Werk, J. K., Prochaska, J. X., Tumlinson, J., et al. 2014, *ApJ*, 792, 8
- Wu, X.-P., Xue, Y.-J., & Fang, L.-Z. 1999, *ApJ*, 524, 22
- Yoon, J. H., Putman, M. E., Thom, C., Chen, H.-W., & Bryan, G. L. 2012, *ApJ*, 754, 84
- Yoon, J. H., & Putman, M. E. 2013, *ApJL*, 772, L29
- Yoon, J. H., & Putman, M. E. 2017, *ApJ*, 839, 117

## APPENDIX

## A. NOTES ON ABSORPTION TOWARD INDIVIDUAL SIGHT LINES

Table 10 lists the species, redshift, velocity offset with respect to the SDSS group redshift, significance level, equivalent width, Doppler  $b$ -value, and column density of all absorbers detected within  $\pm 1000 \text{ km s}^{-1}$  of the SDSS group redshifts. Figure 1 shows the portions of the COS/G130M spectra over approximately the same range. The absorption toward each sight line is discussed below.

A.1. *Group 12833;  $z_0 = 0.14693$ , RBS 711*

A single, narrow H I absorber is seen at  $\Delta v_{\text{abs}} = +129 \text{ km s}^{-1}$  with respect to the SDSS group redshift in both Ly $\alpha$  and Ly $\beta$ . A CoG analysis of these lines is poorly constrained, but is consistent with the individual line fits of  $\log N_{\text{HI}} = 14.6\text{--}15.0$  and  $b = 20\text{--}25 \text{ km s}^{-1}$ . Despite high S/N data, no O VI 1032 absorption is seen corresponding to the H I lines. A weak Si III line shows that metals are present in this system, but that the ionization state and temperature are likely low. This is consistent with the temperature inferred from the narrow Lyman line profiles ( $T \lesssim 80,000 \text{ K}$ ).

A.2. *Group 16803;  $z_0 = 0.14839$ , SDSS J1540–0205*

This sight line probes one of the richest groups in our sample ( $N = 10$  SDSS galaxies; 56 galaxies identified by additional MOS; see Table 8 in Section 4.4) at an impact parameter of  $0.5 R_{\text{grp}}$ . The background AGN was predicted to have a flux of  $\sim 2 \times 10^{-15} \text{ erg s}^{-1} \text{ cm}^{-2} \text{ \AA}^{-1}$  based on GALEX FUV and NUV fluxes and a detection by Swift/UVOT in the UVW1 channel. However, the observed flux was only about half of this due to a previously unknown partial Lyman limit system at the AGN redshift ( $z_{\text{em}} = 0.322$ ). This means that the continuum level blueward of  $\sim 1220 \text{ \AA}$  is only  $\sim 5 \times 10^{-17} \text{ erg s}^{-1} \text{ cm}^{-2} \text{ \AA}^{-1}$ . The data quality around  $1400 \text{ \AA}$  (the region of Ly $\alpha$  at the group redshift) is adequate ( $S/N \approx 15$  per resel) for the Ly $\alpha$  and Si III regions. However,  $S/N \sim 2\text{--}3$  for the O VI and Ly $\beta$  regions of interest ( $\lambda < 1200 \text{ \AA}$ ). The only absorption in the redshift range of the group is a single (presumed to be) Ly $\alpha$  line at  $1392 \text{ \AA}$  ( $\Delta v_{\text{abs}} = -893 \text{ km s}^{-1}$ ). The low data quality at  $\lambda < 1200 \text{ \AA}$  precludes stringent limits to O VI absorption, but no absorption is apparent in either line of the doublet.

A.3. *Group 19670;  $z_0 = 0.13443$ , SBS 0956+510*

Strong H I absorption at  $z = 0.13388$  is seen in Ly $\alpha$  and Ly $\beta$ . A CoG solution gives  $\log N_{\text{HI}} = 15.7$ : and  $b = 17$ :  $\text{km s}^{-1}$ , which fits line profiles reasonably well. A weaker feature at  $\lambda = 1376.9 \text{ \AA}$  is identified as a possible Ly $\alpha$  line at  $\Delta v_{\text{abs}} = +1069 \text{ km s}^{-1}$  ( $z = 0.13267$ ,  $\log N_{\text{HI}} = 13.1 \pm 0.1$ ,  $b = 29 \pm 7 \text{ km s}^{-1}$ ) just off the right-hand edge of Figure 1. No O VI is seen at the redshift of either H I component. O VI 1032  $\text{\AA}$  at the SDSS group redshift is blended with Ly $\beta$  at  $z_{\text{abs}} = 0.1415$ , but no O VI 1038  $\text{\AA}$  absorption is seen at any redshift.

A.4. *Group 25124;  $z_0 = 0.18613$ , B 1612+266*

A strong Ly $\alpha$  absorption line lies very close to the expected group redshift in this sight line ( $z_{\text{abs}} = 0.1853$ ,  $\Delta v_{\text{abs}} = -212 \text{ km s}^{-1}$ ). Strong, broad O VI 1038  $\text{\AA}$  absorption is detected ( $\log N_{\text{OVI}} = 14.49 \pm 0.05$ ,  $b = 54 \pm 6 \text{ km s}^{-1}$ ) at a slightly higher redshift (see Section 3.2), but the stronger O VI 1032  $\text{\AA}$  line is blended with the H I Ly10 line of a partial LLS at  $z_{\text{abs}} = 0.3306$ .

We analyze the blended line in two ways: first, we use the unblended H I lines of the partial LLS to model the column density and  $b$ -value of the system; Ly 6-9 and 11-15 are clearly present in the data and show no obvious blending with other systems. A curve-of-growth (CoG) analysis gives a solution of  $\log N_{\text{HI}} = 16.60 \pm 0.02$ ,  $b = 27 \pm 2 \text{ km s}^{-1}$ .

With this information, we model the partial LLS absorption from the data and recover the O VI 1032  $\text{\AA}$  line, which appears consistent with the weaker 1038  $\text{\AA}$  line. We check this for consistency with a second method that uses the observed O VI 1038  $\text{\AA}$  line as a model and subtracts it from the data near the O VI+Ly10 blend at  $1223 \text{ \AA}$ , yielding a Ly10 profile consistent with the CoG solution.

In addition to H I Ly $\alpha$  and O VI, corresponding absorption is also seen in Si III 1206.5 and Si II 989, 1190, 1193 at  $z_{\text{abs}} = 0.1853$ . Corresponding Ly $\beta$  absorption is obscured in the Galactic Ly $\alpha$  profile and is unrecoverable. This system is discussed in detail in Section 3.2.

**Table 10.** Absorption lines measured within  $2.5\sigma_0$  of SDSS group velocities

Species	$z_{\text{abs}}$	$\Delta v_{\text{abs}}$ ( $\text{km s}^{-1}$ )	S.L. ( $\sigma$ )	$\text{EW}_r$ ( $\text{m}\text{\AA}$ )	$b$ ( $\text{km s}^{-1}$ )	$\log N$ ( $N$ in $\text{cm}^{-2}$ )
RBS711, Group #12833; $z_0 = 0.14693$						
$\text{Ly}\alpha$ 1215	0.14743	129	42.8	$333 \pm 33$	$23 \pm 2$	$14.65 \pm 0.19$
$\text{Ly}\beta$ 1025	0.14743	131	31.7	$241 \pm 14$	$24 \pm 1$	$15.03 \pm 0.07$
Si III 1206	0.14742	127	6.9	$42 \pm 10$	$15 \pm 4$	$12.37 \pm 0.09$
SDSS J15403-0205, Group #16803; $z_0 = 0.14839$						
$\text{Ly}\alpha$ 1215	0.14497	-893	7.1	$110 \pm 17$	$27 \pm 5$	$13.41 \pm 0.07$
SBS0956+509, Group #19670; $z_0 = 0.13443$						
$\text{Ly}\alpha$ 1215	0.13388	-146	30.7	$335 \pm 26$	$25 \pm 2$	$14.49 \pm 0.12$
$\text{Ly}\alpha$ 1215	0.13848	1069	5.3	$51 \pm 9$	$38 \pm 8$	$13.01 \pm 0.07$
$\text{Ly}\beta$ 1025	0.13387	-146	20.8	$233 \pm 15$	$26 \pm 2$	$14.90 \pm 0.05$
QSOB1612+266, Group #25124; $z_0 = 0.18613$						
$\text{Ly}\alpha$ 1215	0.18529	-212	49.7	$705 \pm 77$	$37 \pm 3$	$15.81 \pm 0.33$
$\text{Ly}\alpha$ 1215	0.18569	-110	9.0	$120 \pm 10$	$32 \pm 4$	$13.44 \pm 0.05$
O VI 1032	0.18540	-184	13.0	$248 \pm 90$	$53 \pm 4$	$14.49 \pm 0.05$
O VI 1038	0.18540	-184	13.0	$160 \pm 21$	$53 \pm 4$	$14.49 \pm 0.05$
Si III 1206	0.18517	-242	9.7	$150 \pm 25$	$59 \pm 10$	$12.92 \pm 0.08$
Si III 1206	0.18531	-208	32.7	$364 \pm 22$	$30 \pm 2$	$13.80 \pm 0.07$
C III 977	0.18520	-234	9.5	$289 \pm 129$	$38 \pm 11$	$13.98 \pm 0.45$
C III 977	0.18537	-191	13.7	$323 \pm 83$	$21 \pm 4$	$15.32 \pm 0.72$
N III 989	0.18543	-176	14.8	$215 \pm 21$	$34 \pm 3$	$14.54 \pm 0.05$
Si II 1190	0.18529	-212	13.9	$166 \pm 15$	$33 \pm 2$	$13.79 \pm 0.04$
Si II 1193	0.18531	-207	16.5	$199 \pm 103$	$28 \pm 1$	$13.65 \pm 0.02$
SDSSJ133300.83+451809.0, Group #32123; $z_0 = 0.15971$						
$\text{Ly}\alpha$ 1215	0.15874	-251	37.1	$643 \pm 67$	$41 \pm 4$	$15.10 \pm 0.22$
$\text{Ly}\alpha$ 1215	0.16081	283	15.7	$234 \pm 20$	$22 \pm 2$	$14.02 \pm 0.07$
$\text{Ly}\alpha$ 1215	0.16142	442	4.5	$95 \pm 30$	$49 \pm 13$	$13.29 \pm 0.11$
$\text{Ly}\beta$ 1025	0.15860	-285	10.1	$136 \pm 32$	$15 \pm 4$	$14.67 \pm 0.15$
$\text{Ly}\beta$ 1025	0.15887	-218	16.2	$295 \pm 33$	$32 \pm 4$	$15.03 \pm 0.07$
$\text{Ly}\beta$ 1025	0.16090	306	4.8	$46 \pm 15$	$11 \pm 6$	$13.94 \pm 0.13$
O VI 1032	0.16088	302	2.3	$36 \pm 15$	$29 \pm 13$	$13.55 \pm 0.25$
O VI 1038	0.16082	288	3.0	$44 \pm 35$	$33 \pm 16$	$13.89 \pm 0.28$
Si III 1206	0.15883	-227	6.0	$77 \pm 16$	$15 \pm 4$	$12.69 \pm 0.09$
Si III 1206	0.16079	278	2.9	$24 \pm 11$	$5 \pm 0$	$12.19 \pm 0.21$

*Table 10 continued*

**Table 10** (*continued*)

Species	$z_{\text{abs}}$	$\Delta v_{\text{abs}}$ ( $\text{km s}^{-1}$ )	S.L. ( $\sigma$ )	$\text{EW}_r$ ( $\text{m}\text{\AA}$ )	$b$ ( $\text{km s}^{-1}$ )	$\log N$ ( $N$ in $\text{cm}^{-2}$ )
SDSSJ10282+2119, Group #36001; $z_0 = 0.18788$						
Ly $\alpha$ 1215	0.18429	−906	35.3	$507 \pm 32$	$38 \pm 2$	$14.68 \pm 0.09$
Ly $\alpha$ 1215	0.18494	−743	5.5	$46 \pm 25$	$17 \pm 11$	$13.00 \pm 0.22$
Ly $\alpha$ 1215	0.18527	−659	44.8	$523 \pm 106$	$28 \pm 5$	$15.56 \pm 0.62$
Ly $\alpha$ 1215	0.18585	−513	27.9	$367 \pm 43$	$26 \pm 2$	$14.63 \pm 0.18$
Ly $\gamma$ 972	0.18526	−660	18.7	$344 \pm 12$	$18 \pm 0$	$18.00 \pm 0.00$
Ly $\gamma$ 972	0.18592	−494	8.5	$172 \pm 28$	$23 \pm 5$	$15.16 \pm 0.09$
O VI 1032	0.18436	−887	4.1	$42 \pm 36$	$32 \pm 10$	$13.56 \pm 0.43$
O VI 1032	0.18530	−651	3.6	$30 \pm 1$	$23 \pm 9$	$13.43 \pm 0.13$
O VI 1038	0.18432	−898	3.6	$24 \pm 2$	$18 \pm 8$	$13.63 \pm 0.17$
Si III 1206	0.18527	−658	8.1	$90 \pm 21$	$29 \pm 4$	$12.71 \pm 0.09$
C III 977	0.18532	−646	3.8	$65 \pm 24$	$22 \pm 7$	$13.10 \pm 0.14$
C III 977	0.18604	−464	4.4	$111 \pm 38$	$66 \pm 14$	$13.29 \pm 0.07$
CSO1022, Groups #44564, 44565; $z_0 = 0.14506, 0.14925$ [no absorbers]						
CSO1080, Group #44726; $z_0 = 0.15208$ [no absorbers]						
FBQSJ1519+2838, Group #44739; $z_0 = 0.11839$						
Ly $\alpha$ 1215	0.11537	−808	46.6	$497 \pm 40$	$32 \pm 2$	$14.98 \pm 0.21$
Ly $\alpha$ 1215	0.11706	−357	36.7	$436 \pm 39$	$30 \pm 2$	$14.78 \pm 0.17$
Ly $\alpha$ 1215	0.11766	−195	35.6	$509 \pm 48$	$37 \pm 3$	$14.72 \pm 0.11$
Ly $\alpha$ 1215	0.11795	−118	17.2	$191 \pm 26$	$21 \pm 3$	$13.84 \pm 0.09$
Ly $\beta$ 1025	0.11535	−814	19.9	$325 \pm 30$	$32 \pm 3$	$15.20 \pm 0.12$
Ly $\beta$ 1025	0.11704	−362	26.2	$290 \pm 54$	$25 \pm 4$	$15.34 \pm 0.28$
Ly $\beta$ 1025	0.11762	−205	20.8	$304 \pm 30$	$31 \pm 3$	$15.11 \pm 0.09$
Ly $\beta$ 1025	0.11793	−123	6.1	$77 \pm 21$	$22 \pm 7$	$14.13 \pm 0.11$
O VI 1032	0.11551	−773	3.2	$26 \pm 19$	$10 \pm 10$	$13.39 \pm 0.33$
O VI 1032	0.11766	−197	3.6	$49 \pm 27$	$40 \pm 15$	$13.63 \pm 0.18$
Si III 1206	0.11526	−839	4.9	$85 \pm 31$	$64 \pm 15$	$12.64 \pm 0.12$
Si III 1206	0.11709	−348	4.6	$30 \pm 29$	$5 \pm 0$	$12.32 \pm 0.12$
Si III 1206	0.11765	−197	5.2	$53 \pm 12$	$17 \pm 4$	$12.48 \pm 0.09$
FBQSJ1519+2838, Group #44858; $z_0 = 0.12740$						
Ly $\alpha$ 1215	0.12551	−501	61.2	$581 \pm 166$	$29 \pm 6$	$15.94 \pm 0.96$
Ly $\alpha$ 1215	0.12567	−460	32.4	$372 \pm 189$	$43 \pm 13$	$14.12 \pm 0.49$
Ly $\beta$ 1025	0.12550	−504	30.8	$365 \pm 75$	$30 \pm 5$	$15.57 \pm 0.37$
Ly $\beta$ 1025	0.12568	−457	20.6	$211 \pm 147$	$21 \pm 28$	$15.00 \pm 2.36$
O VI 1032	0.12571	−449	9.8	$93 \pm 12$	$21 \pm 3$	$14.01 \pm 0.06$
O VI 1038	0.12571	−450	5.1	$52 \pm 15$	$20 \pm 6$	$14.00 \pm 0.10$
FBQSJ103059.1+310255, Group #50433; $z_0 = 0.13599$ [no absorbers]						

NOTE—Column 3 lists the velocity offset between the absorber and the SDSS group redshift in Table 2, and Column 4 lists the significance level of the detected absorption.

<sup>a</sup>O VI in this sight line is obscured by a partial LLS at  $z = 0.322$ .

A.5. *Group 32123*;  $z_0 = 0.15971$ , *SDSS J1333+4518*

Several strong absorbers are present in this sight line at  $v_{\text{grp}} \pm 500 \text{ km s}^{-1}$  though none at  $|\Delta v_{\text{abs}}| < 200 \text{ km s}^{-1}$ . Strong Ly $\alpha$  systems are seen at  $z = 0.15874$  and  $z = 0.16081$ , bracketing the SDSS group redshift. The blue system shows two components in Ly $\beta$  while the red system shows a single Ly $\beta$  component along with weak O VI absorption in both lines of the doublet. Both red and blue absorbers show weak Si III absorption though the red Si III detection is marginal ( $\sim 2.8\sigma$ ). A possible metal-free BLA is in this group at  $z=0.16142$  ( $\Delta v_{\text{abs}} = +442 \text{ km s}^{-1}$ ).

A.6. *Group 36001*;  $z_0 = 0.18788$ , *SDSS J1028+2119*

While there is no absorption at the SDSS group redshift, three strong Ly $\alpha$  lines are found at  $\Delta v_{\text{abs}} = -1100$  to  $-500 \text{ km s}^{-1}$ . The first absorber at  $z=0.18429$  ( $\Delta v_{\text{abs}} = -906 \text{ km s}^{-1}$ ) is outside the relative velocity bounds established for association with this group. There is also weak O VI 1031, 1038 Å absorption associated with the  $z=0.18527$  Ly $\alpha$  absorber. Relative to the SDSS group centroid and virial radius, this sight line has the smallest impact parameter ( $\rho_* = 295 \text{ kpc}$ ) in our sample.

A.7. *Groups 44565, 44564*;  $z_0 = 0.14925, 0.14506$ , *CSO 1022*

This archival dataset probes two SDSS groups  $\sim 1200 \text{ km s}^{-1}$  apart, which were shown to be parts of a single, much more massive group (see [Appendix B](#)). While a low-significance feature ( $2.8\sigma$ ) is consistent with O VI 1032 Å absorption at the redshift of group 44564, it is identified as O VI 1038 Å absorption from the unrelated, strong  $z = 0.1387$  system (confirmed via H I and other metal lines at  $z = 0.1387$ ). No absorption is seen in H I through either Ly $\alpha$  or Ly $\beta$  near the redshift of either group. The group characterization analysis discussed in [Section 4.4](#) merges these two groups into one, with velocity centroid between the values above and sky position very close to the centroids of the two SDSS groups.

A.8. *Group 44726*;  $z_0 = 0.15208$ , *CSO 1080*

The long IGM sight line ( $z_{\text{em}} = 0.526$ ) toward this background AGN provides a complicated absorption-line population against which we must measure absorption from the group. Nevertheless, there is no H I absorption within  $|\Delta v_{\text{abs}}| < 1000 \text{ km s}^{-1}$  of the SDSS group redshift, though a strong H I system is found at  $\Delta v_{\text{abs}} = +1300 \text{ km s}^{-1}$ .

A.9. *Groups 44739, 44858*;  $z_0 = 0.11839, 0.12740$ , *FBQS J1519+2838*

At the redshift of group 44739 ( $z_0 = 0.1184$ ), four strong H I lines are seen in both Ly $\alpha$  and Ly $\beta$  between  $-800$  and  $-100 \text{ km s}^{-1}$  from the SDSS group redshift. Two marginal O VI 1032 lines are seen which appear to correspond with the  $-808$  and  $-195 \text{ km s}^{-1}$  components. The potentially broad O VI 1032 Å detection is weak enough that it's consistent with a non-detection in the 1038 Å line. There is Si III absorption seen corresponding to three of the H I components as well.

For group 44858 ( $z_0 = 0.1274$ ), a single, strong H I absorber is best-fit as a pair of Ly $\alpha$  lines at  $\Delta v_{\text{abs}} = -501$  &  $-460 \text{ km s}^{-1}$  with respect to the SDSS group redshift. Moderate, narrow O VI absorption is seen in both lines of the doublet at very nearly the  $\Delta v_{\text{abs}} = -460 \text{ km s}^{-1}$  velocity. Si III at this redshift is blended with another intervening system and no other commonly seen low-ionization species are present in these data.

A.10. *Group 50433*;  $z_0 = 0.13599$ ; *FBQS J1030+3102*

High-S/N data at the expected O VI, Ly $\alpha$ , and Ly $\beta$  line locations show no absorption features in H I or O VI within  $\pm 1500 \text{ km s}^{-1}$  of the group velocity.

## B. NOTES ON PROPERTIES OF INDIVIDUAL GROUPS

[Figure 15](#) examines how the derived properties of the galaxy groups are related. These properties show a high level of discretization for the sparsest groups ( $N_{\text{grp}} \lesssim 10$ ), as well as strong correlations with  $M_{\text{grp}}$  through [Equation 5-6](#). Furthermore, there are often peaks for poor, low-mass and rich, high-mass configurations for a given group. Nevertheless, the group properties in [Table 8](#) are almost always within the  $1\sigma$  range of values derived from the individual Monte Carlo realizations ([Table 6](#)), indicating that the adopted group configurations are representative of the ensemble as a whole. This is reassuring but not surprising since we adopt the configuration that most closely matches the marginal distributions of these parameters ([Section 4.4](#)). Below, we discuss the properties of individual groups.

### B.1. *Group 12833*

The vast majority of the Monte Carlo realizations for this group have  $< 80$  members ([Table 6](#)), but there is a small tail up to  $\sim 150$  members ([Figure 15](#)). The group position is well-constrained in declination, but has two peaks in right ascension; the group

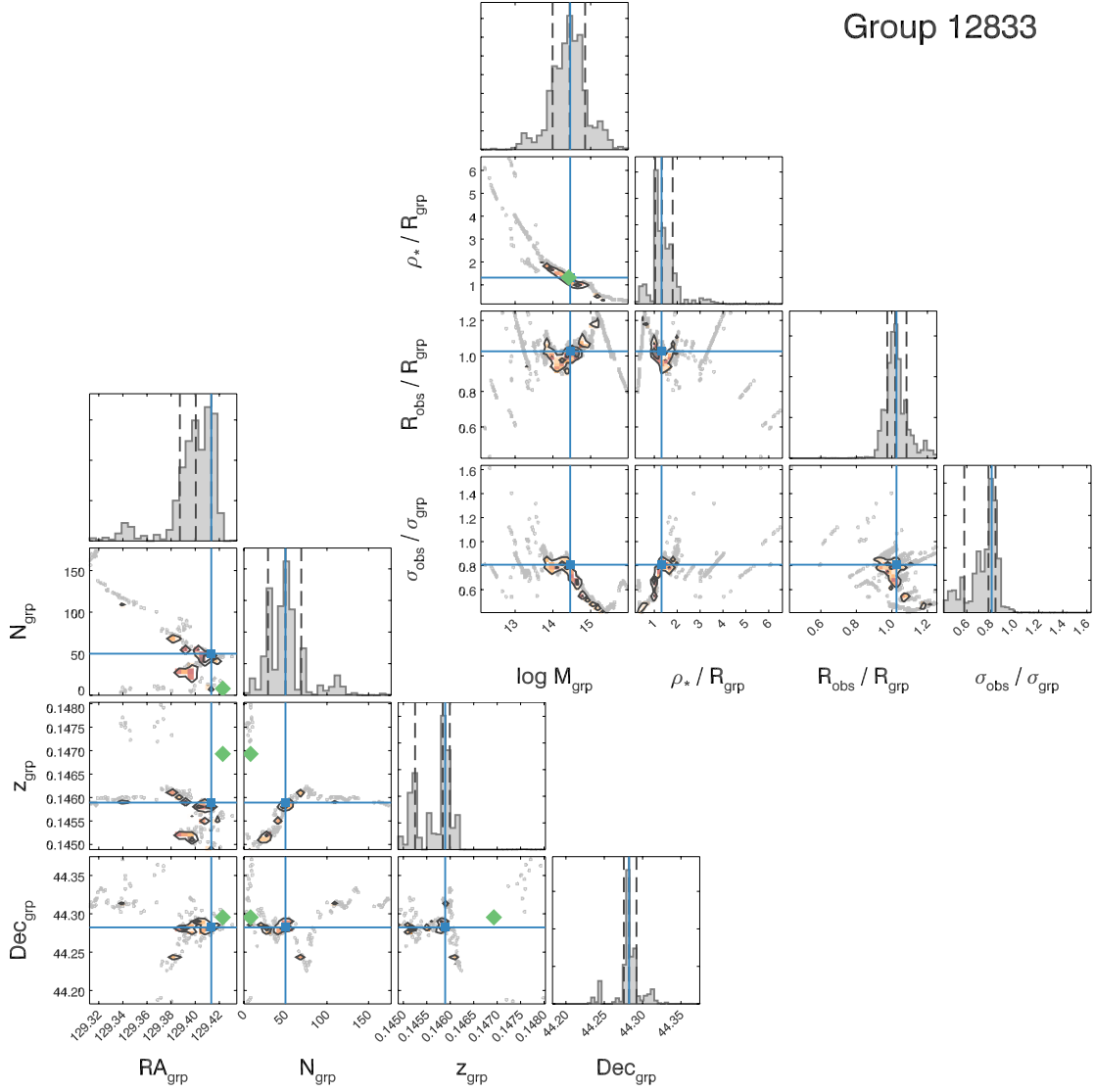


**Figure 15.** Exploration of parameter covariance for group 12833. Contours are drawn at  $1\sigma$  and  $2\sigma$  significance. Inside the  $2\sigma$  contour, data are color-coded according to density, with lighter colors indicating lower density. Outside the  $2\sigma$  contour, data from individual Monte Carlo realizations are shown as gray circles. Dashed lines in the histograms show the 16th, 50th, and 84th percentile values (i.e., the ranges listed in Table 6). Solid blue lines show the adopted values from Table 8 (see Section 4.4). Green diamonds show the values from the SDSS analysis in Table 2, where applicable.

redshift also shows two peaks separated by  $\sim 250 \text{ km s}^{-1}$ . The group mass shows a strong peak at  $\sim 10^{14.5} M_{\odot}$  and a weaker one at  $\sim 10^{13} M_{\odot}$ , and the impact parameter of the QSO is well constrained at  $\rho_{*} \approx 1.3 R_{\text{grp}}$ . The distributions of  $R_{\text{obs}}/R_{\text{grp}}$  and  $\sigma_{\text{obs}}/\sigma_{\text{grp}}$  are fairly broad, which is a general characteristic for all groups owing to the noisy nature of  $R_{\text{obs}}$  and  $\sigma_{\text{obs}}$ . The adopted group properties (blue lines) all fall within the  $1\sigma$  uncertainty.

### B.2. Group 16803

The properties of this group are all reasonably well constrained (Figure 37), except for the  $R_{\text{obs}}/R_{\text{grp}}$  and  $\sigma_{\text{obs}}/\sigma_{\text{grp}}$  values, whose marginal likelihoods have multiple peaks. The adopted group properties are all near the peaks of the marginal distributions.

### B.3. Group 19670

Most of the derived properties of this group show evidence for multiple peaks (Figure 38), suggesting that a relatively low-mass,  $\sim 50$ -member group and a higher-mass,  $\sim 90$ -member group are both common outcomes. The adopted group properties favor the lower mass configuration, and all fall within the  $1\sigma$  uncertainty.

#### B.4. Group 25124

This is perhaps the hardest group in our sample to characterize. The most common configurations (Figure 39) are a  $\sim 30$ -member, low-mass ( $\sim 10^{14.4} M_{\odot}$ ) group, and a  $\sim 40$ -member, high-mass ( $\sim 10^{14.8} M_{\odot}$ ) group; however, the richness distribution for the high-mass configuration is broad and extends up to  $\sim 50$  members. The group redshift distribution shows two peaks separated by  $\sim 300 \text{ km s}^{-1}$ , and the  $R_{\text{obs}}/R_{\text{grp}}$  and  $\sigma_{\text{obs}}/\sigma_{\text{grp}}$  distributions are also multi-modal. Confoundingly, the two group configurations evident in the richness and mass distributions do not correspond to two clear positions on the sky; instead there are  $\sim 5$  fairly common group positions in the Monte Carlo realizations. Our adopted group membership favors the most common of these positions, which corresponds to one of the low-mass group configurations.

#### B.5. Group 32123

The Monte Carlo realizations for this group tend to find  $\lesssim 20$  members (Figure 40), but there is a tail that extends up to  $\sim 50$  members. The group position on the sky shows a clearly favored position, but the group redshift is more widely distributed; the adopted group configuration matches the richness and favored position well. The mass and other derived properties also have multiple peaks in their distributions; the adopted group values are all in the high-density regions for these properties.

#### B.6. Group 36001

The Monte Carlo realizations all find a modest ( $< 15$ -member) group, with a 6-member configuration being the most common (Figure 41). Due to the small number of galaxies involved, the group position and redshift distributions tend to settle on a handful of discrete values. The mass and other derived properties show smoother distributions due to the uncertainty in  $\Upsilon_{\text{grp}}$  that is folded into the Monte Carlo process (see Section 4.3). The adopted group properties match the peaks in all of these quantities.

#### B.7. Groups 44564 & 44565

These two groups are both probed by the same QSO sight line (Table 1), and the initial SDSS analysis found them to be separated by  $1'8$  on the sky and  $1100 \text{ km s}^{-1}$  in redshift (Table 2). We find many galaxies at intermediate redshifts in this region of the sky, so the two SDSS groups merge into a single,  $\sim 115$ -member group by our analysis. The Monte Carlo realizations find positions and redshifts for the groups separated by  $\sim 10''$  on the sky and  $\sim 5 \text{ km s}^{-1}$  in redshift (Table 6), and all other derived (and adopted) group quantities are also nearly identical. The adopted position of the merged group is closer to the SDSS position of group 44565, but the adopted redshift is closer to the SDSS redshift of group 44564 (Table 8).

#### B.8. Group 44726

The vast majority of the Monte Carlo realizations find a modest group with  $< 30$  members, but there is a tail that extends all the way up to  $> 150$  members (Figure 44). This leads to a bimodality in the inferred mass and other derived quantities. Our adopted group properties lie near the peaks of all of the parameter distributions, and prefer a low mass ( $\sim 10^{13.4} M_{\odot}$ ) group. The adopted 7-member group is also remarkably compact, with  $R_{\text{obs}} < 200 \text{ kpc}$  (Table 8).

#### B.9. Group 44739

Groups 44739 and 44858 are probed by the same QSO sight line (Table 1). However, the initial SDSS analysis found them to be much more separated ( $30'$  on the sky and  $2400 \text{ km s}^{-1}$  in redshift; Table 2) than Groups 44564 and 44565, so they do not merge into a single, larger group by our analysis. Thus, we continue to discuss their properties separately.

Most of the Monte Carlo realizations find groups with  $\lesssim 100$  members, but occasionally they will merge this group with Group 44858, which allows the group to grow to several hundred members (Figure 45). Ignoring this low-frequency tail, the group position, richness, and redshift are well-constrained. The inferred mass and other derived group properties are also well-behaved. The adopted group properties are all near the peaks of the marginal distributions.

#### B.10. Group 44858

As with Group 44739, most of the Monte Carlo realizations have  $< 100$  members, but there is a low-frequency tail that extends up to  $\sim 600$  members when the two groups occasionally merge (Figure 46). Outside of these rare cases the group properties are well-constrained. The adopted group properties match the peaks of the marginal distributions, except for  $R_{\text{obs}}/R_{\text{grp}}$  and  $\sigma_{\text{obs}}/\sigma_{\text{grp}}$ , which lie outside the  $1\sigma$  uncertainty.

#### B.11. Group 50433

The Monte Carlo realizations almost always find  $< 40$  members in this group (Figure 47), with several discrete positions, richnesses, and redshifts. The distributions of inferred mass and other derived quantities are smooth and well-behaved, and the adopted group properties are near the peaks of all of these quantities.

## C. SUPPLEMENTAL MATERIAL

This is not a real section. It includes the full set of Figures and Tables that will be combined into the various Figure Sets and machine-readable Tables above after acceptance. It is included for completeness.

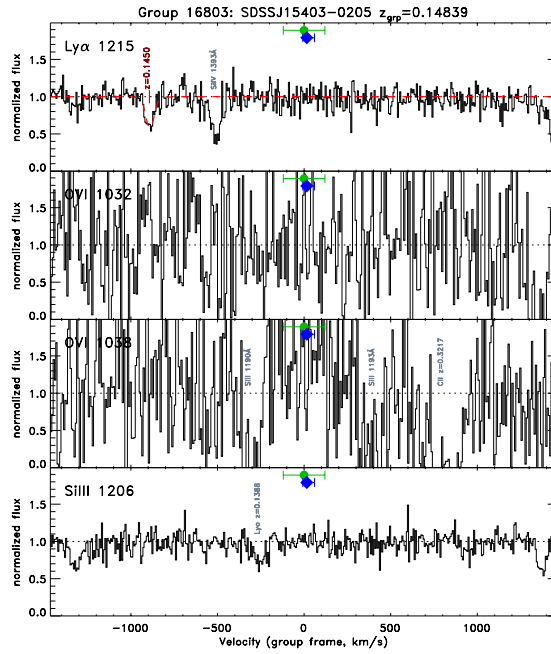


**Figure 16.** Same as Figure 1, but for group 16803. A weak Ly $\alpha$  line is seen, but no O VI is detected. The continuum is severely depressed due to a higher redshift LLS at the wavelength where OVI would appear at the group redshift. Therefore, this spectrum has an inconclusive result on the possibility of hot gas in this group.

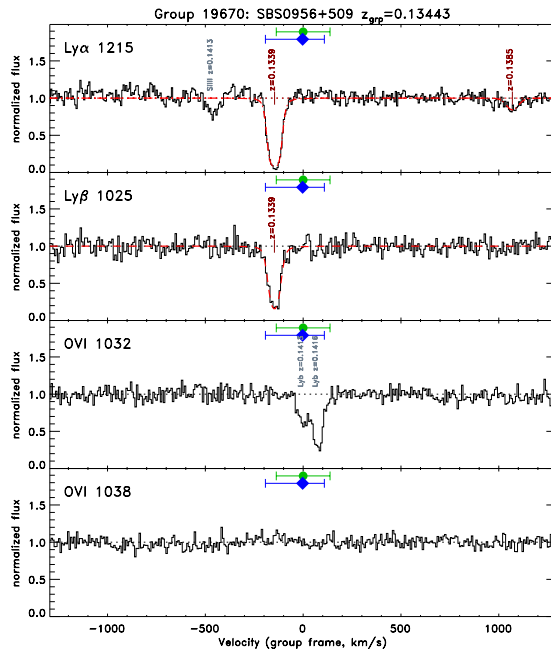


**Figure 17.** Same as Figure 1, but for group 19670. Strong H I absorption is seen near the group velocity, but no corresponding O VI absorption is seen.

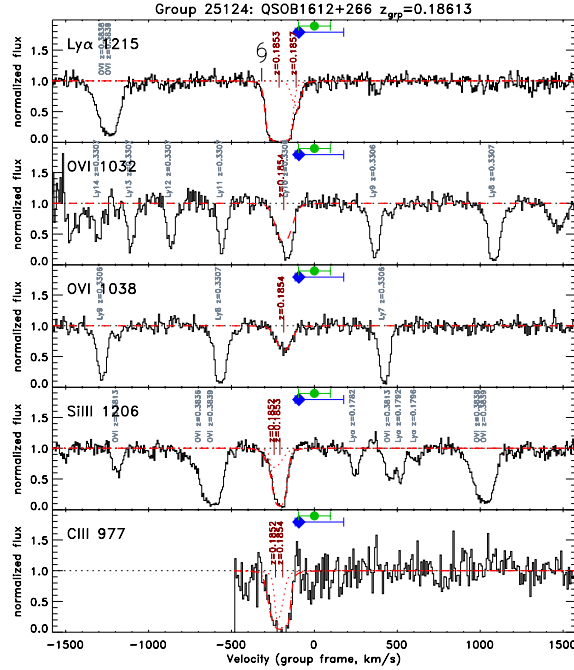


**Figure 18.** Same as Figure 1, but for group 25124. Strong Ly $\alpha$  absorption is seen at  $\Delta v_{\text{abs}} = -212 \text{ km s}^{-1}$  along with O VI 1038 absorption. The corresponding O VI 1032 Å line is blended with a partial LLS Ly10 line, and attempts to recover this line using the observed Lyman series of the partial LLS successfully obtain a line strength and width consistent with the 1038 Å detection. Because the O VI lines are significantly offset in velocity from the narrow H I lines in the fit displayed here and listed in Table 10, the Ly $\alpha$  complex was refit as discussed in Section 3.2 with the result that a BLA is likely present coincident in velocity with the O VI lines. The galaxy symbol marks the redshift of the nearest galaxy to this absorber 168 kpc ( $0.6 R_{\text{vir}}$ ) away, to which these absorptions are likely associated.

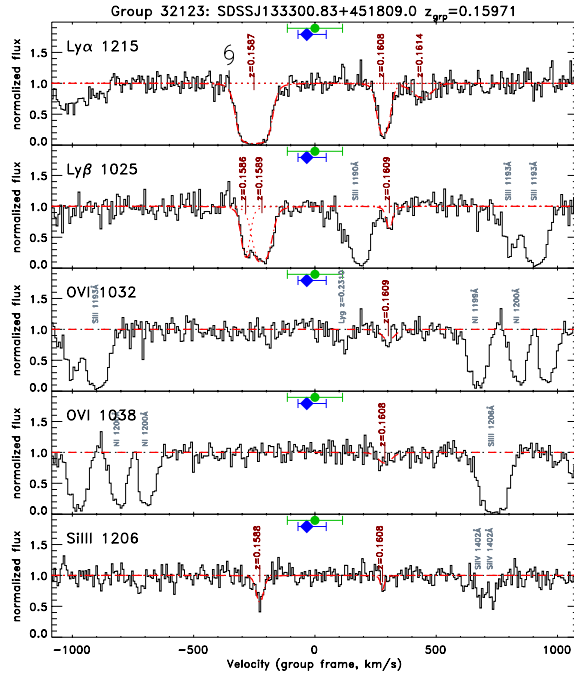


**Figure 19.** Same as Figure 1, but for group 32123. While no absorption is seen right at the SDSS group redshift, strong Ly $\alpha$  features are seen at  $\Delta v_{\text{abs}} = -251$  and  $+283 \text{ km s}^{-1}$ . A metal-free BLA is associated with this group at  $\Delta v_{\text{abs}} = +442 \text{ km s}^{-1}$

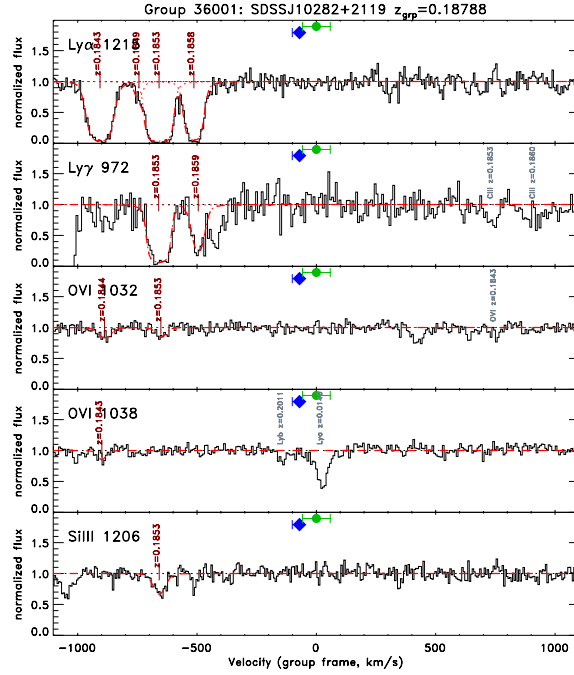


**Figure 20.** Same as Figure 1, but for group 36001. Weak O VI 1032 and, C III & Si III absorbers are aligned with an H I system at  $\Delta v_{\text{abs}} = -659 \text{ km s}^{-1}$ . Two other Ly $\alpha$  absorbers are present at higher negative relative velocities; the highest at  $\Delta v_{\text{abs}} = -906 \text{ km s}^{-1}$  is outside the velocity bounds we have considered for associated with this group.

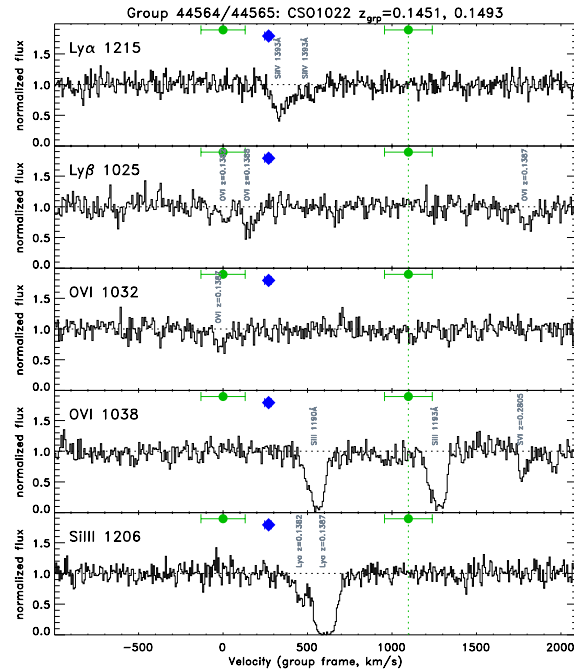


**Figure 21.** Same as Figure 1, but for groups 44564 and 44565, for which our detailed analysis finds only a single group (see Table 8). The apparent Ly $\beta$  and O VI absorption at  $z \approx 0.1451$  is coincidental and is, in fact, intervening O VI from two lower-redshift systems with corroborating H I Ly $\alpha$  and Ly $\beta$  absorption. A marginal ( $< 3\sigma$ ) detection is found consistent with very weak O VI absorption at  $z = 0.1493$ , but this absorber could also be plausibly identified as H I Ly $\gamma$  at  $z = 0.2195$ . No other O VI or H I absorption is seen associated with either group.

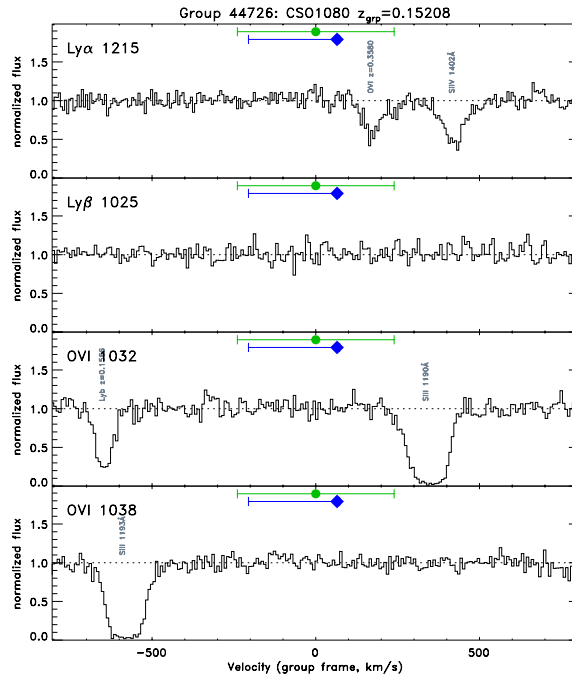


**Figure 22.** Same as Figure 1, but for group 44726. Strong H I absorption is seen at  $\Delta v_{abs} = +1300 \text{ km s}^{-1}$ , but no absorption is seen at the SDSS group velocity. Numerous interstellar and unrelated intergalactic lines render the possibility for blended lines high.

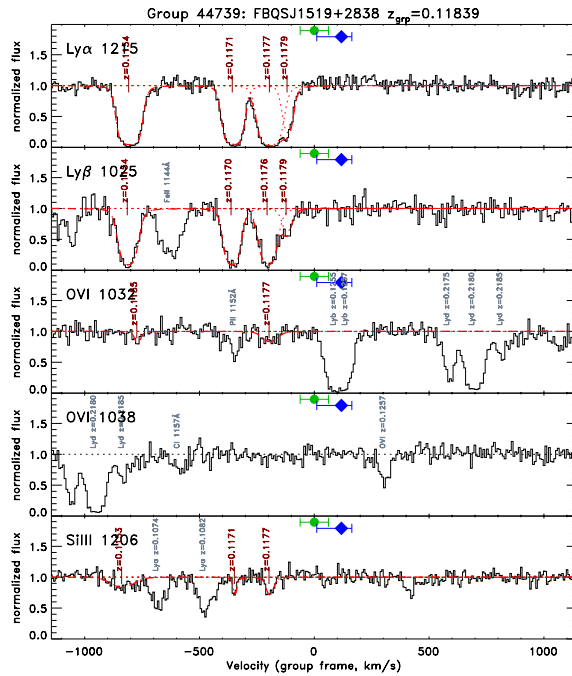


**Figure 23.** Same as Figure 1, but for group 44739. Strong H I absorption is seen at  $\Delta v_{abs} \approx -800$  to  $-120 \text{ km s}^{-1}$ . Two weak features are consistent with O VI 1032 absorption corresponding to two of the strong H I components. Weak Si III absorption is also seen coincident with two H I velocity components.

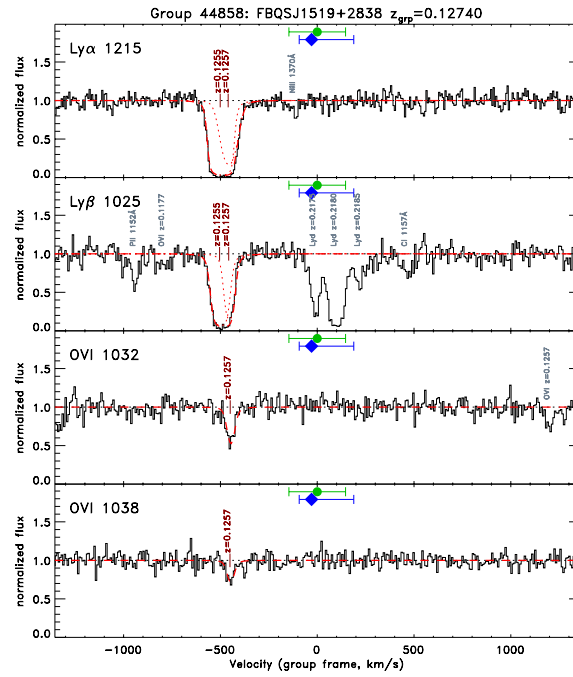


**Figure 24.** Same as Figure 1, but for group 44858. Strong H I is aligned with moderate O VI absorption at  $\Delta v_{\text{abs}} = -460 \text{ km s}^{-1}$ . A second H I component at  $\Delta v_{\text{abs}} = -501 \text{ km s}^{-1}$  is metal-free.

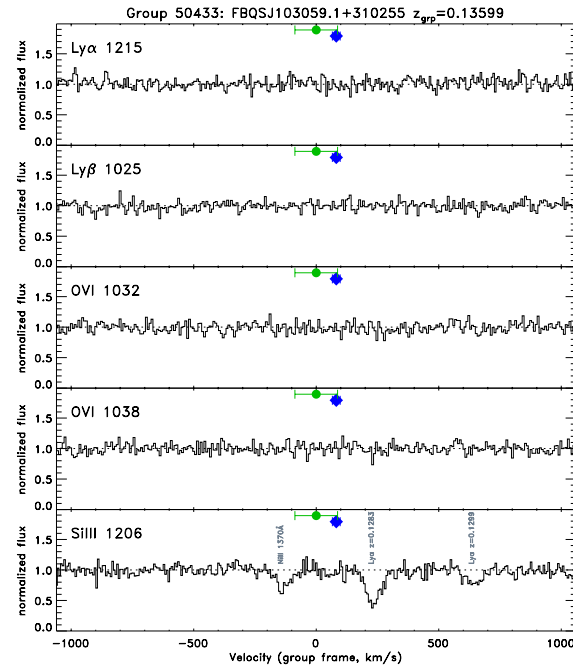


**Figure 25.** Same as Figure 1, but for group 50433. No absorption is seen in any species near the group redshift.

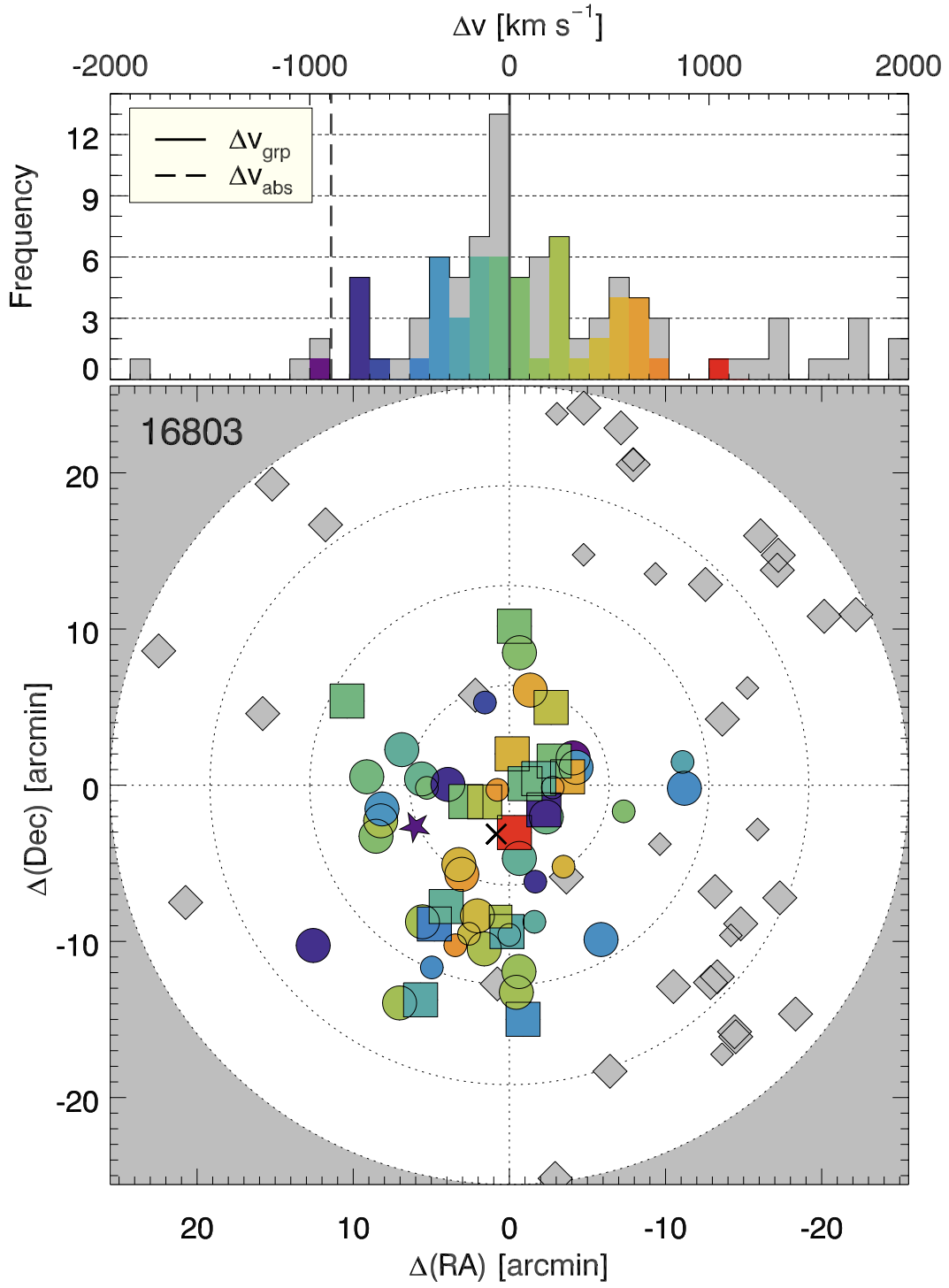


Figure 26. Same as Figure 4, but for the galaxy group 16803.

**Table 11.** Members of Group 16803

Name	RA	Dec	$z_{\text{gal}}$	$L_{\text{gal}}$	Type	$\Delta\rho$	$\Delta v$	$f_{\text{mem}}$
(1)	(2)	(3)	(4)	( $L^*$ ) (5)	(6)	(kpc) (7)	( $\text{km s}^{-1}$ ) (8)	(%) (9)
1237655498141270296	234.964227	-2.038841	0.14815	6.80	A	158	-63	99.7
sdss1540_275_503	234.941540	-2.074340	0.14812	1.03	A	488	-70	99.7
1237655498141270269	234.949579	-2.033421	0.14790	2.01	C	302	-127	99.6
1237655691945836795	234.933090	-2.014718	0.14841	2.31	C	510	5	99.6
sdss1540_254_416	234.970307	-2.118609	0.14785	1.03	A	740	-141	99.3
1237655498141270424	235.027343	-2.057876	0.14837	3.46	C	465	-4	99.3
1237655498141270391	235.007329	-2.058280	0.14952	4.89	A	299	295	99.3
sdss1540_291_657	234.909754	-2.021402	0.14704	1.12	A	691	-352	97.8
1237655691945836877	234.977958	-2.006994	0.15039	1.95	C	315	522	97.4
sdss1540_255_588	234.923143	-2.127417	0.15032	0.597	C	980	504	97.4
sdss1540_295_344	234.993753	-2.045437	0.15097	0.718	C	129	674	97.3
sdss1540_286_547	234.934645	-2.042969	0.15092	0.620	C	435	660	97.3
1237655498141270213	234.918780	-2.031483	0.15068	2.96	C	589	599	97.3
sdss1540_229_220	235.034895	-2.125181	0.15031	1.63	C	943	501	96.9
sdss1540_344_155	235.069055	-2.043311	0.14838	0.820	C	827	-3	96.9
sdss1540_353_185	235.074706	-2.033800	0.14797	1.23	A	882	-110	96.9
sdss1540_225_254	235.031762	-2.135590	0.15099	1.39	A	1012	679	96.7
1237655498141270961	234.990357	-2.180719	0.14938	0.515	A	1320	258	94.8
sdss1540_215_416	235.015082	-2.179881	0.15011	1.23	A	1347	449	94.7
1237655498141270464	235.048419	-2.169946	0.14783	2.13	A	1370	-146	94.6
sdss1540_232_584	234.954242	-2.186261	0.14772	0.853	A	1391	-175	94.5
sdss1540_207_459	235.024052	-2.199019	0.14998	0.947	C	1542	415	94.5
sdss1540_63_146	235.116977	-2.065781	0.14706	1.48	A	1298	-347	94.4
sdss1540_81_136	235.118408	-2.078488	0.14932	1.04	C	1338	243	94.4
1237655498141270319	234.983523	-2.196621	0.14758	7.33	A	1466	-211	94.4
sdss1540_104_156	235.123386	-2.094928	0.14859	1.23	C	1431	52	94.3
sdss1540_185_366	235.073747	-2.186265	0.14930	1.60	C	1622	238	94.3
1237655498141335925	235.061101	-2.188603	0.14667	1.58	C	1581	-450	94.1
sdss1540_210_538	235.007787	-2.215165	0.14937	1.08	C	1659	256	94.0
sdss1540_199_480	235.038729	-2.211297	0.15108	0.839	C	1693	702	93.8
sdss1540_11_300	235.095892	-2.002550	0.14777	1.27	C	1136	-162	93.8
sdss1540_45_268	235.133285	-2.031495	0.14826	1.42	A	1432	-34	90.8
1237655691945836803	234.936374	-1.957532	0.14977	3.22	A	884	360	90.3

*Table 11 continued*

**Table 11** (*continued*)

Name	RA	Dec	$z_{\text{gal}}$	$L_{\text{gal}}$	Type	$\Delta\rho$	$\Delta v$	$f_{\text{mem}}$
(1)	(2)	(3)	(4)	( $L^*$ )	(6)	(kpc)	( $\text{km s}^{-1}$ )	(%)
(1)	(2)	(3)	(4)	(5)	(6)	(7)	(8)	(9)
sdss1540_275_801	234.858856	-2.068358	0.14858	0.898	A	1175	50	88.8
sdss1540_320_685	234.958677	-1.938995	0.15069	1.03	A	975	600	86.5
sdss1540_331_546	235.007100	-1.952255	0.14585	0.620	C	864	-663	85.1
sdss1540_216_683	234.970708	-2.239341	0.14906	1.03	A	1869	175	84.0
sdss1540_187_544	235.063791	-2.234963	0.14686	0.680	C	1984	-399	83.8
sdss1540_221_549	234.981036	-2.200240	0.14568	0.898	A	1500	-707	83.0
sdss1540_246_505	234.953256	-2.143418	0.14554	0.718	C	1001	-744	82.0
sdss1540_323_204	235.046611	-2.039641	0.14549	1.18	A	616	-757	82.0
sdss1540_239_833	234.883046	-2.205204	0.14694	1.08	A	1799	-379	81.4
1237655498141270249	234.944052	-2.066769	0.14538	2.51	A	425	-785	81.4
sdss1540_212_744	234.973497	-2.261484	0.14923	1.23	A	2076	219	78.6
sdss1540_294_660	234.912858	-2.011349	0.14486	1.03	A	695	-922	65.6
1237655691409031412	235.075812	-2.269518	0.14758	2.29	A	2327	-211	64.6
1237655498141270920	234.975587	-2.090936	0.15229	1.62	C	476	1019	63.0
1237655691408965901	234.966356	-2.290281	0.14697	1.49	C	2349	-371	63.0
sdss1540_330_778	234.970222	-1.899088	0.14864	6.81	A	1331	65	61.7
sdss1540_175_679	235.098238	-2.272838	0.14922	1.08	C	2443	217	57.5
sdss1540_279_1043	234.794025	-2.043782	0.14686	1.35	A	1754	-399	57.4
sdss1540_284_1055	234.795957	-2.015644	0.14746	0.655	C	1751	-243	54.2
1237655691945902487	235.154285	-1.950655	0.14822	1.79	C	1832	-46	53.3
1237655691945836906	234.975625	-1.870832	0.14847	3.49	A	1593	20	50.5
sdss1540_140_602	235.190477	-2.211527	0.14544	1.12	C	2538	-770	43.0

NOTE—Column 6 lists the galaxy’s spectral type: “E” for emission-line galaxies, “A” for absorption-line galaxies, and “C” for composite galaxies that show both emission and absorption.  $\Delta\rho$  and  $\Delta v$  are calculated with respect to the original SDSS group centers in Table 2;  $f_{\text{mem}}$  is the percentage of the Monte Carlo trials in which a galaxy was identified as a group member.

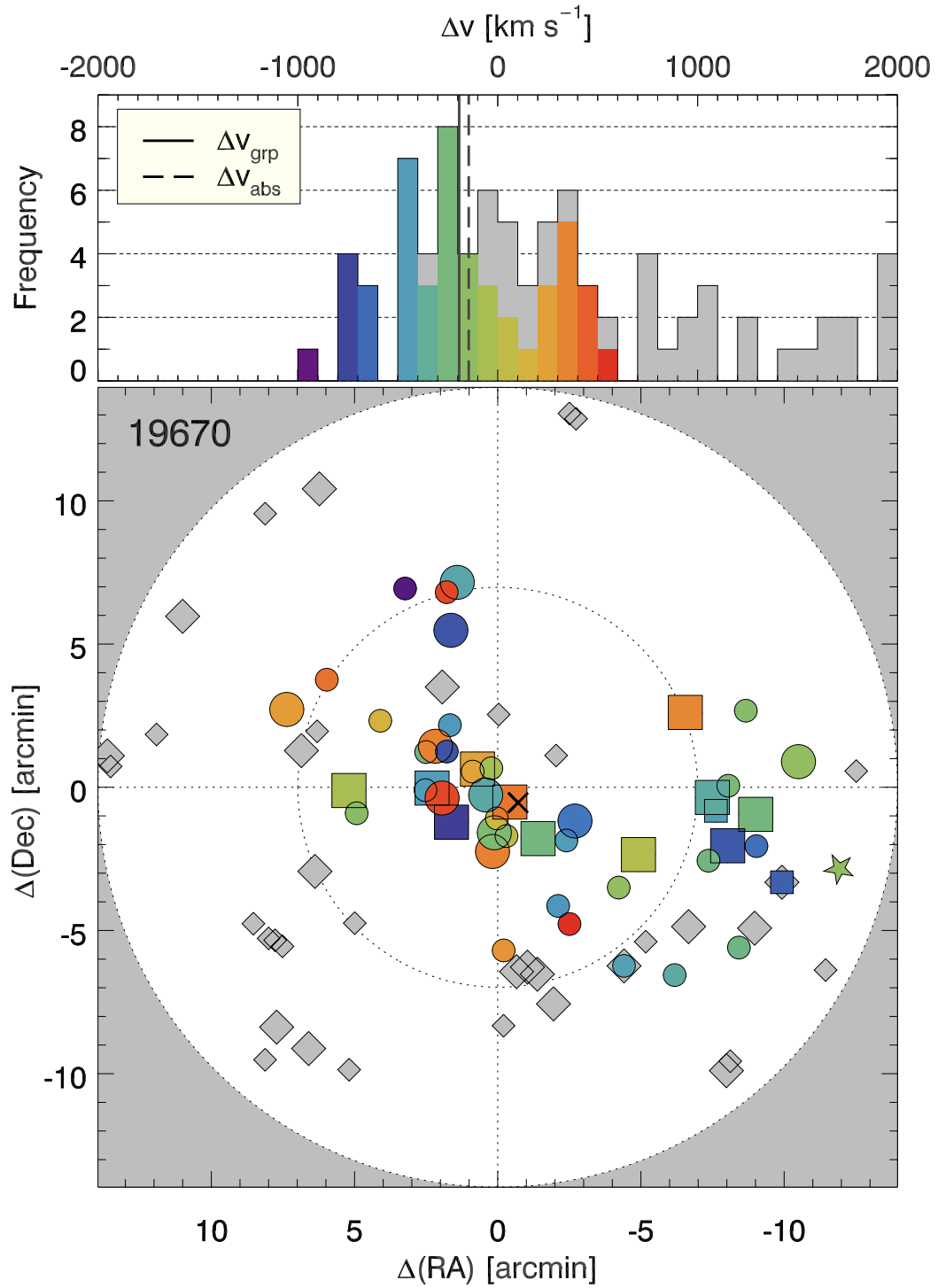


**Figure 27.** Same as Figure 4, but for the galaxy group 19670.

**Table 12.** Members of Group 19670

Name	RA	Dec	$z_{\text{gal}}$	$L_{\text{gal}}$ ( $L^*$ )	Type	$\Delta\rho$ (kpc)	$\Delta v$ ( $\text{km s}^{-1}$ )	$f_{\text{mem}}$ (%)
(1)	(2)	(3)	(4)	(5)	(6)	(7)	(8)	(9)
sbs0956_87_726	150.199427	50.767933	0.13361	2.71	A	229	-217	100.0
sbs0956_84_882	150.262799	50.792747	0.13341	0.743	C	363	-270	100.0
sbs0956_80_899	150.262213	50.814877	0.13337	0.601	C	401	-280	100.0
1237657632190627883	150.159170	50.764552	0.13344	4.70	C	328	-263	100.0
sbs0956_80_758	150.202131	50.805466	0.13421	0.408	C	101	-58	100.0
sbs0956_87_700	150.188212	50.766033	0.13455	0.312	A	249	32	100.0
sbs0956_85_725	150.197110	50.776314	0.13479	0.748	A	156	95	99.9
sbs0956_86_1018	150.326143	50.779293	0.13377	0.392	A	721	-174	99.9
1237657591924785305	150.333244	50.792518	0.13425	2.79	C	748	-47	99.9
sbs0956_83_756	150.207367	50.789936	0.13292	2.16	A	72	-399	99.8
1237657632190693462	150.256737	50.793943	0.13266	7.89	A	330	-467	99.8
sbs0956_77_869	150.240326	50.830551	0.13263	0.241	A	394	-476	99.8
sbs0956_87_574	150.133066	50.763420	0.13269	0.820	A	437	-460	99.8
sbs0956_95_594	150.140662	50.725380	0.13257	0.709	C	669	-492	99.6
sbs0956_79_1010	150.304384	50.833103	0.13501	0.471	A	678	153	99.6
1237657632190627974	150.066734	50.755232	0.13439	2.76	A	784	-10	99.4
sbs0956_94_463	150.084887	50.736034	0.13390	0.356	C	790	-140	99.4
1237657632190628054	150.214934	50.805015	0.13534	5.01	A	137	241	99.3
sbs0956_84_562	150.125141	50.774754	0.13210	1.35	C	424	-616	98.5
sbs0956_89_727a	150.201058	50.757042	0.13579	1.62	C	324	359	98.1
sbs0956_80_884	150.253615	50.818294	0.13579	1.03	A	375	359	98.1
sbs0956_99_724	150.190830	50.699467	0.13556	0.195	C	821	299	98.0
1237657632190628024	150.185143	50.785804	0.13587	1.60	C	96	382	98.0
sbs0956_80_858	150.243130	50.815186	0.13171	0.931	C	312	-719	97.0
sbs0956_69_954	150.239396	50.885742	0.13173	1.26	C	823	-714	96.9
1237657591924719897	150.238861	50.774098	0.13150	1.31	A	291	-775	96.7
sbs0956_106_495	150.080023	50.690456	0.13277	0.988	C	1100	-439	96.6
1237657632190627956	149.998672	50.788504	0.13300	2.97	A	1080	-377	96.5
1237657632190562635	149.995411	50.780697	0.13269	0.506	A	1103	-461	96.5
sbs0956_88_274	150.002246	50.751678	0.13338	0.820	C	1122	-277	96.5
sbs0956_77_1143	150.353637	50.857002	0.13592	0.748	A	1015	394	96.5
1237657632190627991	150.023588	50.837963	0.13570	1.76	A	1015	335	96.5
sbs0956_81_794	150.219340	50.803532	0.13604	0.820	A	149	425	96.3

*Table 12 continued*

**Table 12** (*continued*)

Name	RA	Dec	$z_{\text{gal}}$	$L_{\text{gal}}$ ( $L^*$ )	Type	$\Delta\rho$ (kpc)	$\Delta v$ ( $\text{km s}^{-1}$ )	$f_{\text{mem}}$ (%)
(1)	(2)	(3)	(4)	(5)	(6)	(7)	(8)	(9)
sbs0956_65_999	150.233502	50.913639	0.13289	1.19	C	1050	-407	95.9
sbs0956_65_290	149.984007	50.795311	0.13356	0.567	A	1159	-230	95.7
1237657632190562537	149.984572	50.760349	0.13176	1.14	A	1193	-706	95.7
sbs0956_80_1204	150.390487	50.839691	0.13543	1.18	C	1130	264	94.4
sbs0956_113_410	150.033388	50.685112	0.13301	0.446	C	1298	-375	94.0
sbs0956_84_845	150.247478	50.788151	0.13632	1.13	C	285	499	93.5
1237657632190562432	149.958823	50.778650	0.13346	1.07	A	1304	-257	93.2
sbs0956_66_1005	150.243244	50.907921	0.13630	0.376	C	1013	494	93.1
sbs0956_81_179	149.958100	50.760170	0.13204	0.225	A	1334	-632	93.0
sbs0956_44_384	149.967885	50.838970	0.13374	0.418	C	1304	-182	92.9
sbs0956_68_1081	150.281553	50.910072	0.13097	0.430	A	1102	-914	88.8
sbs0956_117_267	149.974222	50.701134	0.13334	0.261	E	1457	-288	87.6
sbs0956_98_577	150.130234	50.714848	0.13653	0.298	C	776	555	86.3
1237657632190562509	149.934622	50.739147	0.13185	0.992	A	1507	-682	85.6
sbs0956_31_240	149.919405	50.809322	0.13393	1.39	C	1517	-132	85.3

NOTE—Column 6 lists the galaxy’s spectral type: “E” for emission-line galaxies, “A” for absorption-line galaxies, and “C” for composite galaxies that show both emission and absorption.  $\Delta\rho$  and  $\Delta v$  are calculated with respect to the original SDSS group centers in Table 2;  $f_{\text{mem}}$  is the percentage of the Monte Carlo trials in which a galaxy was identified as a group member.

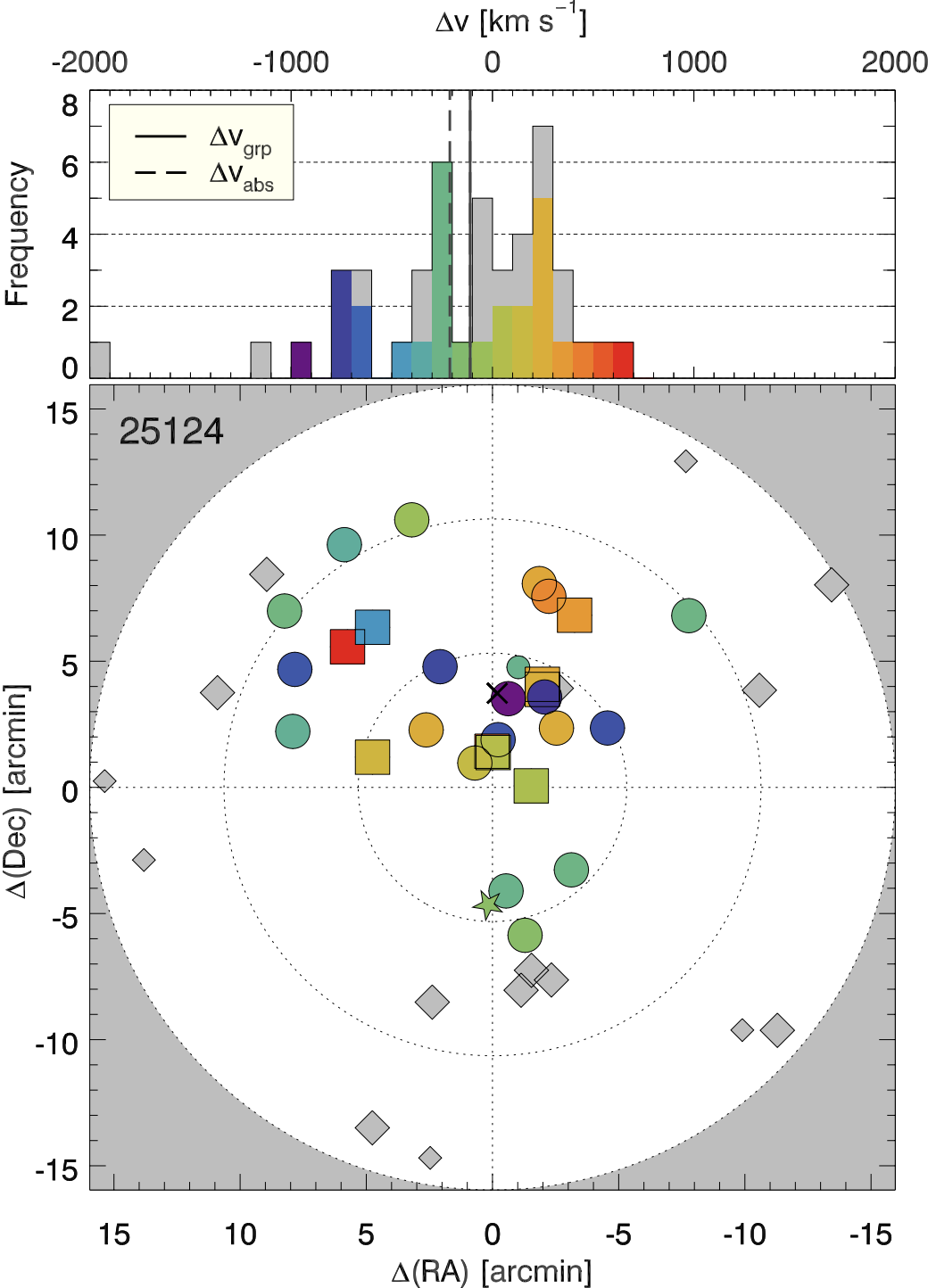


Figure 28. Same as Figure 4, but for the galaxy group 25124.

**Table 13.** Members of Group 25124

Name	RA	Dec	$z_{\text{gal}}$	$L_{\text{gal}}$ ( $L^*$ )	Type	$\Delta\rho$ (kpc)	$\Delta v$ ( $\text{km s}^{-1}$ )	$f_{\text{mem}}$ (%)
(1)	(2)	(3)	(4)	(5)	(6)	(7)	(8)	(9)
1237662619189838119	243.512392	26.625859	0.18623	3.71	A	290	26	99.1
b1612_6_338	243.554077	26.640946	0.18664	1.84	C	224	129	99.1
1237662619189837900	243.540465	26.647870	0.18640	2.21	C	260	69	99.1
b1612_337_450	243.493767	26.664057	0.18719	2.84	A	651	268	99.1
1237662619189837901	243.541445	26.648761	0.18812	5.51	A	270	504	99.0
1237662619189837844	243.504132	26.692949	0.18728	8.19	C	855	290	99.0
1237662619189837842	243.504250	26.689543	0.18710	1.12	A	820	244	99.0
b1612_22_441	243.590040	26.662842	0.18718	1.24	C	655	265	98.8
b1612_352_569	243.521948	26.704216	0.18505	0.929	C	917	-273	95.8
1237662619189772711	243.480377	26.738583	0.18754	2.80	A	1424	356	95.5
b1612_348_747	243.499432	26.751102	0.18777	1.41	C	1487	415	95.4
b1612_350_773	243.506441	26.759483	0.18729	1.84	A	1561	293	95.4
1237662619189838244	243.629655	26.644804	0.18688	3.15	A	923	190	87.9
b1612_291_214	243.482752	26.570368	0.18516	1.86	C	852	-245	87.9
b1612_305_53	243.531018	26.556435	0.18507	1.84	C	780	-268	87.1
1237662640658841658	243.629601	26.730657	0.18426	16.6	A	1493	-472	86.9
1237662640658841941	243.648112	26.717774	0.18874	3.70	A	1507	660	83.9
b1612_323_836	243.396006	26.738296	0.18516	1.34	C	1946	-245	81.4
b1612_13_577	243.579798	26.704605	0.18323	1.72	A	983	-733	81.2
b1612_357_393	243.536882	26.656389	0.18337	1.02	C	359	-698	81.2
b1612_323_507	243.456087	26.664093	0.18334	1.02	C	966	-705	81.2
b1612_344_511	243.502522	26.684589	0.18303	1.53	A	779	-784	81.0
b1612_13_933	243.600655	26.801601	0.18594	1.34	C	2086	-48	76.6
b1612_43_724	243.687057	26.702814	0.18340	1.53	A	1718	-690	74.3
b1612_52_620	243.688545	26.661825	0.18495	1.96	A	1547	-298	74.2
b1612_25_921	243.650465	26.785215	0.18483	2.36	A	2122	-329	73.3
b1612_354_492	243.529358	26.683470	0.18231	1.49	A	673	-966	72.0
b1612_38_849	243.694668	26.741384	0.18524	1.06	C	2035	-225	70.4
b1612_234_114	243.516970	26.527134	0.18564	1.79	A	1131	-124	60.2

NOTE—Column 6 lists the galaxy’s spectral type: “E” for emission-line galaxies, “A” for absorption-line galaxies, and “C” for composite galaxies that show both emission and absorption.  $\Delta\rho$  and  $\Delta v$  are calculated with respect to the original SDSS group centers in Table 2;  $f_{\text{mem}}$  is the percentage of the Monte Carlo trials in which a galaxy was identified as a group member.

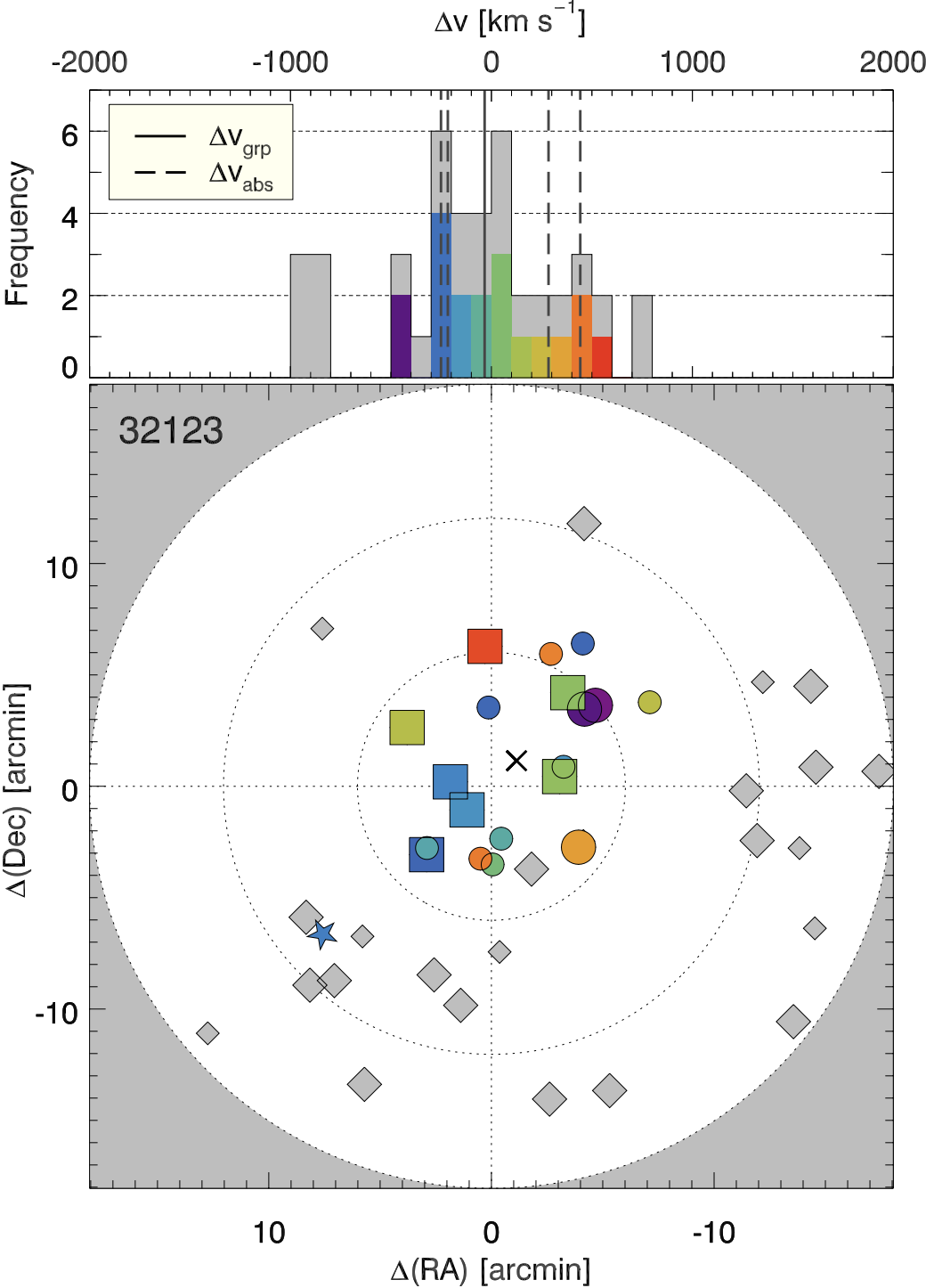


Figure 29. Same as Figure 4, but for the galaxy group 32123.

**Table 14.** Members of Group 32123

Name	RA	Dec	$z_{\text{gal}}$	$L_{\text{gal}}$ ( $L^*$ )	Type	$\Delta\rho$ (kpc)	$\Delta v$ ( $\text{km s}^{-1}$ )	$f_{\text{mem}}$ (%)
(1)	(2)	(3)	(4)	(5)	(6)	(7)	(8)	(9)
sdss1333_291_546	203.063049	45.373932	0.15941	0.628	C	398	-78	99.3
1237661360761471098	203.099533	45.395529	0.15906	2.54	A	253	-169	99.3
1237661433777029221	203.117247	45.416476	0.15892	2.83	C	308	-203	99.2
sdss1333_287_495	203.072233	45.354637	0.15978	0.968	A	584	18	98.4
1237661433776963784	203.000758	45.420384	0.16007	4.51	C	515	94	97.9
sdss1333_296_790	202.996616	45.427727	0.15909	0.516	C	558	-160	97.9
sdss1333_301_364	203.142242	45.366959	0.15934	0.712	A	667	-96	97.2
1237661360761471128	203.142678	45.361986	0.15867	2.27	C	704	-269	97.2
sdss1333_314_756	203.076610	45.472092	0.15869	0.887	C	589	-264	97.0
sdss1333_284_729	202.980652	45.367565	0.16112	1.45	A	794	365	95.2
1237661433777029234	203.163416	45.457117	0.16045	4.45	A	767	191	95.2
1237661433776963767	202.992082	45.483172	0.16002	3.52	A	902	81	94.2
sdss1333_302_930	202.974272	45.470879	0.15798	1.00	C	903	-447	94.1
sdss1333_301_959	202.962570	45.473698	0.15782	1.06	C	984	-489	93.6
sdss1333_289_471	203.085251	45.358959	0.16142	0.856	A	547	442	92.0
sdss1333_311_973	203.010006	45.512176	0.16137	0.650	A	1084	429	89.9
1237661433776963797	203.080373	45.517850	0.16174	2.03	C	1046	524	87.6
sdss1333_309_1050	202.976060	45.519962	0.15868	0.695	A	1265	-266	87.2
sdss1333_297_1080	202.904677	45.476009	0.16051	0.896	C	1338	207	85.6

NOTE—Column 6 lists the galaxy’s spectral type: “E” for emission-line galaxies, “A” for absorption-line galaxies, and “C” for composite galaxies that show both emission and absorption.  $\Delta\rho$  and  $\Delta v$  are calculated with respect to the original SDSS group centers in Table 2;  $f_{\text{mem}}$  is the percentage of the Monte Carlo trials in which a galaxy was identified as a group member.

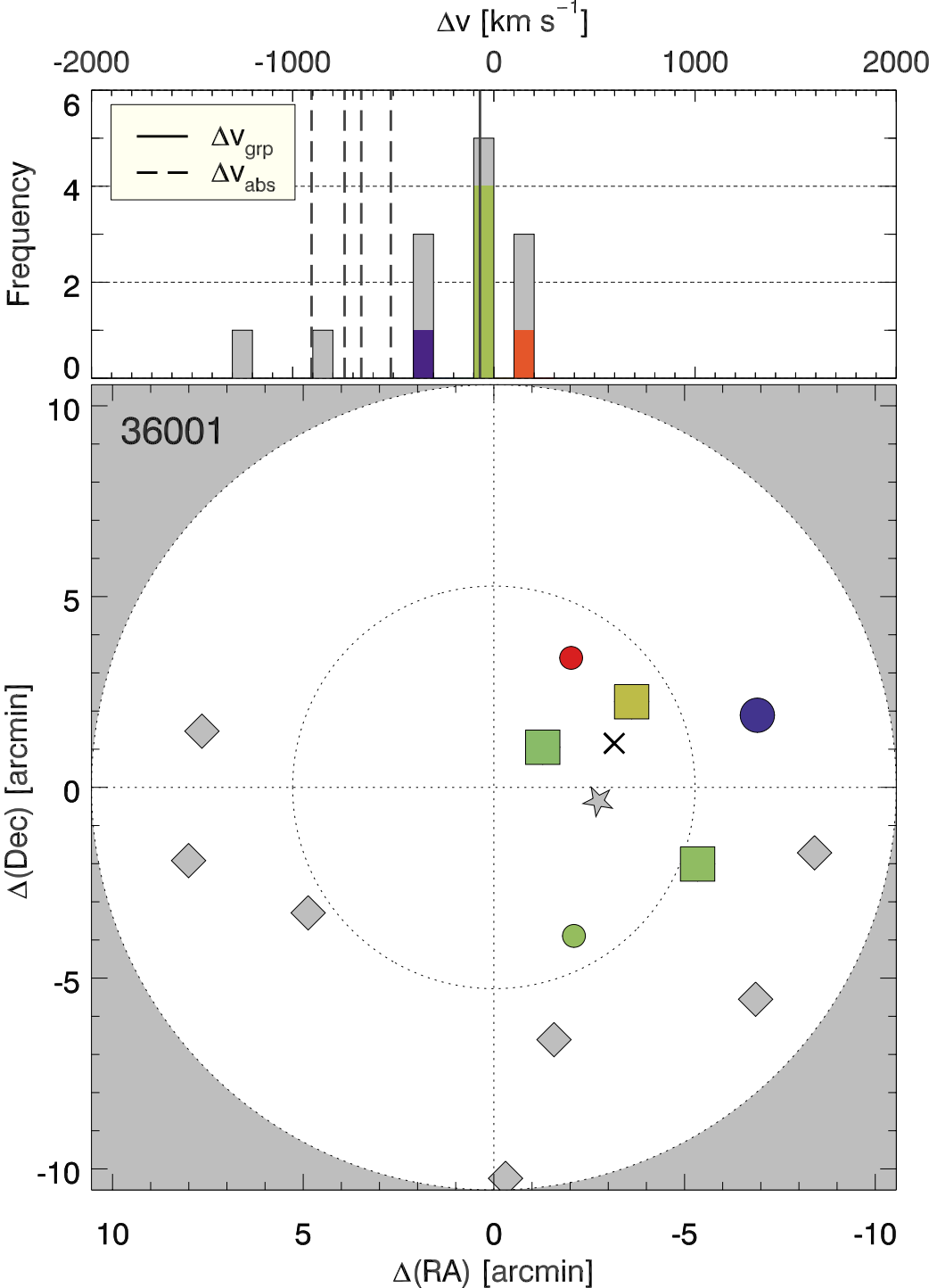


Figure 30. Same as Figure 4, but for the galaxy group 36001.

**Table 15.** Members of Group 36001

Name	RA	Dec	$z_{\text{gal}}$	$L_{\text{gal}}$ ( $L^*$ )	Type	$\Delta\rho$ (kpc)	$\Delta v$ ( $\text{km s}^{-1}$ )	$f_{\text{mem}}$ (%)
(1)	(2)	(3)	(4)	(5)	(6)	(7)	(8)	(9)
1237667549268148342	157.086777	21.355513	0.18752	4.69	C	315	-92	92.8
sdss1028_12_229	157.073436	21.394539	0.18867	0.678	E	750	199	89.4
1237667549268082878	157.045047	21.375382	0.18783	8.49	A	807	-12	89.2
1237667536399564944	157.014096	21.304513	0.18756	3.29	A	1083	-80	85.9
sdss1028_297_284	156.986060	21.369490	0.18658	2.01	C	1359	-328	82.6
sdss1028_169_215	157.072120	21.273083	0.18759	0.816	C	839	-73	79.7

NOTE—Column 6 lists the galaxy’s spectral type: “E” for emission-line galaxies, “A” for absorption-line galaxies, and “C” for composite galaxies that show both emission and absorption.  $\Delta\rho$  and  $\Delta v$  are calculated with respect to the original SDSS group centers in Table 2;  $f_{\text{mem}}$  is the percentage of the Monte Carlo trials in which a galaxy was identified as a group member.

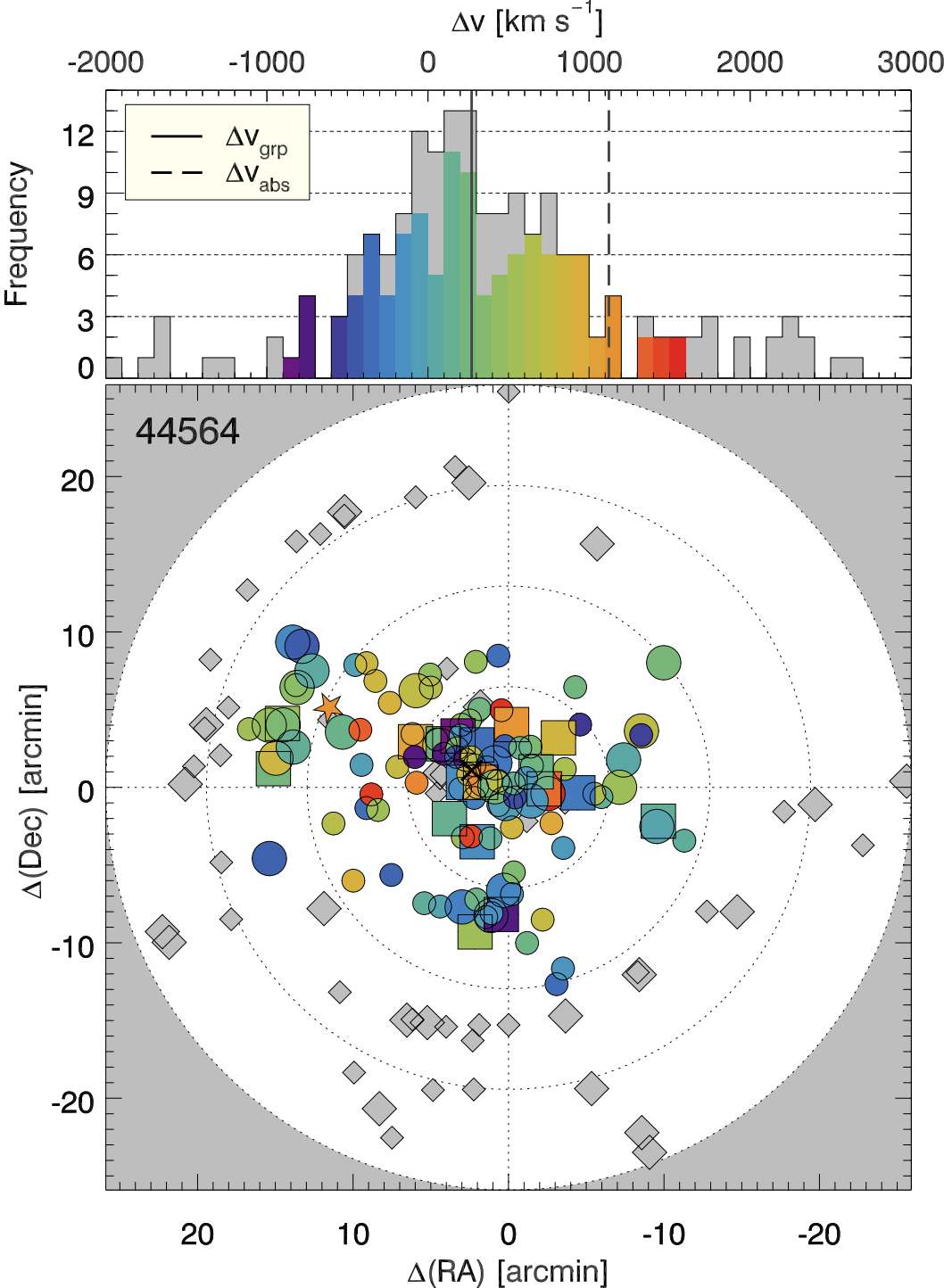


Figure 31. Same as Figure 4, but for the galaxy group 44564.

**Table 16.** Members of Group 44564

Name	RA	Dec	$z_{\text{gal}}$	$L_{\text{gal}}$ ( $L^*$ )	Type	$\Delta\rho$ (kpc)	$\Delta v$ ( $\text{km s}^{-1}$ )	$f_{\text{mem}}$ (%)
(1)	(2)	(3)	(4)	(5)	(6)	(7)	(8)	(9)
cso1022_252_769	208.113456	36.265675	0.14554	0.399	A	65	126	100.0
cso1022_249_708	208.138490	36.262070	0.14610	9.66	A	134	272	100.0
cso1022_247_774	208.124285	36.244125	0.14490	1.46	A	162	-42	100.0
cso1022_254_807	208.096947	36.271324	0.14479	0.493	A	197	-71	100.0
cso1022_246_753	208.133912	36.242416	0.14443	0.327	C	202	-165	100.0
cso1022_250_858	208.090482	36.246872	0.14467	1.06	A	260	-102	100.0
cso1022_262_790	208.091225	36.305073	0.14620	0.311	A	457	298	100.0
1237662685753311429	208.083703	36.278130	0.14589	3.30	A	313	218	100.0
cso1022_257_813	208.089252	36.284828	0.14511	0.283	A	316	13	100.0
cso1022_261_752	208.104901	36.303677	0.14573	0.364	A	406	175	100.0
cso1022_244_659	208.166142	36.250111	0.14411	0.733	A	355	-249	100.0
1237662685753376963	208.180283	36.266770	0.14440	1.69	A	447	-172	100.0
1237662685753376967	208.162092	36.203144	0.14443	3.66	A	620	-165	100.0
cso1022_256_518	208.188500	36.303368	0.14635	0.332	A	636	338	100.0
1237662685753376995	208.199025	36.227883	0.14562	1.63	A	661	146	100.0
cso1022_261_518	208.184152	36.316959	0.14476	0.283	A	697	-79	100.0
cso1022_266_544	208.171720	36.333157	0.14634	0.882	A	763	335	100.0
1237664854715072690	208.206989	36.308085	0.14595	10.3	A	773	232	100.0
cso1022_237_801	208.144398	36.206817	0.14549	0.833	A	534	113	100.0
cso1022_270_579	208.158975	36.345352	0.14596	0.479	A	824	236	100.0
cso1022_255_673	208.138575	36.287804	0.14390	1.40	A	278	-304	99.9
1237664854715072648	208.162762	36.307017	0.14380	2.25	C	525	-330	99.9
1237662685753311408	208.028163	36.255575	0.14399	3.01	A	687	-280	99.7
cso1022_260_693	208.125243	36.305706	0.14356	0.303	A	409	-393	99.6
cso1022_253_525	208.189902	36.294155	0.14344	0.243	C	598	-424	99.3
cso1022_232_719	208.181176	36.207748	0.14693	0.332	A	669	490	99.0
cso1022_235_955	208.113356	36.170322	0.14629	0.295	E	841	322	98.8
cso1022_245_1053	208.047609	36.196464	0.14475	0.236	A	807	-81	98.8
cso1022_249_796	208.111811	36.250652	0.14326	0.236	C	118	-471	97.8
cso1022_256_1105	207.996897	36.250961	0.14556	0.600	C	923	131	97.1
cso1022_265_514	208.182921	36.328602	0.14738	0.668	A	773	607	95.9
cso1022_259_938	208.045650	36.281216	0.14735	0.332	A	584	600	95.9
cso1022_230_975	208.126888	36.151024	0.14427	1.10	A	1018	-207	95.9

*Table 16 continued*

Table 16 (continued)

Name	RA	Dec	$z_{\text{gal}}$	$L_{\text{gal}}$	Type	$\Delta\rho$	$\Delta v$	$f_{\text{mem}}$
(1)	(2)	(3)	(4)	( $L^*$ ) (5)	(6)	(kpc) (7)	( $\text{km s}^{-1}$ ) (8)	(%) (9)
cso1022_256_1075	208.006267	36.254601	0.14744	0.966	A	850	623	95.8
cso1022_247_648	208.162150	36.261677	0.14306	0.221	A	310	-524	95.3
cso1022_251_710	208.134227	36.268360	0.14768	0.230	A	121	686	95.2
cso1022_253_602	208.165812	36.285011	0.14765	0.385	A	401	678	95.2
cso1022_279_399	208.223705	36.368343	0.14755	0.507	A	1248	652	95.1
cso1022_231_1008	208.115830	36.146946	0.14483	0.431	C	1055	-60	94.8
cso1022_255_581	208.169818	36.293491	0.14794	0.781	A	471	754	94.6
cso1022_235_348	208.268323	36.283421	0.14794	0.482	A	1117	754	94.6
cso1022_249_594	208.174067	36.275593	0.14799	0.482	A	419	767	94.6
cso1022_279_341	208.243303	36.365154	0.14784	1.16	A	1321	728	94.6
cso1022_285_591	208.163924	36.396053	0.14686	0.668	A	1281	471	94.6
cso1022_285_409	208.224664	36.382423	0.14675	0.446	E	1357	442	94.5
cso1022_211_438	208.293915	36.237144	0.14704	0.918	A	1308	518	94.4
cso1022_284_681	208.133984	36.402626	0.14382	0.393	C	1304	-325	94.3
cso1022_274_951	208.031774	36.368881	0.14597	0.507	A	1188	238	93.7
cso1022_224_933	208.163352	36.141197	0.14577	0.230	C	1152	186	93.2
cso1022_205_413	208.309393	36.239227	0.14382	0.269	E	1418	-325	93.1
cso1022_215_254	208.315859	36.285557	0.14489	0.479	C	1468	-45	93.0
cso1022_243_843	208.115859	36.218498	0.14829	0.230	A	397	846	92.5
1237664854715007115	208.054066	36.314504	0.14833	1.73	A	694	855	92.4
cso1022_267_969	208.025222	36.328747	0.14284	0.431	C	940	-581	91.8
cso1022_274_234	208.278251	36.352047	0.14847	0.226	C	1438	893	91.2
cso1022_258_1161	207.972822	36.261536	0.14706	1.45	C	1096	524	91.1
cso1022_220_925	208.182077	36.133156	0.14415	1.40	C	1267	-238	90.8
cso1022_256_337	208.248067	36.318649	0.14852	0.320	A	1084	906	90.8
1237662685753376885	208.157511	36.266795	0.14855	1.83	A	280	913	90.8
cso1022_257_431	208.216181	36.312786	0.14862	0.230	A	854	932	90.7
cso1022_205_689	208.276191	36.167522	0.14361	0.707	C	1445	-380	90.7
cso1022_225_1011	208.142982	36.126495	0.14449	0.332	C	1254	-149	90.6
cso1022_215_879	208.211446	36.133663	0.14507	0.931	C	1357	3	90.6
cso1022_224_1017	208.143682	36.124035	0.14493	2.43	C	1277	-34	90.6
cso1022_223_1011	208.150077	36.122284	0.14612	0.577	A	1300	278	90.6
cso1022_212_839	208.232489	36.137222	0.14545	0.833	A	1415	102	90.6
cso1022_255_450	208.211760	36.306549	0.14868	1.72	C	795	948	90.5
cso1022_262_1153	207.967486	36.290798	0.14521	1.20	A	1167	39	90.2

Table 16 continued

**Table 16** (*continued*)

Name	RA	Dec	$z_{\text{gal}}$	$L_{\text{gal}}$	Type	$\Delta\rho$	$\Delta v$	$f_{\text{mem}}$
(1)	(2)	(3)	(4)	( $L^*$ ) (5)	(6)	(kpc) (7)	( $\text{km s}^{-1}$ ) (8)	(%) (9)
cso1022_295_205	208.297391	36.375523	0.14820	0.290	C	1682	822	88.8
cso1022_214_107	208.341165	36.320690	0.14576	1.40	A	1727	183	88.6
cso1022_248_966	208.063388	36.223057	0.14884	0.393	C	552	990	88.1
cso1022_244_594	208.184752	36.259785	0.14889	0.438	A	478	1003	87.7
1237664854715072734	208.244140	36.310442	0.14895	1.75	A	1024	1020	87.3
1237662685753376999	208.164863	36.106427	0.14708	1.64	A	1465	528	86.2
cso1022_232_1161	208.075047	36.119587	0.14803	0.966	A	1349	778	86.2
cso1022_183_448	208.353124	36.222717	0.14763	0.410	C	1765	673	86.1
cso1022_253_650	208.149190	36.282814	0.14934	0.609	A	291	1121	81.8
1237664854715072601	208.116342	36.328792	0.14932	2.74	A	621	1115	81.8
cso1022_190_674	208.326745	36.161411	0.14857	0.588	C	1789	919	81.7
cso1022_314_223	208.309107	36.394661	0.14818	0.913	C	1862	817	81.7
cso1022_250_663	208.151422	36.269134	0.14947	2.66	A	241	1155	81.7
cso1022_236_445	208.242660	36.266365	0.14960	0.540	C	909	1189	80.5
cso1022_266_1207	207.944040	36.317524	0.14300	0.332	A	1408	-539	80.4
cso1022_323_192	208.324156	36.392666	0.14498	0.850	C	1936	-21	80.3
cso1022_267_1207	207.943711	36.321941	0.14782	1.32	A	1425	723	79.8
cso1022_227_1187	208.095803	36.094528	0.14585	0.276	A	1548	207	78.9
1237662685753311352	207.921161	36.225136	0.14544	1.56	A	1518	100	70.6
cso1022_254_1344	207.923212	36.219505	0.14510	1.53	C	1515	10	70.6
1237662685753376945	208.129929	36.125105	0.14220	2.10	A	1258	-748	67.2
cso1022_132_206	208.406553	36.304672	0.14551	1.30	C	2161	118	67.2
cso1022_252_476	208.206453	36.297382	0.14216	0.383	C	720	-759	67.1
cso1022_245_381	208.245005	36.293961	0.14210	0.385	C	972	-775	66.3
cso1022_253_562	208.177843	36.291058	0.14201	0.399	A	506	-799	64.7
1237662685753311426	208.072897	36.259851	0.15006	1.65	C	353	1309	62.2
cso1022_31_155	208.381662	36.386307	0.14533	1.60	C	2254	71	62.0
cso1022_64_145	208.401475	36.368553	0.14659	2.31	C	2308	401	60.1
cso1022_107_190	208.420229	36.328415	0.14626	4.40	A	2310	314	60.1
1237664854715138119	208.420948	36.330000	0.14698	4.11	E	2319	502	60.1
cso1022_241_147	208.317404	36.323219	0.15026	0.393	C	1569	1361	60.1
cso1022_62_154	208.402934	36.371037	0.14703	0.479	A	2327	516	60.1
1237664854715138234	208.433051	36.281447	0.14606	1.83	C	2329	262	60.1
cso1022_128_283	208.429670	36.292713	0.14819	1.45	C	2314	819	60.1
1237664854715072678	208.187569	36.316579	0.14175	2.80	C	712	-866	60.1

*Table 16 continued*

**Table 16** (*continued*)

Name	RA	Dec	$z_{\text{gal}}$	$L_{\text{gal}}$ ( $L^*$ )	Type	$\Delta\rho$ (kpc)	$\Delta v$ ( $\text{km s}^{-1}$ )	$f_{\text{mem}}$ (%)
(1)	(2)	(3)	(4)	(5)	(6)	(7)	(8)	(9)
cso1022_104_240	208.438511	36.328083	0.14687	1.16	A	2440	474	60.1
cso1022_29_258	208.394952	36.412701	0.14344	1.32	A	2468	-424	60.1
cso1022_277_1300	207.914142	36.395043	0.14613	1.45	A	1964	280	58.1
cso1022_35_288	208.407283	36.417133	0.14432	1.63	C	2566	-194	57.7
cso1022_228_1352	208.048038	36.067234	0.14461	0.721	E	1868	-118	57.5
cso1022_154_627	208.438396	36.185101	0.14353	1.03	C	2465	-401	56.5
cso1022_254_1463	207.886691	36.204285	0.14545	0.856	A	1815	102	55.2
cso1022_234_739	208.170362	36.208736	0.15064	0.257	C	611	1461	54.2
cso1022_103_320	208.465576	36.323864	0.14714	0.226	C	2626	545	53.8
cso1022_212_372	208.302812	36.253921	0.15072	0.230	A	1356	1482	52.7
cso1022_226_1382	208.056579	36.050407	0.14372	0.962	C	2001	-351	51.8
cso1022_270_664	208.129807	36.344147	0.15084	0.856	C	765	1513	48.7
cso1022_253_906	208.067994	36.254742	0.15093	1.53	A	394	1537	46.5

NOTE—Column 6 lists the galaxy’s spectral type: “E” for emission-line galaxies, “A” for absorption-line galaxies, and “C” for composite galaxies that show both emission and absorption.  $\Delta\rho$  and  $\Delta v$  are calculated with respect to the original SDSS group centers in Table 2;  $f_{\text{mem}}$  is the percentage of the Monte Carlo trials in which a galaxy was identified as a group member.

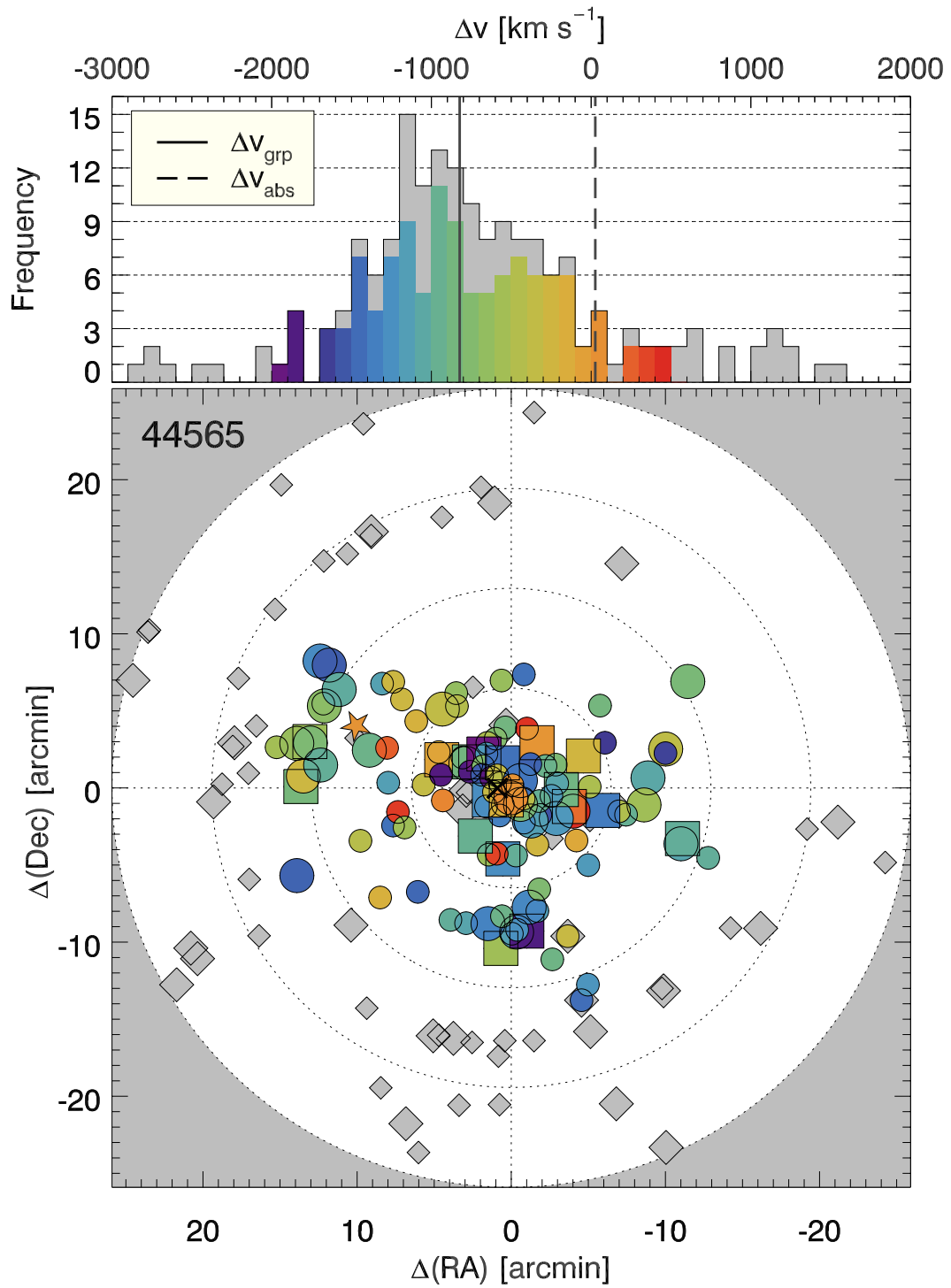


Figure 32. Same as Figure 4, but for the galaxy group 44565.

**Table 17.** Members of Group 44565

Name	RA	Dec	$z_{\text{gal}}$	$L_{\text{gal}}$ ( $L^*$ )	Type	$\Delta\rho$ (kpc)	$\Delta v$ ( $\text{km s}^{-1}$ )	$f_{\text{mem}}$ (%)
(1)	(2)	(3)	(4)	(5)	(6)	(7)	(8)	(9)
cso1022_253_602	208.165812	36.285011	0.14765	0.387	A	124	-417	100.0
cso1022_251_710	208.134227	36.268360	0.14768	0.231	A	167	-410	100.0
cso1022_249_594	208.174067	36.275593	0.14799	0.488	A	181	-329	100.0
cso1022_255_581	208.169818	36.293491	0.14794	0.783	A	193	-342	100.0
1237662685753376885	208.157511	36.266795	0.14855	1.85	A	133	-184	100.0
cso1022_255_450	208.211760	36.306549	0.14868	1.71	C	527	-149	99.8
cso1022_257_431	208.216181	36.312786	0.14862	0.231	A	586	-164	99.8
cso1022_265_514	208.182921	36.328602	0.14738	0.674	A	520	-488	99.8
cso1022_256_337	208.248067	36.318649	0.14852	0.323	A	825	-190	99.7
cso1022_235_348	208.268323	36.283421	0.14794	0.488	A	894	-342	99.4
cso1022_244_594	208.184752	36.259785	0.14889	0.439	A	320	-94	99.4
1237664854715072734	208.244140	36.310442	0.14895	1.77	A	766	-77	99.2
cso1022_232_719	208.181176	36.207748	0.14693	0.333	A	718	-605	97.4
cso1022_279_399	208.223705	36.368343	0.14755	0.512	A	1002	-443	96.1
cso1022_279_341	208.243303	36.365154	0.14784	1.17	A	1068	-368	95.8
cso1022_243_843	208.115859	36.218498	0.14829	0.231	A	637	-250	95.0
cso1022_285_409	208.224664	36.382423	0.14675	0.445	E	1118	-652	94.9
cso1022_274_234	208.278251	36.352047	0.14847	0.226	C	1184	-203	94.9
cso1022_253_650	208.149190	36.282814	0.14934	0.615	A	30	23	94.3
cso1022_256_518	208.188500	36.303368	0.14635	0.333	A	362	-757	94.2
cso1022_266_544	208.171720	36.333157	0.14634	0.888	A	527	-759	94.2
1237664854715072601	208.116342	36.328792	0.14932	2.76	A	531	18	94.1
cso1022_285_591	208.163924	36.396053	0.14686	0.674	A	1100	-623	93.9
cso1022_262_790	208.091225	36.305073	0.14620	0.312	A	512	-796	93.8
cso1022_249_708	208.138490	36.262070	0.14610	9.74	A	192	-822	93.7
cso1022_270_579	208.158975	36.345352	0.14596	0.482	A	621	-858	93.7
1237664854715072690	208.206989	36.308085	0.14595	10.4	A	503	-862	93.7
1237662685753311429	208.083703	36.278130	0.14589	3.33	A	511	-875	93.7
1237664854715007115	208.054066	36.314504	0.14833	1.75	A	805	-241	93.7
cso1022_261_752	208.104901	36.303677	0.14573	0.366	A	415	-918	93.6
cso1022_211_438	208.293915	36.237144	0.14704	0.930	A	1161	-577	93.6
cso1022_259_938	208.045650	36.281216	0.14735	0.333	A	800	-496	93.5
1237662685753376995	208.199025	36.227883	0.14562	1.65	A	612	-947	93.5

*Table 17 continued*

**Table 17** (*continued*)

Name	RA	Dec	$z_{\text{gal}}$	$L_{\text{gal}}$	Type	$\Delta\rho$	$\Delta v$	$f_{\text{mem}}$
(1)	(2)	(3)	(4)	( $L^*$ )	(6)	(kpc)	( $\text{km s}^{-1}$ )	(%)
(1)	(2)	(3)	(4)	(5)	(6)	(7)	(8)	(9)
cso1022_252_769	208.113456	36.265675	0.14554	0.401	A	314	-968	93.5
cso1022_237_801	208.144398	36.206817	0.14549	0.837	A	691	-981	93.5
cso1022_250_663	208.151422	36.269134	0.14947	2.68	A	101	57	92.9
cso1022_248_966	208.063388	36.223057	0.14884	0.392	C	854	-107	92.8
cso1022_257_813	208.089252	36.284828	0.14511	0.284	A	471	-1080	92.0
cso1022_235_955	208.113356	36.170322	0.14629	0.295	E	1072	-772	91.9
cso1022_256_1075	208.006267	36.254601	0.14744	0.974	A	1125	-472	91.4
cso1022_254_807	208.096947	36.271324	0.14479	0.494	A	418	-1163	91.3
cso1022_247_774	208.124285	36.244125	0.14490	1.47	A	393	-1135	91.3
cso1022_261_518	208.184152	36.316959	0.14476	0.284	A	432	-1171	91.3
cso1022_250_858	208.090482	36.246872	0.14467	1.07	A	555	-1195	91.3
cso1022_215_254	208.315859	36.285557	0.14489	0.482	C	1256	-1137	91.3
cso1022_245_1053	208.047609	36.196464	0.14475	0.237	A	1112	-1174	91.3
1237662685753376963	208.180283	36.266770	0.14440	1.71	A	256	-1265	91.2
cso1022_246_753	208.133912	36.242416	0.14443	0.326	C	376	-1257	91.2
1237662685753376967	208.162092	36.203144	0.14443	3.68	A	729	-1258	91.2
cso1022_274_951	208.031774	36.368881	0.14597	0.512	A	1234	-856	91.2
cso1022_244_659	208.166142	36.250111	0.14411	0.739	A	304	-1341	91.2
cso1022_256_1105	207.996897	36.250961	0.14556	0.599	C	1202	-963	91.2
1237662685753311408	208.028163	36.255575	0.14399	3.03	A	961	-1372	91.2
cso1022_230_975	208.126888	36.151024	0.14427	1.10	A	1229	-1299	91.2
cso1022_255_673	208.138575	36.287804	0.14390	1.41	A	120	-1396	91.2
1237664854715072648	208.162762	36.307017	0.14380	2.26	C	272	-1422	91.2
cso1022_260_693	208.125243	36.305706	0.14356	0.304	A	312	-1484	91.2
cso1022_284_681	208.133984	36.402626	0.14382	0.392	C	1165	-1417	91.1
cso1022_205_413	208.309393	36.239227	0.14382	0.268	E	1266	-1417	91.1
cso1022_236_445	208.242660	36.266365	0.14960	0.541	C	710	91	91.1
cso1022_231_1008	208.115830	36.146946	0.14483	0.430	C	1282	-1153	91.1
cso1022_224_933	208.163352	36.141197	0.14577	0.231	C	1312	-908	91.1
cso1022_253_525	208.189902	36.294155	0.14344	0.244	C	326	-1516	90.7
cso1022_220_925	208.182077	36.133156	0.14415	1.41	C	1404	-1330	90.5
cso1022_205_689	208.276191	36.167522	0.14361	0.705	C	1426	-1471	90.5
cso1022_258_1161	207.972822	36.261536	0.14706	1.46	C	1365	-571	90.4
cso1022_249_796	208.111811	36.250652	0.14326	0.237	C	405	-1563	90.4
cso1022_215_879	208.211446	36.133663	0.14507	0.930	C	1454	-1090	90.3

*Table 17 continued*

Table 17 (continued)

Name	RA	Dec	$z_{\text{gal}}$	$L_{\text{gal}}$	Type	$\Delta\rho$	$\Delta v$	$f_{\text{mem}}$
(1)	(2)	(3)	(4)	( $L^*$ )	(6)	(kpc)	( $\text{km s}^{-1}$ )	(%)
(1)	(2)	(3)	(4)	(5)	(6)	(7)	(8)	(9)
cso1022_224_1017	208.143682	36.124035	0.14493	2.45	C	1471	-1127	90.3
cso1022_225_1011	208.142982	36.126495	0.14449	0.333	C	1448	-1242	90.3
cso1022_223_1011	208.150077	36.122284	0.14612	0.579	A	1487	-817	90.3
cso1022_212_839	208.232489	36.137222	0.14545	0.837	A	1482	-991	90.3
cso1022_295_205	208.297391	36.375523	0.14820	0.290	C	1433	-274	90.3
cso1022_247_648	208.162150	36.261677	0.14306	0.223	A	192	-1615	90.1
cso1022_262_1153	207.967486	36.290798	0.14521	1.21	A	1398	-1054	89.9
cso1022_214_107	208.341165	36.320690	0.14576	1.41	A	1497	-910	89.9
cso1022_183_448	208.353124	36.222717	0.14763	0.410	C	1631	-423	87.5
1237662685753376999	208.164863	36.106427	0.14708	1.64	A	1640	-567	87.3
cso1022_232_1161	208.075047	36.119587	0.14803	0.974	A	1618	-318	87.2
cso1022_190_674	208.326745	36.161411	0.14857	0.587	C	1744	-177	84.3
cso1022_314_223	208.309107	36.394661	0.14818	0.918	C	1618	-279	83.8
cso1022_267_969	208.025222	36.328747	0.14284	0.430	C	1060	-1672	83.5
cso1022_323_192	208.324156	36.392666	0.14498	0.848	C	1693	-1114	80.8
cso1022_266_1207	207.944040	36.317524	0.14300	0.333	A	1612	-1630	80.7
cso1022_267_1207	207.943711	36.321941	0.14782	1.33	A	1624	-373	80.3
cso1022_227_1187	208.095803	36.094528	0.14585	0.278	A	1798	-887	79.2
cso1022_254_1344	207.923212	36.219505	0.14510	1.54	C	1823	-1083	72.4
1237662685753311352	207.921161	36.225136	0.14544	1.58	A	1822	-993	72.3
1237662685753311426	208.072897	36.259851	0.15006	1.67	C	622	211	69.1
cso1022_132_206	208.406553	36.304672	0.14551	1.30	C	1958	-976	67.5
cso1022_252_476	208.206453	36.297382	0.14216	0.383	C	454	-1850	65.6
1237662685753376945	208.129929	36.125105	0.14220	2.11	A	1469	-1838	65.6
cso1022_245_381	208.245005	36.293961	0.14210	0.387	C	728	-1865	65.5
cso1022_253_562	208.177843	36.291058	0.14201	0.401	A	231	-1889	63.8
cso1022_31_155	208.381662	36.386307	0.14533	1.62	C	2021	-1023	62.8
cso1022_241_147	208.317404	36.323219	0.15026	0.392	C	1331	263	61.1
1237664854715138119	208.420948	36.330000	0.14698	4.11	E	2107	-593	61.1
cso1022_62_154	208.402934	36.371037	0.14703	0.482	A	2100	-579	61.1
cso1022_107_190	208.420229	36.328415	0.14626	4.45	A	2099	-780	61.1
cso1022_64_145	208.401475	36.368553	0.14659	2.34	C	2080	-694	61.1
cso1022_128_283	208.429670	36.292713	0.14819	1.46	C	2124	-277	61.1
1237664854715138234	208.433051	36.281447	0.14606	1.83	C	2146	-832	61.1
cso1022_104_240	208.438511	36.328083	0.14687	1.17	A	2234	-621	61.0

Table 17 continued

**Table 17** (*continued*)

Name	RA	Dec	$z_{\text{gal}}$	$L_{\text{gal}}$ ( $L^*$ )	Type	$\Delta\rho$ (kpc)	$\Delta v$ ( $\text{km s}^{-1}$ )	$f_{\text{mem}}$ (%)
(1)	(2)	(3)	(4)	(5)	(6)	(7)	(8)	(9)
cso1022_29_258	208.394952	36.412701	0.14344	1.33	A	2238	-1516	60.9
1237664854715072678	208.187569	36.316579	0.14175	2.80	C	445	-1956	60.9
cso1022_277_1300	207.914142	36.395043	0.14613	1.46	A	2101	-814	58.6
cso1022_35_288	208.407283	36.417133	0.14432	1.64	C	2339	-1286	58.4
cso1022_228_1352	208.048038	36.067234	0.14461	0.721	E	2153	-1210	57.8
cso1022_154_627	208.438396	36.185101	0.14353	1.03	C	2364	-1492	56.8
cso1022_254_1463	207.886691	36.204285	0.14545	0.858	A	2132	-991	55.5
cso1022_234_739	208.170362	36.208736	0.15064	0.256	C	687	363	55.3
cso1022_103_320	208.465576	36.323864	0.14714	0.226	C	2428	-550	55.1
cso1022_212_372	208.302812	36.253921	0.15072	0.231	A	1182	383	53.4
cso1022_226_1382	208.056579	36.050407	0.14372	0.962	C	2280	-1443	52.1
cso1022_270_664	208.129807	36.344147	0.15084	0.858	C	627	415	50.3
cso1022_253_906	208.067994	36.254742	0.15093	1.54	A	673	438	48.7

NOTE—Column 6 lists the galaxy’s spectral type: “E” for emission-line galaxies, “A” for absorption-line galaxies, and “C” for composite galaxies that show both emission and absorption.  $\Delta\rho$  and  $\Delta v$  are calculated with respect to the original SDSS group centers in Table 2;  $f_{\text{mem}}$  is the percentage of the Monte Carlo trials in which a galaxy was identified as a group member.

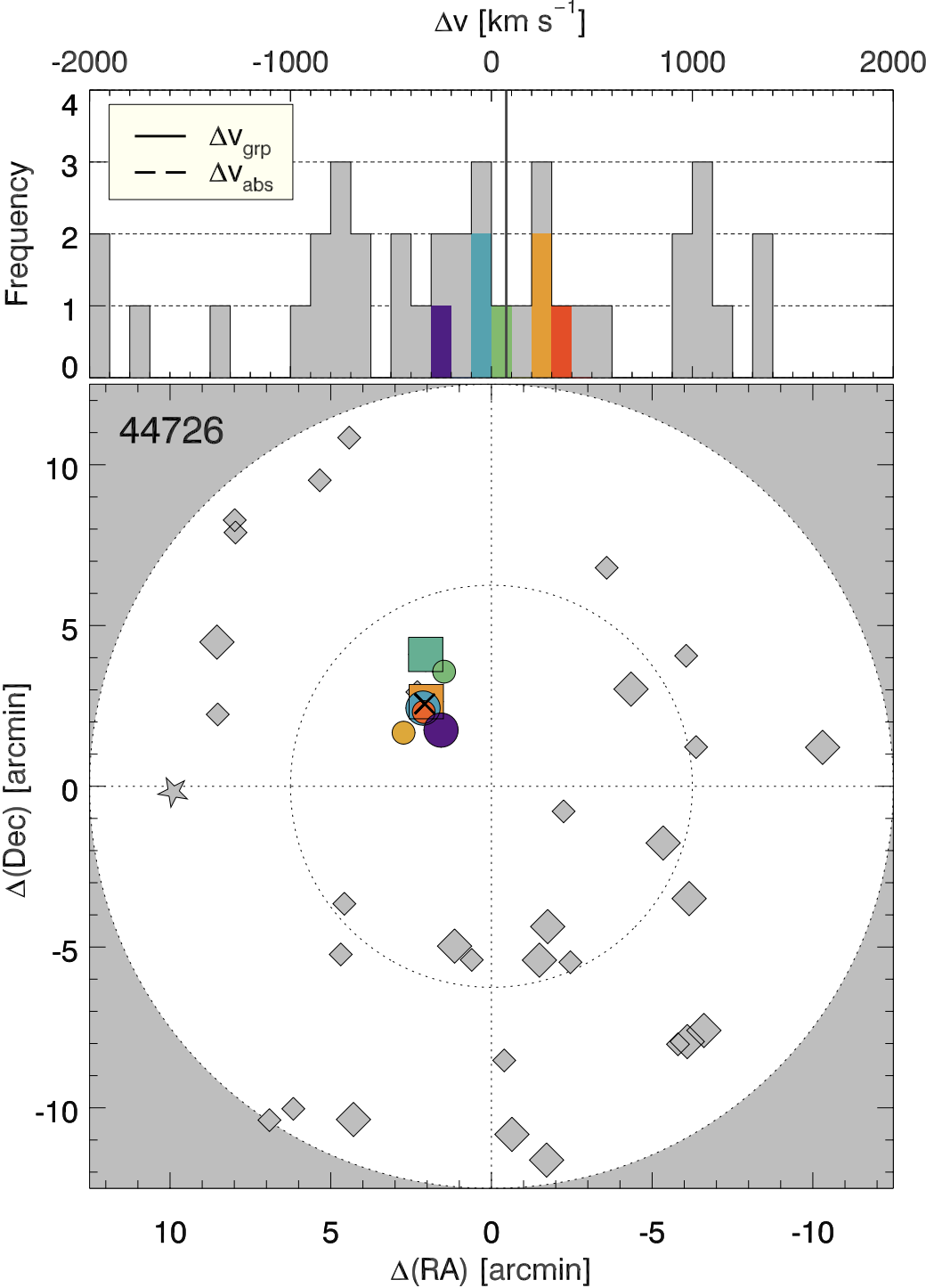


Figure 33. Same as Figure 4, but for the galaxy group 44726.

**Table 18.** Members of Group 44726

Name	RA	Dec	$z_{\text{gal}}$	$L_{\text{gal}}$ ( $L^*$ )	Type	$\Delta\rho$ (kpc)	$\Delta v$ ( $\text{km s}^{-1}$ )	$f_{\text{mem}}$ (%)
(1)	(2)	(3)	(4)	(5)	(6)	(7)	(8)	(9)
cso1080_287_491	226.215806	29.831860	0.15185	1.15	A	516	-60	85.9
cso1080_292_552	226.203217	29.850737	0.15222	0.525	C	616	36	85.8
1237664853111603254	226.214239	29.859650	0.15205	3.80	A	732	-8	85.7
cso1080_283_443	226.227436	29.819086	0.15296	0.786	C	511	229	85.6
1237664853111603398	226.213860	29.835203	0.15309	2.31	A	531	262	85.6
cso1080_286_490	226.215362	29.829822	0.15333	0.510	E	499	325	85.6
cso1080_282_512	226.205034	29.820446	0.15108	1.70	C	375	-260	83.0

NOTE—Column 6 lists the galaxy’s spectral type: “E” for emission-line galaxies, “A” for absorption-line galaxies, and “C” for composite galaxies that show both emission and absorption.  $\Delta\rho$  and  $\Delta v$  are calculated with respect to the original SDSS group centers in Table 2;  $f_{\text{mem}}$  is the percentage of the Monte Carlo trials in which a galaxy was identified as a group member.

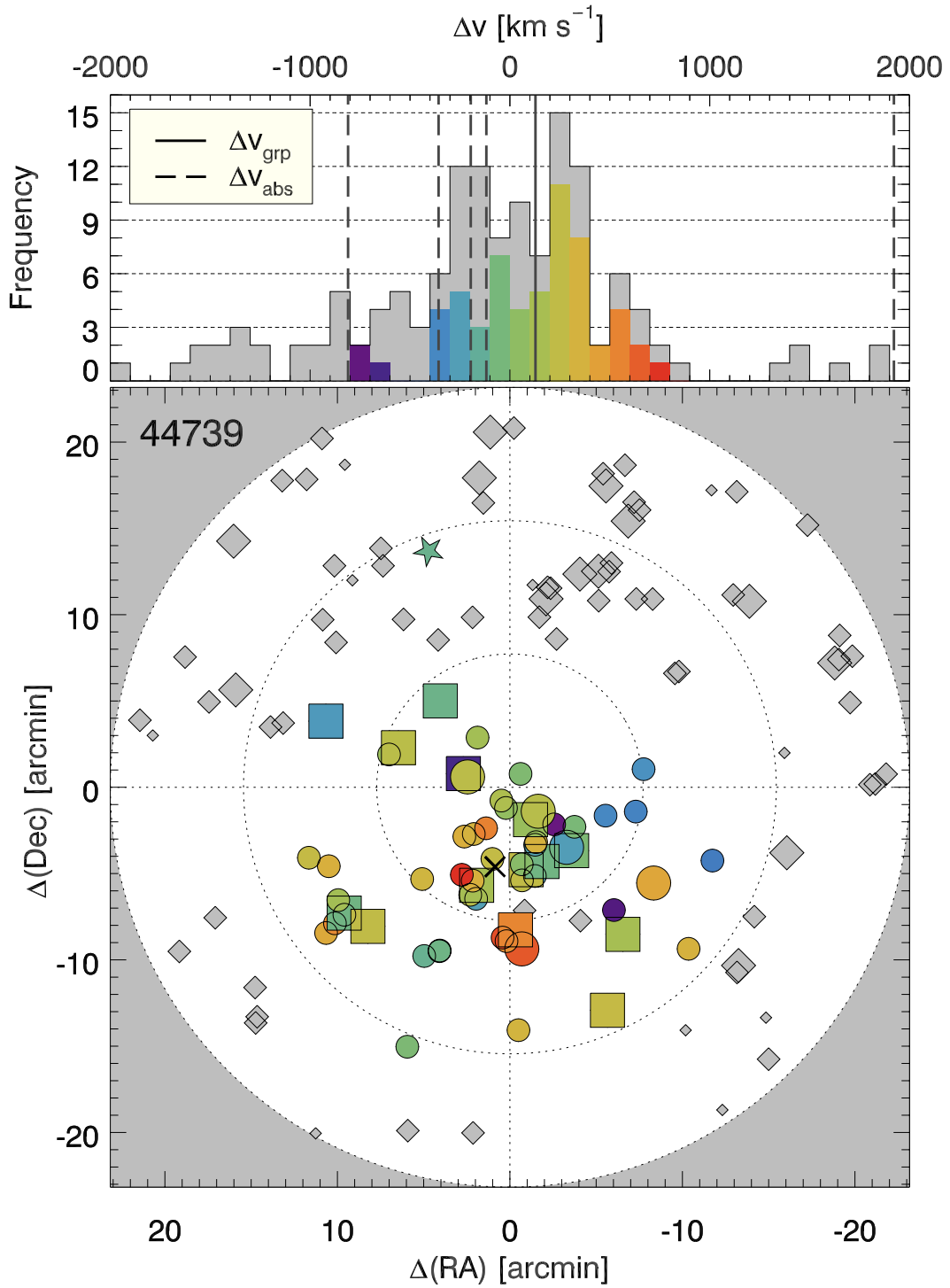


Figure 34. Same as Figure 4, but for the galaxy group 44739.

**Table 19.** Members of Group 44739

Name	RA	Dec	$z_{\text{gal}}$	$L_{\text{gal}}$ ( $L^*$ )	Type	$\Delta\rho$ (kpc)	$\Delta v$ ( $\text{km s}^{-1}$ )	$f_{\text{mem}}$ (%)
(1)	(2)	(3)	(4)	(5)	(6)	(7)	(8)	(9)
fbqs1519_206_837	229.799752	28.425806	0.11834	0.216	C	128	-13	99.5
fbqs1519_192_796	229.857945	28.422901	0.11924	1.25	A	326	228	99.5
fbqs1519_199_903	229.820809	28.400061	0.11904	0.228	C	118	174	99.5
fbqs1519_199_932	229.815774	28.392901	0.11864	0.829	C	158	67	99.5
fbqs1519_206_981	229.780355	28.389717	0.11918	2.00	C	278	212	99.4
1237664853113110825	229.788788	28.381629	0.11870	6.48	C	287	84	99.4
fbqs1519_189_1155	229.852309	28.322714	0.11976	0.435	A	752	367	99.4
1237664853113176111	229.847981	28.318204	0.11892	4.44	A	774	141	99.4
fbqs1519_188_1203	229.854999	28.309038	0.11915	0.829	C	857	204	99.4
fbqs1519_199_1135	229.798465	28.338533	0.11848	0.480	A	583	24	99.4
fbqs1519_191_996	229.851136	28.367766	0.11969	0.909	C	442	348	99.4
fbqs1519_203_1078	229.782686	28.359922	0.11971	0.578	A	455	354	99.4
fbqs1519_189_1000	229.861507	28.365299	0.11980	0.459	C	502	378	99.4
fbqs1519_194_1093	229.830694	28.343674	0.11936	0.220	C	552	260	99.4
fbqs1519_212_1084	229.740557	28.374685	0.11823	0.578	A	566	-43	99.4
1237662697033498829	229.776252	28.341178	0.11807	1.19	A	605	-85	99.4
1237662697033498854	229.793628	28.333293	0.11933	2.54	C	628	252	99.4
1237662697033433429	229.743619	28.351711	0.11827	2.01	C	662	-31	99.4
fbqs1519_198_1189	229.798179	28.322996	0.11928	0.230	A	702	239	99.4
fbqs1519_179_1140	229.907842	28.324282	0.11959	0.552	C	950	322	99.3
1237662697033498734	229.805329	28.275240	0.12040	1.09	C	1067	539	99.3
fbqs1519_194_984	229.837604	28.373312	0.12046	0.783	A	355	555	99.3
fbqs1519_193_1382	229.815173	28.264309	0.12032	0.252	C	1151	517	99.3
fbqs1519_201_1188	229.784031	28.327223	0.11747	0.166	A	689	-247	99.1
fbqs1519_208_1135	229.749198	28.354935	0.11742	4.00	C	617	-260	99.1
fbqs1519_203_1086	229.783702	28.357368	0.11755	0.375	C	470	-225	99.1
fbqs1519_189_1220	229.848547	28.305203	0.11747	0.480	A	871	-247	99.1
fbqs1519_197_670	229.847002	28.460884	0.11887	0.236	C	444	129	98.4
fbqs1519_182_1391	229.888887	28.254620	0.11791	0.220	C	1334	-129	97.8
fbqs1519_182_1389	229.888530	28.255241	0.11805	0.247	C	1329	-91	97.8
fbqs1519_218_1106	229.706368	28.385492	0.11707	0.284	E	746	-354	97.7
fbqs1519_180_1407	229.905567	28.249983	0.11790	0.304	C	1415	-131	96.1
fbqs1519_195_1420	229.798379	28.256838	0.12085	1.04	C	1212	659	96.0

*Table 19 continued*

**Table 19** (*continued*)

Name	RA	Dec	$z_{\text{gal}}$	$L_{\text{gal}}$ ( $L^*$ )	Type	$\Delta\rho$ (kpc)	$\Delta v$ ( $\text{km s}^{-1}$ )	$f_{\text{mem}}$ (%)
(1)	(2)	(3)	(4)	(5)	(6)	(7)	(8)	(9)
fbqs1519_193_1368	229.819522	28.267727	0.12094	0.459	C	1125	684	95.1
1237662697033433413	229.687321	28.270844	0.11891	1.21	A	1388	140	94.9
fbqs1519_223_1156	229.673166	28.389431	0.11700	0.374	E	959	-373	94.8
fbqs1519_218_1393	229.653568	28.320434	0.11997	1.49	E	1292	424	92.2
fbqs1519_187_1131	229.864254	28.328377	0.12119	0.230	A	747	751	91.8
1237664853113176496	229.967404	28.278578	0.11931	2.06	C	1487	247	91.3
1237664853113176370	229.933854	28.451119	0.11921	1.94	A	885	221	90.7
fbqs1519_168_720	229.944220	28.444590	0.11874	0.983	C	937	94	90.7
1237664853113241794	229.993429	28.291391	0.11808	6.34	A	1557	-83	88.1
fbqs1519_166_1297	229.993243	28.289816	0.11940	0.598	A	1563	271	88.1
fbqs1519_164_1253	229.999967	28.303963	0.11886	0.220	A	1537	126	88.0
fbqs1519_193_1694	229.802027	28.178356	0.11963	0.411	C	1817	332	88.0
1237664853113110919	229.887881	28.496281	0.11800	2.01	C	829	-104	87.5
fbqs1519_161_1149	230.010381	28.336676	0.11979	0.909	C	1478	375	87.5
fbqs1519_165_1334	230.003643	28.281529	0.12036	0.364	A	1659	528	87.3
fbqs1519_229_1064	229.664612	28.430366	0.11721	0.191	C	1009	-316	87.0
fbqs1519_164_1374	230.013327	28.272190	0.11990	0.399	A	1755	405	84.7
1237662697033498836	229.704289	28.197538	0.11942	2.35	C	1821	275	84.6
fbqs1519_157_1144	230.032239	28.344833	0.11937	0.362	C	1594	263	82.7
fbqs1519_178_1724	229.924164	28.162340	0.11828	0.527	C	2087	-29	76.9
1237664853113111100	229.862562	28.426096	0.11597	1.47	C	363	-649	74.9
fbqs1519_217_1651	229.615187	28.256910	0.11971	0.236	C	1802	354	67.3
fbqs1519_211_1404	229.697185	28.294325	0.11575	0.452	C	1204	-708	66.6
fbqs1519_227_1459	229.588995	28.342115	0.11690	0.542	C	1612	-399	65.4
1237662714216513886	230.013567	28.476778	0.11736	1.42	A	1463	-277	62.3
fbqs1519_208_1045	229.762816	28.377041	0.11554	0.220	C	432	-764	62.0

NOTE—Column 6 lists the galaxy’s spectral type: “E” for emission-line galaxies, “A” for absorption-line galaxies, and “C” for composite galaxies that show both emission and absorption.  $\Delta\rho$  and  $\Delta v$  are calculated with respect to the original SDSS group centers in Table 2;  $f_{\text{mem}}$  is the percentage of the Monte Carlo trials in which a galaxy was identified as a group member.

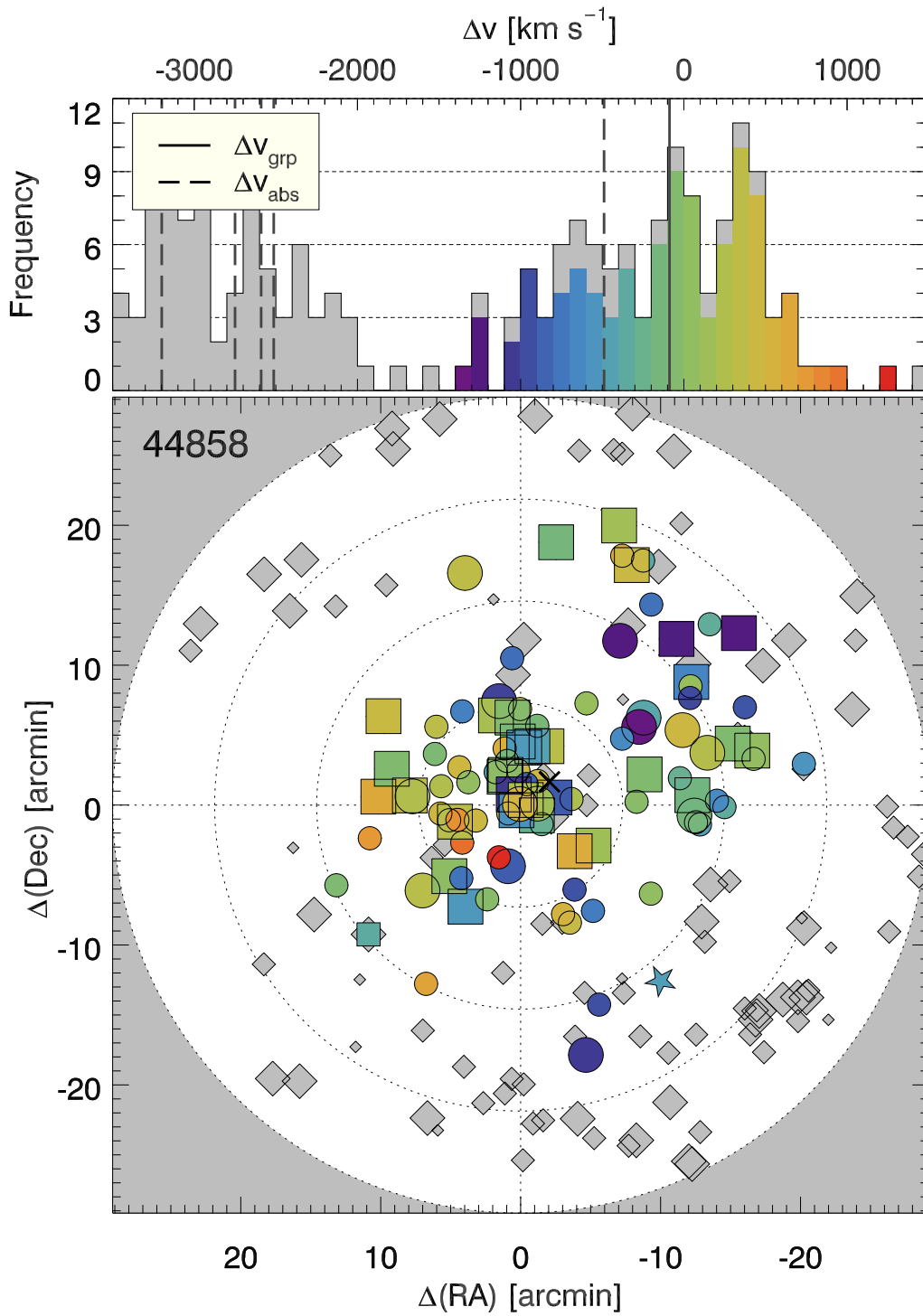


Figure 35. Same as Figure 4, but for the galaxy group 44858.

**Table 20.** Members of Group 44858

Name	RA	Dec	$z_{\text{gal}}$	$L_{\text{gal}}$ ( $L^*$ )	Type	$\Delta\rho$ (kpc)	$\Delta v$ ( $\text{km s}^{-1}$ )	$f_{\text{mem}}$ (%)
(1)	(2)	(3)	(4)	(5)	(6)	(7)	(8)	(9)
fbqs1519_36_1006	230.067973	28.879044	0.12915	0.487	A	289	465	100.0
fbqs1519_47_971	230.107970	28.840452	0.12854	0.588	A	147	303	100.0
1237664853649981733	230.084212	28.856470	0.12827	2.39	C	71	231	100.0
fbqs1519_43_969	230.092135	28.851719	0.12928	2.13	A	13	500	100.0
fbqs1519_38_1088	230.094152	28.891317	0.12903	0.813	A	338	433	100.0
fbqs1519_39_926	230.068302	28.852137	0.12794	2.34	C	165	144	100.0
A1518+2903	230.112920	28.884167	0.12748	9.00	...	320	22	100.0
1237664853649981766	230.111703	28.886344	0.12717	7.80	A	332	-61	100.0
fbqs1519_53_1049	230.151987	28.832008	0.12911	0.487	A	465	455	100.0
fbqs1519_30_868	230.021939	28.857599	0.12828	0.324	A	503	234	100.0
fbqs1519_48_1186	230.162244	28.877651	0.12764	0.713	C	561	64	100.0
1237662698107240590	230.095088	28.926195	0.12695	1.87	C	626	-119	100.0
1237664853649981617	230.055982	28.920543	0.12858	1.49	A	632	313	100.0
fbqs1519_48_1259	230.174489	28.895523	0.12916	0.324	A	708	468	100.0
fbqs1519_29_1215	230.068531	28.944855	0.12692	0.427	A	796	-128	100.0
1237662698107240568	230.102200	28.954633	0.12726	2.40	A	863	-38	100.0
1237662698107240601	230.124706	28.957202	0.12815	1.47	C	914	200	100.0
fbqs1519_31_1312	230.091905	28.964829	0.12863	0.449	E	944	327	100.0
fbqs1519_38_1200	230.112848	28.917833	0.12959	0.536	A	578	582	100.0
fbqs1519_39_1150	230.109487	28.902992	0.12685	0.468	A	454	-146	100.0
1237664853650047220	230.180477	28.830732	0.12859	1.32	A	666	317	99.9
fbqs1519_57_1187	230.200238	28.840372	0.12917	0.749	C	793	471	99.9
fbqs1519_57_1139	230.188336	28.832354	0.12863	0.586	C	718	327	99.9
fbqs1519_49_1373	230.207763	28.911295	0.12707	0.273	C	981	-88	99.9
fbqs1519_53_1258	230.199108	28.872921	0.12837	0.283	C	802	258	99.9
fbqs1519_46_1454	230.205717	28.943720	0.12864	0.586	C	1130	330	99.8
fbqs1519_57_1327	230.238204	28.860857	0.12839	1.82	C	1066	263	99.6
1237662698107306114	230.241759	28.861868	0.12884	2.24	A	1093	382	99.6
fbqs1519_41_844	230.062595	28.827728	0.12640	0.224	A	278	-266	99.5
1237664853649981719	230.069021	28.838277	0.12638	3.95	A	188	-270	99.5
1237664853649981663	230.017589	28.795516	0.12971	1.15	A	698	613	98.5
1237664853650047292	230.188101	28.765745	0.12746	2.83	C	990	16	98.3
1237662698107306135	230.266348	28.893687	0.12717	1.48	A	1315	-61	98.2

*Table 20 continued*

**Table 20** (*continued*)

Name	RA	Dec	$z_{\text{gal}}$	$L_{\text{gal}}$	Type	$\Delta\rho$	$\Delta v$	$f_{\text{mem}}$
(1)	(2)	(3)	(4)	( $L^*$ ) (5)	(6)	(kpc) (7)	( $\text{km s}^{-1}$ ) (8)	(%) (9)
fbqs1519_56_1112	230.177121	28.832739	0.13042	0.224	C	638	803	97.9
1237664853649981620	229.991978	28.802212	0.12790	2.88	A	819	133	97.5
fbqs1519_68_823	230.136652	28.738174	0.12730	0.468	A	983	-27	97.4
1237662698107175197	230.075083	28.920654	0.12577	1.28	C	591	-433	96.7
fbqs1519_17_1232	230.001597	28.971601	0.12769	0.991	C	1190	77	96.7
1237662698107306166	230.284677	28.860455	0.12980	3.32	C	1401	639	96.3
fbqs1519_72_1093	230.224528	28.748673	0.12860	1.02	A	1279	319	94.6
fbqs1519_43_1141	230.125036	28.889610	0.12557	0.295	A	406	-487	94.2
1237662698107240707	230.277593	28.956320	0.12903	1.36	C	1605	433	94.0
A1518+2905	230.086255	28.918888	0.12544	2.98	...	565	-522	93.0
1237664853650047289	230.166076	28.729427	0.12540	1.62	A	1136	-532	93.0
fbqs1519_67_1390	230.296240	28.810938	0.13025	0.586	C	1518	758	92.8
fbqs1519_9_775	229.933491	28.854357	0.12734	0.606	C	1139	-16	90.8
fbqs1519_60_507	230.033469	28.720512	0.12937	0.218	E	1150	524	90.8
1237664853650047101	230.096791	28.844224	0.12522	4.27	C	66	-580	90.6
1237664853649916286	229.922568	28.886993	0.12713	1.37	A	1254	-71	89.5
fbqs1519_59_1038	230.170512	28.805691	0.13105	0.263	E	682	971	89.4
fbqs1519_61_463	230.024157	28.710384	0.12890	0.259	C	1253	399	87.9
fbqs1519_11_1051	229.953217	28.929481	0.12506	0.324	A	1191	-622	86.8
fbqs1519_5_1131	229.923964	28.954531	0.12591	1.18	A	1482	-396	83.2
fbqs1519_41_1435	230.170512	28.962065	0.12481	0.206	E	1085	-689	81.2
fbqs1519_48_418	229.992757	28.724390	0.12469	0.355	A	1260	-721	79.0
fbqs1519_66_963	230.171800	28.763405	0.12455	0.177	A	925	-758	75.3
fbqs1519_28_1523	230.102663	29.025417	0.12440	0.194	C	1446	-798	72.5
fbqs1519_354_873	229.874582	28.882448	0.12642	0.324	A	1586	-261	70.6
fbqs1519_8_376	229.914050	28.744917	0.12759	0.216	C	1548	51	69.7
fbqs1519_38_1021	230.083094	28.875464	0.12418	0.468	C	215	-856	69.3
fbqs1519_57_819	230.108314	28.777596	0.12410	1.18	C	613	-878	68.8
1237664853649981650	230.045102	28.859411	0.12405	1.60	A	341	-890	68.8
1237664853649916215	229.857600	28.862229	0.12676	1.30	A	1690	-171	67.9
fbqs1519_355_1079	229.871092	28.939735	0.12915	1.07	C	1752	465	67.9
fbqs1519_347_723	229.854827	28.837967	0.12685	1.12	A	1710	-146	67.8
fbqs1519_48_538	230.017848	28.749735	0.12391	0.468	A	985	-928	67.8
fbqs1519_346_697	229.852681	28.830008	0.12491	0.753	C	1731	-662	67.8
fbqs1519_345_691	229.847288	28.827349	0.12569	0.205	A	1772	-455	66.9

*Table 20 continued*

Table 20 (continued)

Name	RA	Dec	$z_{\text{gal}}$	$L_{\text{gal}}$ ( $L^*$ )	Type	$\Delta\rho$ (kpc)	$\Delta v$ ( $\text{km s}^{-1}$ )	$f_{\text{mem}}$ (%)
(1)	(2)	(3)	(4)	(5)	(6)	(7)	(8)	(9)
fbqs1519_34_1385	230.120502	28.974247	0.12364	1.15	C	1043	-1000	62.3
fbqs1519_347_998	229.837246	28.912718	0.12845	1.07	C	1904	279	62.1
fbqs1519_354_1219	229.860749	28.977970	0.12374	0.369	A	1968	-973	61.7
fbqs1519_341_809	229.824228	28.855625	0.12507	0.205	A	1929	-620	61.3
1237664853649981755	230.100548	28.863074	0.12343	1.11	A	125	-1056	60.3
fbqs1519_354_1269	229.860120	28.991983	0.12771	0.371	A	2036	82	60.2
1237664853649916125	229.859077	28.997116	0.12490	6.98	A	2067	-664	59.5
fbqs1519_338_793	229.814000	28.847992	0.12614	0.474	C	2002	-335	59.5
fbqs1519_76_1451	230.341659	28.754915	0.12712	0.241	C	1975	-74	53.8
A1519+2852A	230.297914	28.696388	0.12610	0.267	...	1962	-346	53.5
1237664853649916119	229.802722	28.923720	0.12715	1.53	A	2169	-68	51.7
fbqs1519_91_1008	230.219722	28.637480	0.12994	0.393	E	1988	675	51.5
1237662698107109633	229.879193	29.048287	0.12283	1.34	A	2237	-1214	45.3
fbqs1519_2_1614	229.913535	29.089283	0.12449	0.742	C	2351	-774	44.9
1237664853649916076	229.776261	28.915262	0.12762	2.91	C	2336	57	44.9
fbqs1519_335_1032	229.774404	28.905470	0.12763	0.536	A	2332	61	44.9
fbqs1519_8_1468	229.955964	29.046102	0.12272	1.19	C	1886	-1245	44.9
fbqs1519_341_1227	229.786234	28.966974	0.12392	0.265	E	2402	-925	44.9
fbqs1519_29_1940	230.166879	29.126911	0.12870	1.35	C	2346	346	44.8
fbqs1519_109_283	229.984460	28.612741	0.12385	0.236	C	2107	-944	44.8
fbqs1519_352_1543	229.834013	29.065804	0.12620	0.593	C	2569	-319	39.1
fbqs1519_6_1092	229.930029	28.943438	0.12241	1.07	C	1394	-1327	39.1
1237662698107109663	229.939969	29.136340	0.12906	1.29	A	2599	441	39.1
1237664854186787103	230.042862	29.163441	0.12683	1.45	C	2606	-153	37.7
fbqs1519_6_1830	229.952989	29.147474	0.12980	0.593	C	2645	638	37.7
fbqs1519_3_1804	229.924593	29.141710	0.12597	0.395	E	2687	-380	36.8
1237662698107109562	229.794297	29.055259	0.12273	2.15	A	2729	-1243	36.0
fbqs1519_57_874	230.120787	28.788191	0.13208	0.327	C	556	1245	33.4
fbqs1519_324_1115	229.706025	28.899624	0.12532	0.618	A	2811	-553	28.3
1237662698107109639	229.957209	29.183463	0.12799	1.45	C	2912	158	25.6
fbqs1519_131_452	230.002427	28.552778	0.12346	1.02	A	2538	-1048	21.2

NOTE—Column 6 lists the galaxy’s spectral type: “E” for emission-line galaxies, “A” for absorption-line galaxies, and “C” for composite galaxies that show both emission and absorption.  $\Delta\rho$  and  $\Delta v$  are calculated with respect to the original SDSS group centers in Table 2;  $f_{\text{mem}}$  is the percentage of the Monte Carlo trials in which a galaxy was identified as a group member.

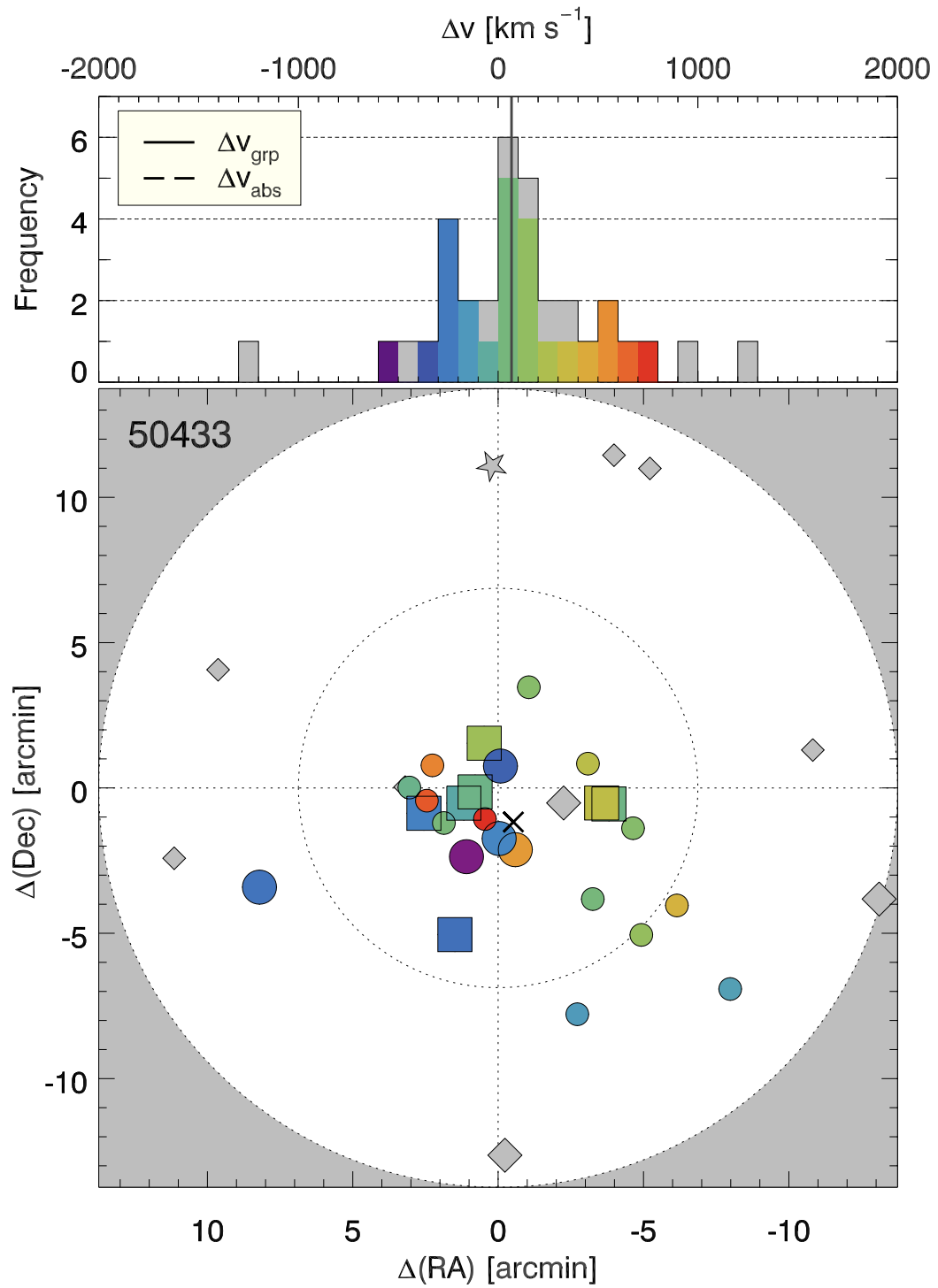


**Figure 36.** Same as Figure 4, but for the galaxy group 50433.

**Table 21.** Members of Group 50433

Name	RA	Dec	$z_{\text{gal}}$	$L_{\text{gal}}$ ( $L^*$ )	Type	$\Delta\rho$ (kpc)	$\Delta v$ ( $\text{km s}^{-1}$ )	$f_{\text{mem}}$ (%)
(1)	(2)	(3)	(4)	(5)	(6)	(7)	(8)	(9)
1237665015235870817	157.765069	30.855472	0.13571	2.36	A	188	-74	99.9
1237665015235870836	157.751425	30.889867	0.13673	3.51	A	234	195	99.9
fbqs1030_182_769	157.741456	30.835203	0.13518	1.03	A	253	-214	99.9
fbqs1030_172_743	157.778378	30.844095	0.13621	0.207	A	323	58	99.9
1237665015235870848	157.791725	30.849692	0.13512	3.26	A	392	-229	99.9
1237665015235870816	157.757518	30.861972	0.13605	11.4	A	117	16	99.9
fbqs1030_164_685	157.801409	30.864449	0.13600	0.542	A	444	3	99.9
1237665015235805294	157.668127	30.855027	0.13606	3.82	A	560	19	99.9
fbqs1030_191_462	157.721658	30.921972	0.13642	0.495	C	527	113	99.9
1237665015235805295	157.672999	30.855598	0.13717	1.74	C	523	313	99.9
fbqs1030_201_645	157.682147	30.878136	0.13711	0.823	A	465	296	99.9
fbqs1030_196_917	157.678928	30.800493	0.13620	0.674	C	730	55	99.9
fbqs1030_205_802	157.652035	30.841126	0.13639	0.259	A	704	106	99.9
fbqs1030_182_619	157.740569	30.876751	0.13478	1.19	A	110	-319	99.9
1237665126923173993	157.771036	30.780119	0.13493	1.59	A	765	-279	99.8
fbqs1030_185_793	157.730684	30.828814	0.13793	1.36	A	320	512	98.7
fbqs1030_201_1015	157.646513	30.779943	0.13660	0.652	C	1026	161	98.5
fbqs1030_207_984	157.622752	30.796824	0.13751	0.301	C	1070	401	98.2
fbqs1030_167_630	157.786017	30.877161	0.13818	0.294	C	347	578	97.6
fbqs1030_191_1145	157.689257	30.734449	0.13547	0.269	C	1199	-137	93.8
fbqs1030_168_703	157.789722	30.856916	0.13856	0.823	A	362	678	90.3
fbqs1030_176_808	157.763286	30.824806	0.13372	1.00	C	378	-599	79.6
fbqs1030_179_728	157.750955	30.846392	0.13887	0.312	A	169	760	79.0
fbqs1030_148_992	157.901502	30.807314	0.13497	1.30	C	1293	-269	75.5
fbqs1030_208_1186	157.587161	30.748926	0.13555	0.339	C	1536	-116	66.9

NOTE—Column 6 lists the galaxy’s spectral type: “E” for emission-line galaxies, “A” for absorption-line galaxies, and “C” for composite galaxies that show both emission and absorption.  $\Delta\rho$  and  $\Delta v$  are calculated with respect to the original SDSS group centers in Table 2;  $f_{\text{mem}}$  is the percentage of the Monte Carlo trials in which a galaxy was identified as a group member.

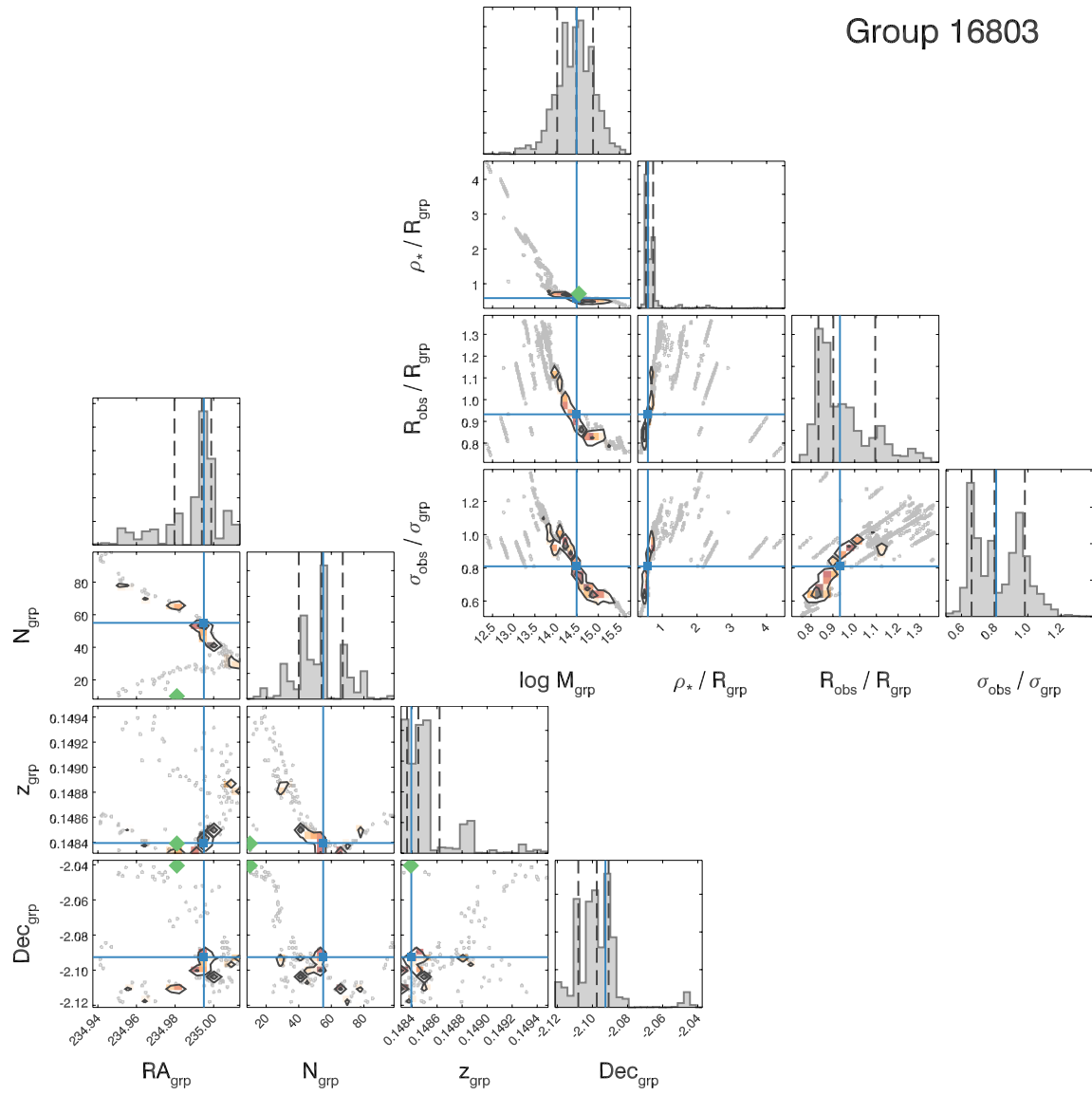


Figure 37. Same as Figure 15, but for the galaxy group 16803.

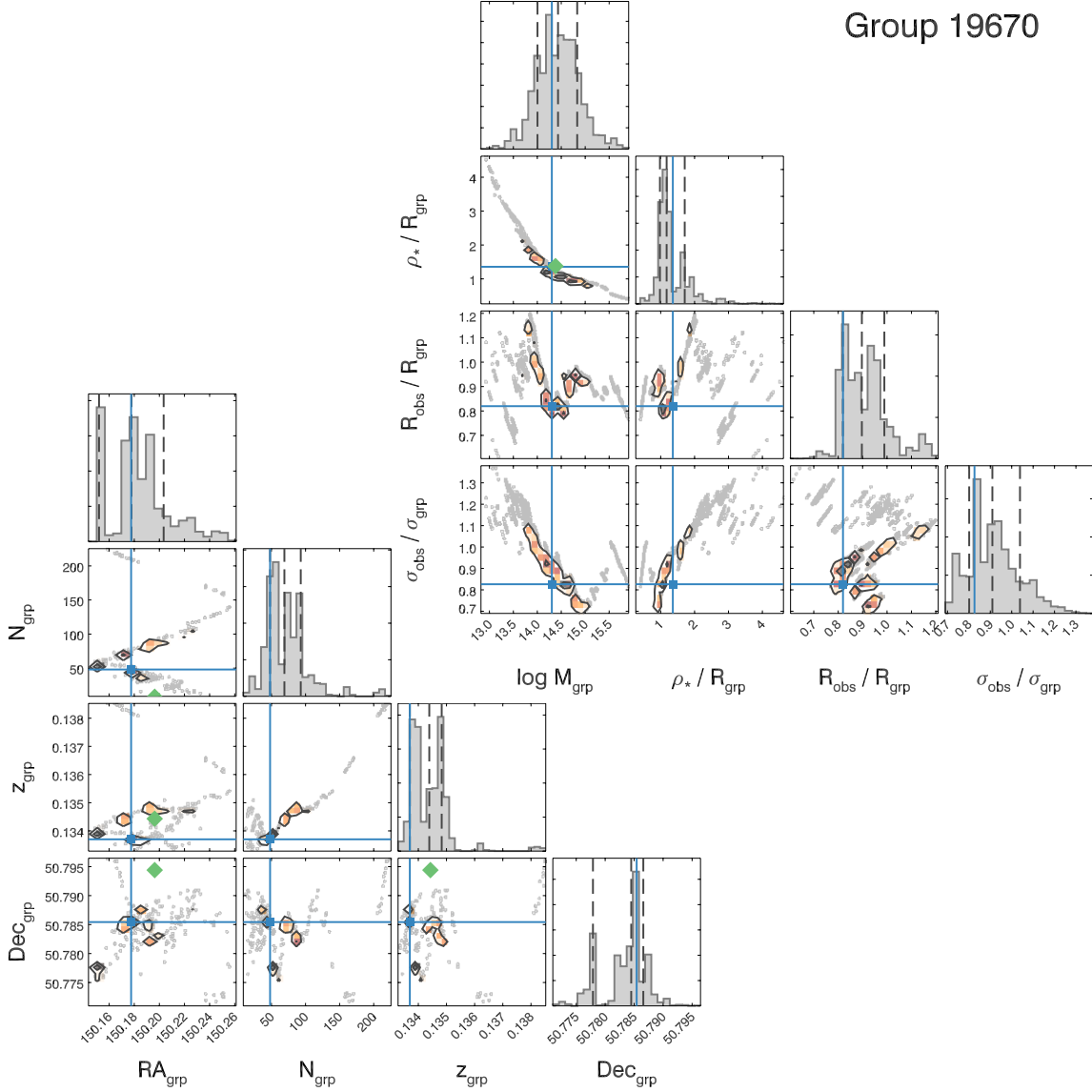
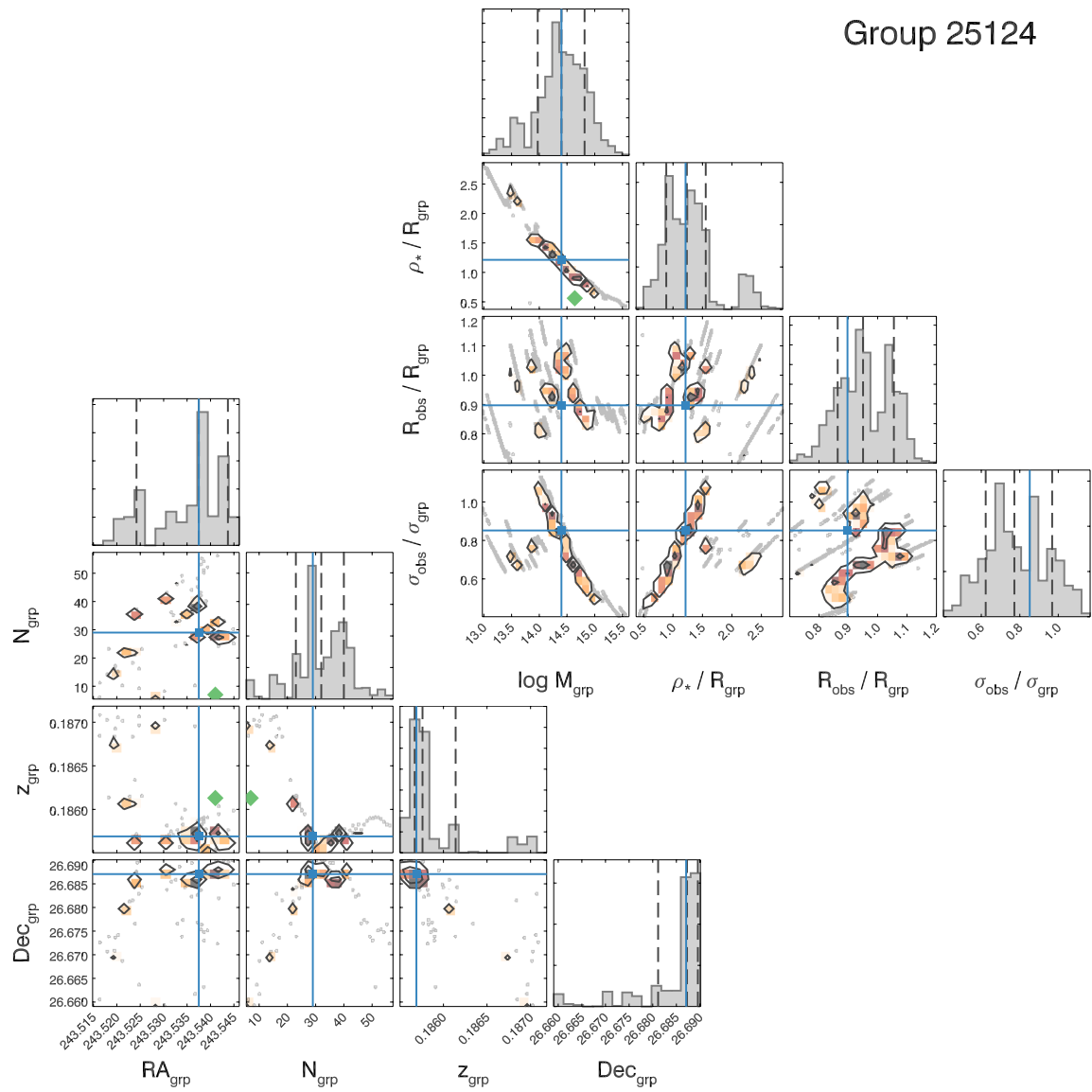


Figure 38. Same as Figure 15, but for the galaxy group 19670.



**Figure 39.** Same as Figure 15, but for the galaxy group 25124.

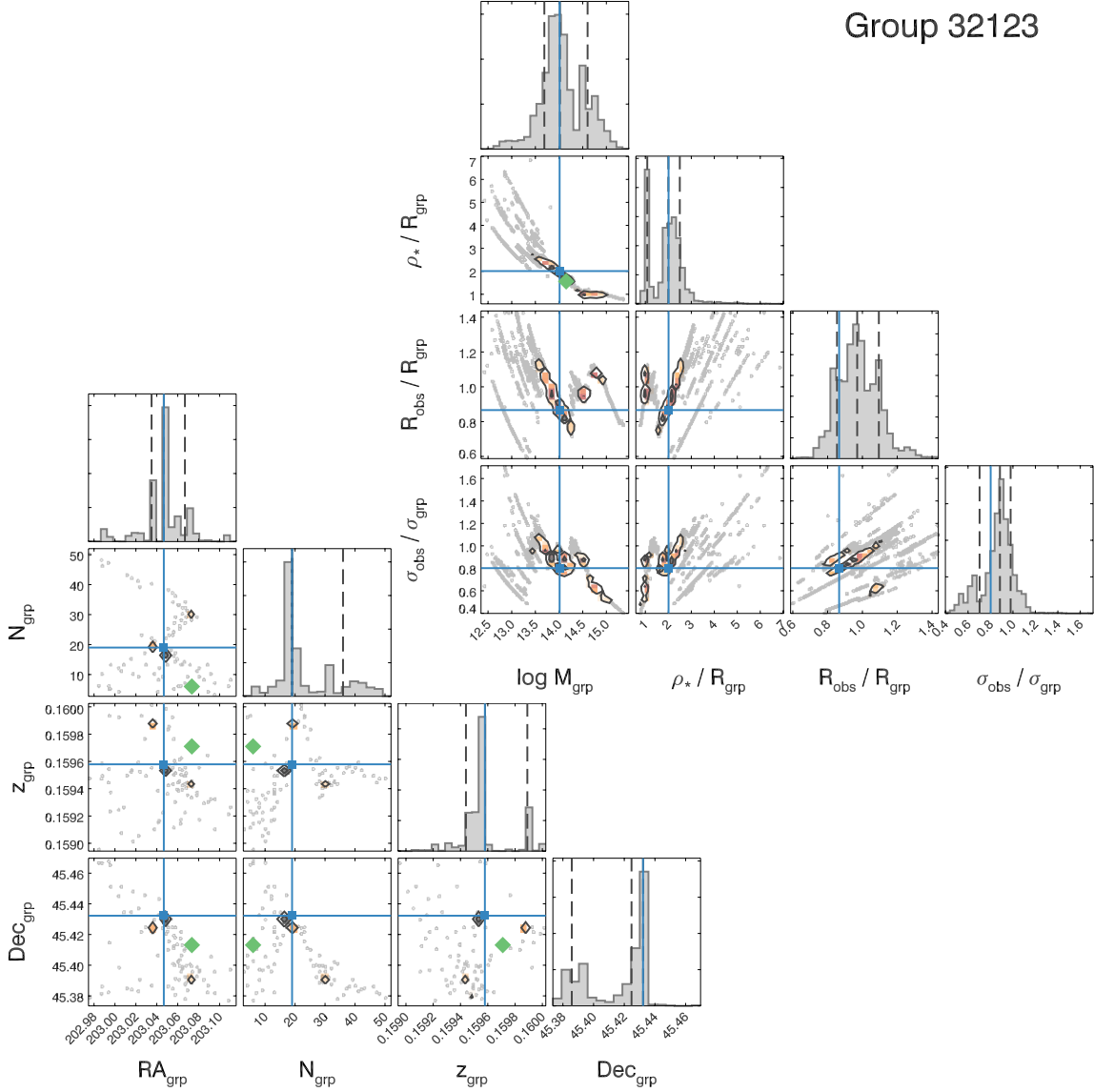


Figure 40. Same as Figure 15, but for the galaxy group 32123.

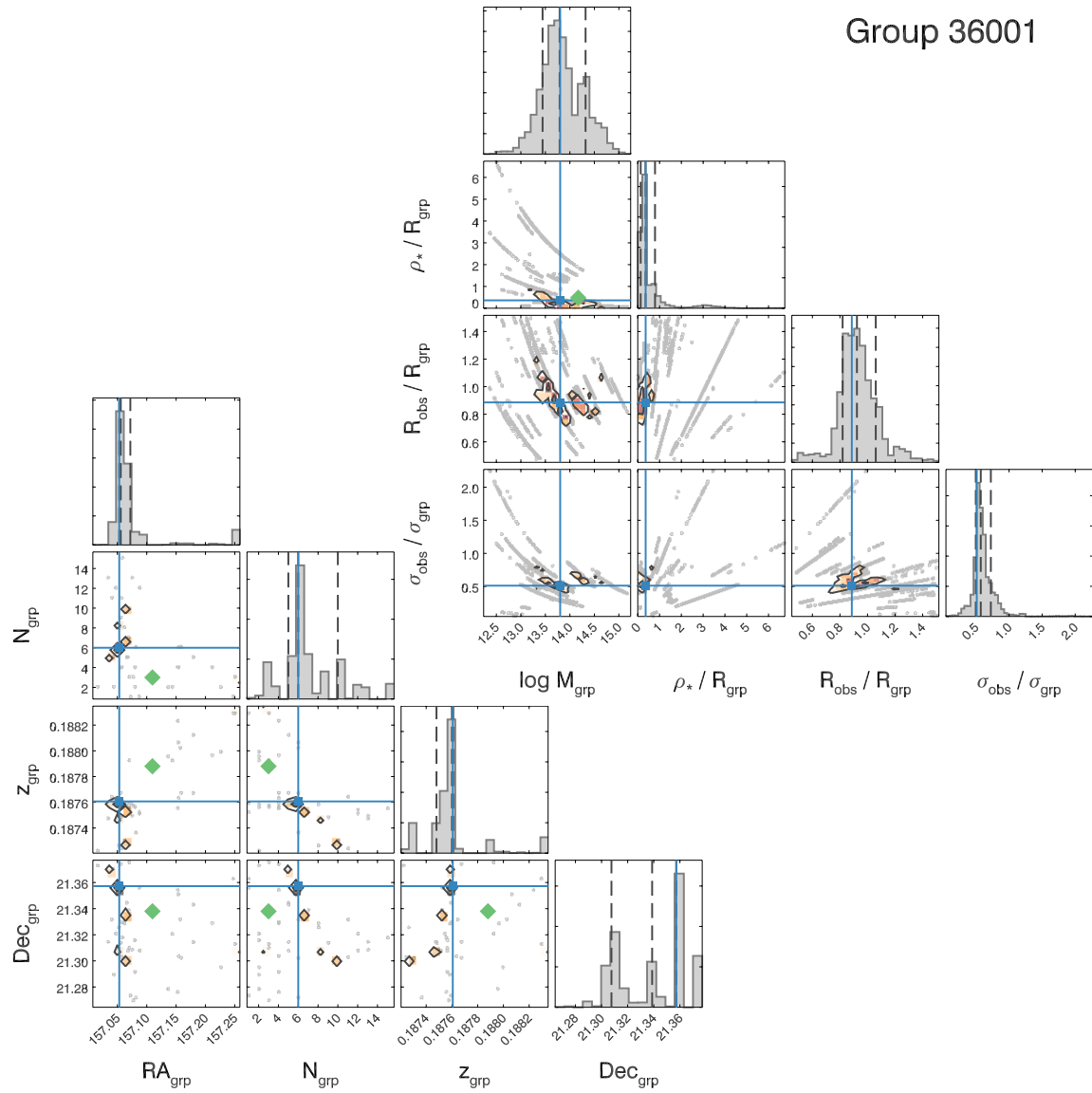


Figure 41. Same as Figure 15, but for the galaxy group 36001.

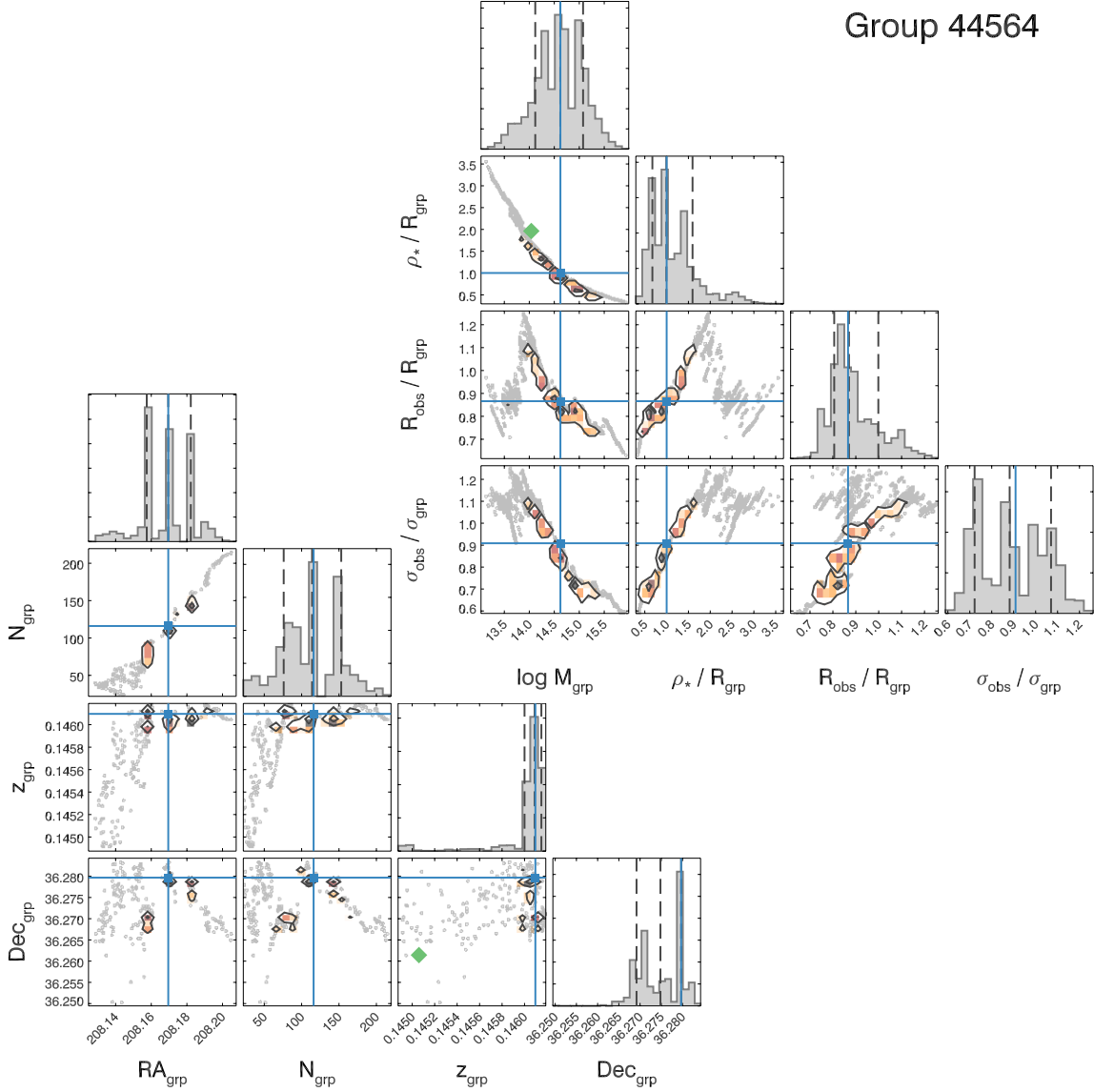
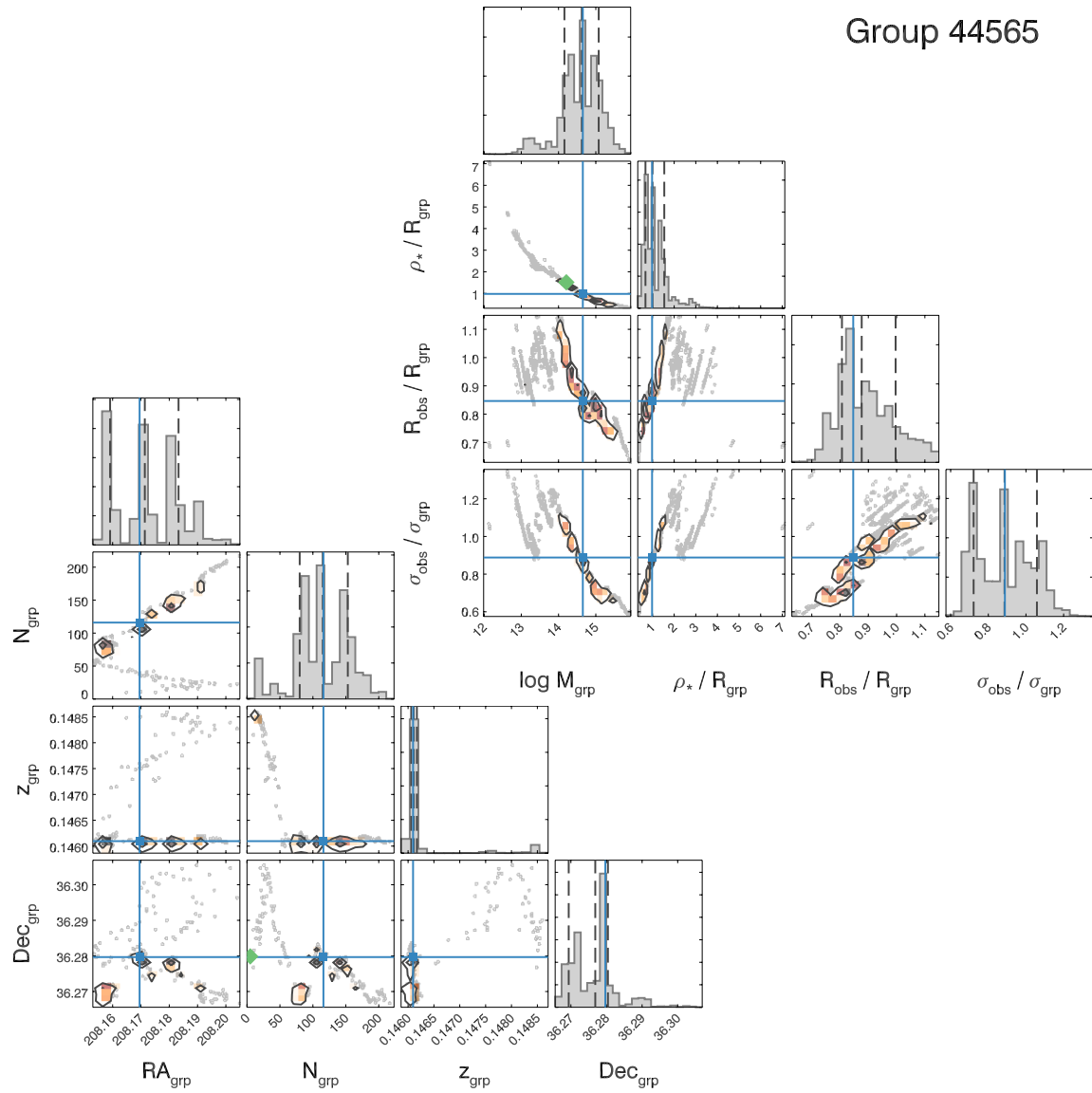


Figure 42. Same as Figure 15, but for the galaxy group 44564.



**Figure 43.** Same as Figure 15, but for the galaxy group 44565.

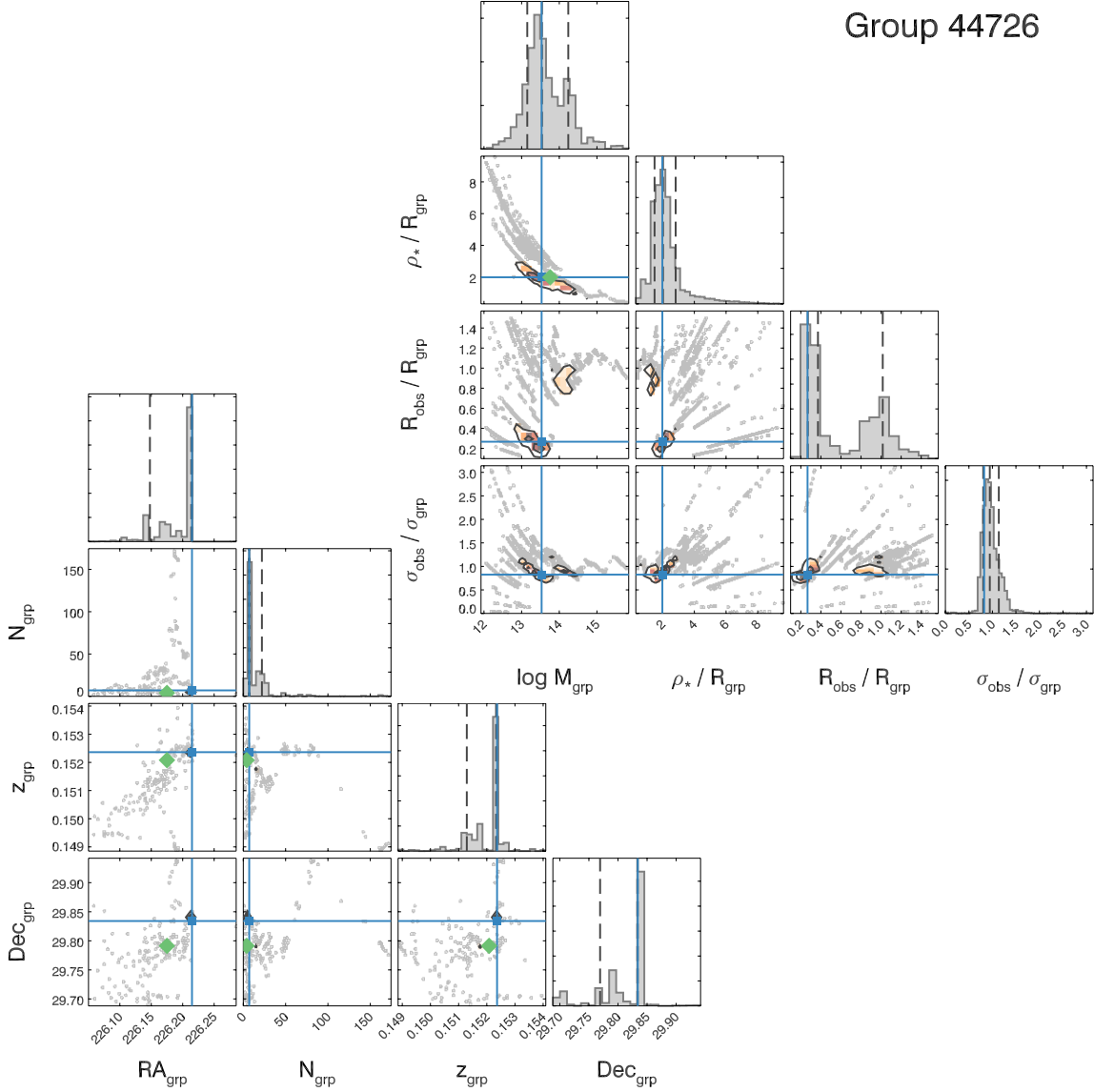
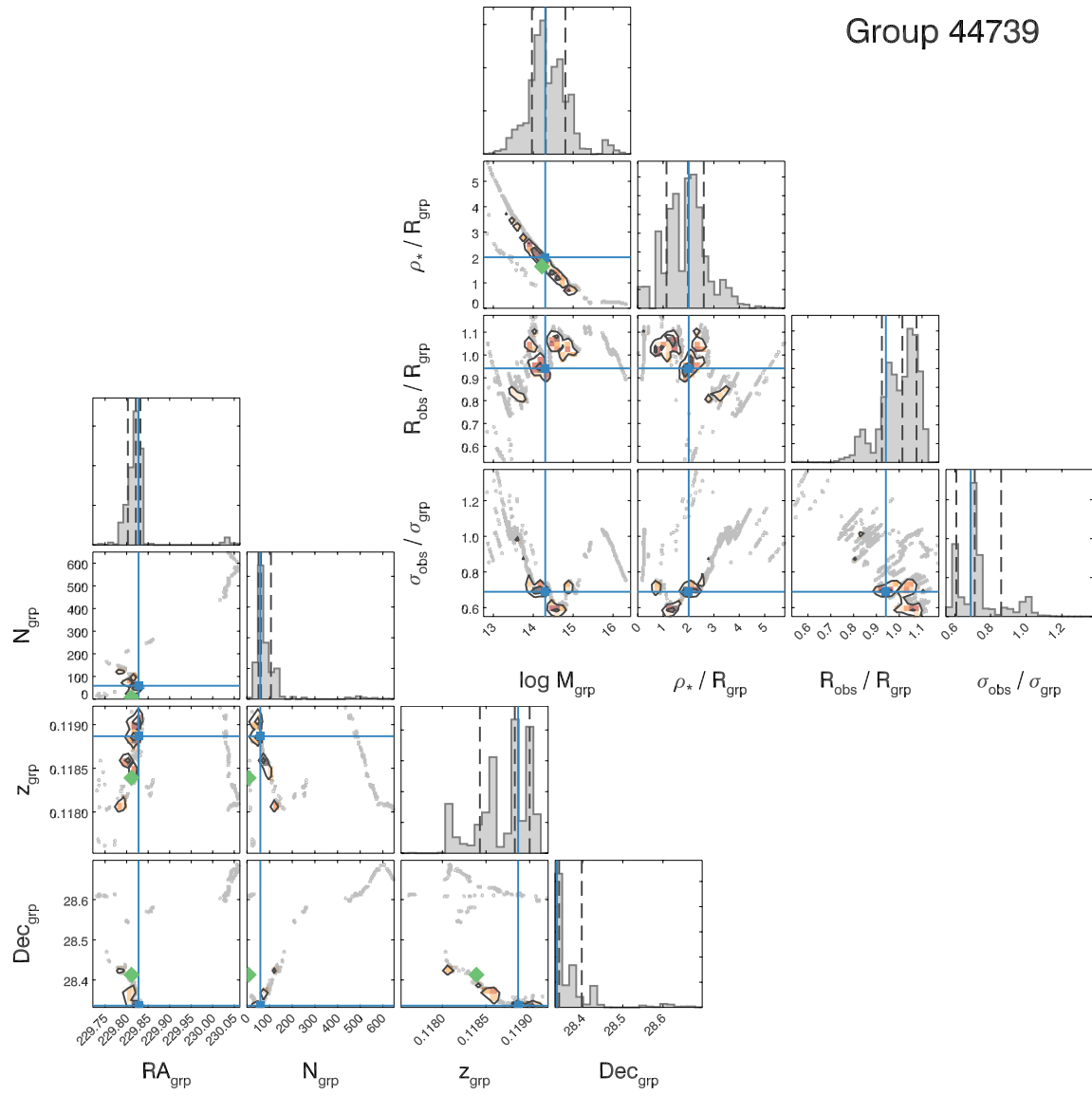


Figure 44. Same as Figure 15, but for the galaxy group 44726.



**Figure 45.** Same as [Figure 15](#), but for the galaxy group 44739.

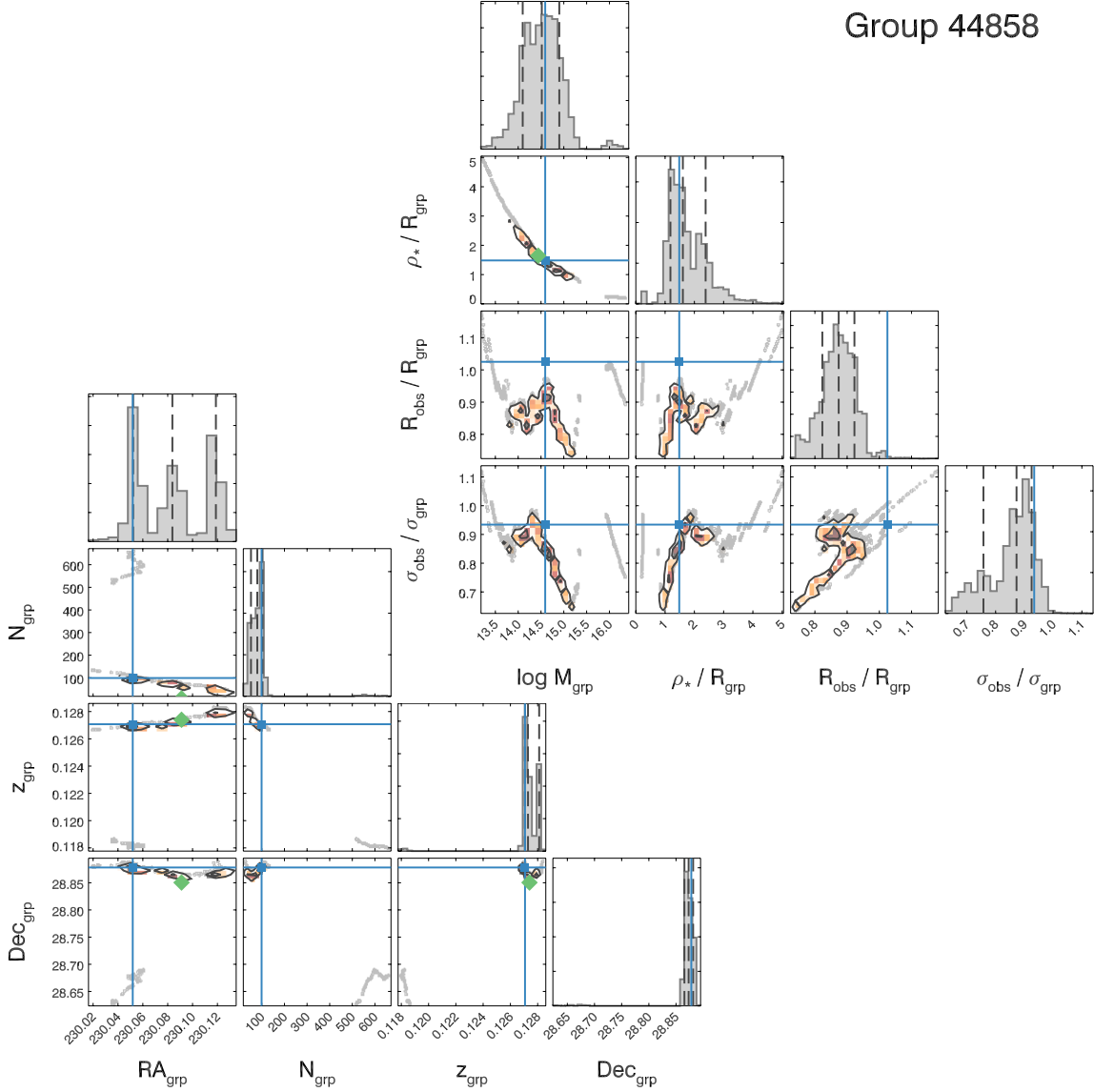


Figure 46. Same as Figure 15, but for the galaxy group 44858.

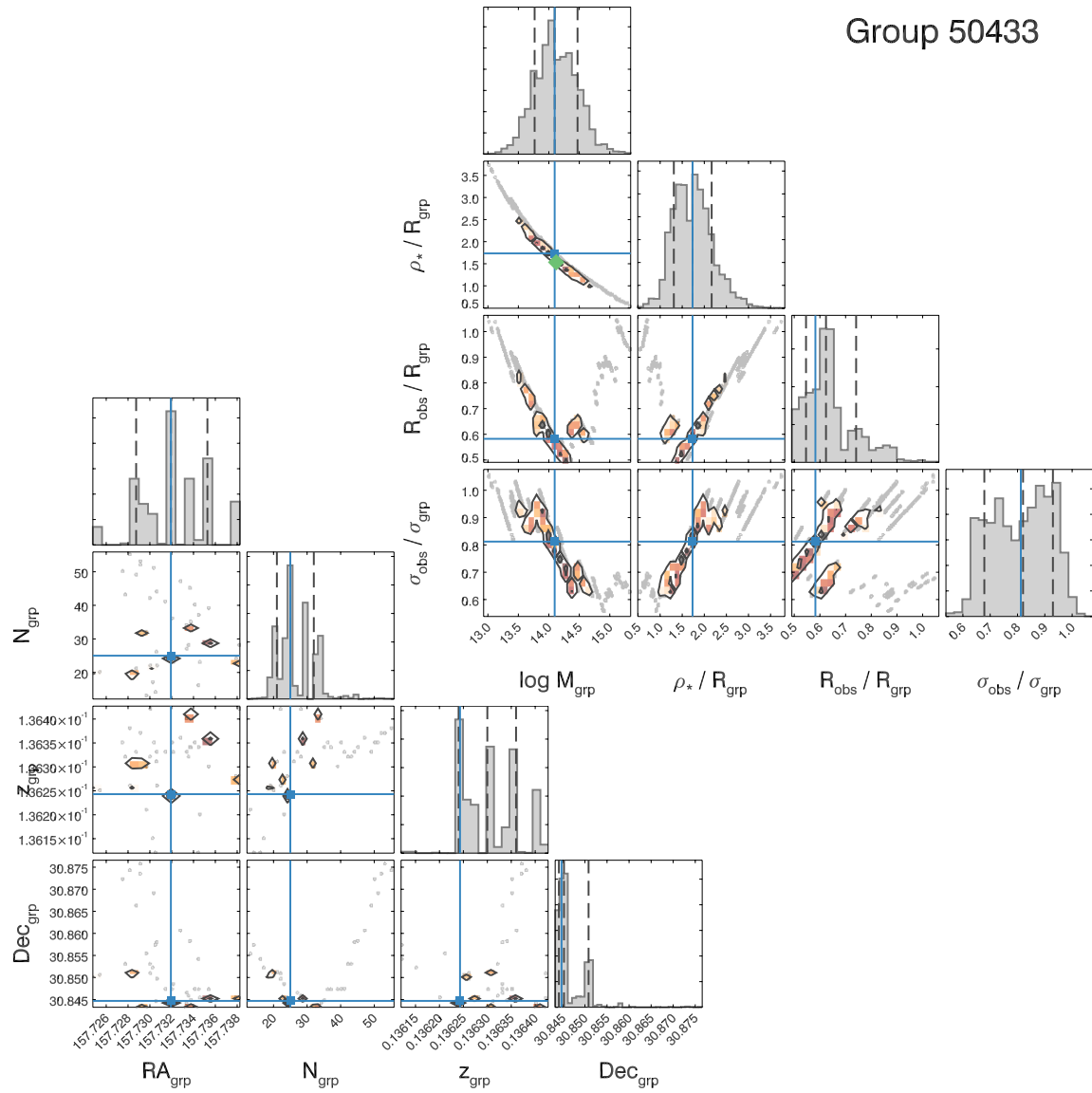


Figure 47. Same as Figure 15, but for the galaxy group 50433.